UNIVERSITY OF HELSINKI REPORT SERIES IN PHYSICS

No. D279 (2022)

Energetic electron dynamics in the outer Van Allen radiation belt during sheath regions driven by interplanetary coronal mass ejections

Milla Kalliokoski

Academic dissertation

Department of Physics
Faculty of Science
University of Helsinki
Helsinki, Finland

To be presented, with the permission of the Faculty of Science of the University of Helsinki, for public criticism in Banquet Room 303 (Unioninkatu 33) on September 20th, 2022, at 13 o'clock.

Helsinki 2022

Supervising professor
Professor Emilia Kilpua, University of Helsinki, Finland

Thesis supervisors
Professor Emilia Kilpua, University of Helsinki, Finland
Assistant Professor Adnane Osmane, University of Helsinki, Finland

Pre-examiners
Assistant Professor Lauren Blum, University of Colorado at Boulder, USA
Dr. Lauri Holappa, University of Oulu, Finland

Opponent
Professor Xinlin Li, University of Colorado at Boulder, USA

ISSN 0356-0961
ISBN 978-951-51-8513-6 (print)
ISBN 978-951-51-8514-3 (pdf)
Helsinki University Print (Unigrafia)
http://ethesis.helsinki.fi/
Helsinki 2022

Milla Maria Helena Kalliokoski
University of Helsinki, 2022

Abstract

Phenomena originating in the Sun are the main drivers of activity in the near-Earth space environment. Plasma and magnetic fields constantly flow out of the solar atmosphere, including eruptions of large magnetized plasma clouds. These clouds propagate away from the Sun to large distances, and when detected directly, they are called interplanetary coronal mass ejections (ICMEs). When ICMEs impact the Earth, they compress the magnetosphere and fill it with different plasma waves, which further affect the charged particles trapped in the geomagnetic field. These energetic particles in the Earth's radiation belts are important to understand because they pose a significant threat for satellites. However, which physical processes – such as acceleration, scattering loss or radial diffusion – dominate the radiation belt response to a given solar wind driver structure cannot yet be predicted accurately. The dynamics remain elusive especially on short timescales of less than an hour due to the demanding level of the required data density.

This thesis performs the first comprehensive and detailed statistical study on how turbulent sheath regions ahead of ICMEs affect plasma waves in the inner magnetosphere and outer radiation belt electrons. With high quality multi-point satellite measurements, the outer belt response to sheaths as a function of electron energy and radial location has been revealed. The studied sheath events were also divided based on their capability to drive geomagnetic activity, and computational tools were employed to separate adiabatic and nonadiabatic effects.

Statistical analysis presented in this thesis shows that wave activity is elevated during sheaths which provides favorable conditions for wave-particle interactions. The high dynamic pressure of the sheaths also pushes the magnetopause inward facilitating significant electron losses. Flux measurements from both the Van Allen Probes and the Global Positioning System (GPS) satellite missions evidence that sheaths tend to enhance the fluxes of low energy (10s to 100s keV) electrons but deplete the high energy (> MeV) electrons. The larger number of satellites in the GPS constellation was crucial in confirming that the obtained results were due to the sheath and not influenced significantly by the following ejecta. Additionally, computation of phase space density showed that all sheaths can cause permanent loss, either by loss at the magnetopause or scattering to the atmosphere, but

energization of electrons requires a sheath than can also drive storm conditions in the magnetosphere.

This thesis shows that by utilizing multi-point and multi-satellite observations, assessing the overall geospace conditions from waves, geomagnetic activity and radiation belt electron variability, the impact of sheath regions could be determined. This thesis also demonstrates that sheaths which do not generate geomagnetic storms are able to drive significant changes in the outer belt electron populations, which should be noted in the event selection that often focuses on storm periods. Furthermore, the work presented in this thesis highlights the high data density of GPS satellites, which enables studying electron dynamics on timescales of a few tens of minutes, and its good synergy with Van Allen Probes measurements.

Keywords: *Space Physics, Space Weather, Coronal Mass Ejections, Sheath Regions, Radiation Belts, Phase Space Density*

Tiivistelmä

Maapallon magneettikenttä vangitsee sähköisesti varattuja hiukkasia muodostaen planeetan ympärille niin kutsutut säteilyvyöt. Ulompi säteilyvyö koostuu pääosin elektroneista, joiden määrä ja energiat vaihtelevat niin minuuttien kuin päivien aikaskaaloilla johtuen vuorovaikutuksista esimerkiksi sähkömagneettisten aaltojen kanssa. Tutkimuksia elektronivuon muutoksista tarvitaan, jotta voidaan selvittää säteilyvyön olosuhteita kulloinkin hallitsevat mekanismit. Tämä tieto on tärkeää, sillä useat navigaatio- ja telekommunikaatiosatelliitit kiertävät Maata ulommassa säteilyvyössä, jossa ne ovat alttiita korkeaenergisten elektronien aiheuttamille häiriöille ja vahingoille.

Säteilyvöiden olosuhteita muovaa aurinkotuuli, joka koostuu Auringosta alati virtaavista varatuista hiukkasista ja kuljettaa mukanaan Auringon magneettikenttää. Lisäksi tähtemme koronassa tapahtuu ajoittain voimakkaita purkauksia, joissa planeettainväliseen avaruuteen sinkoutuu valtavia kaasupilviä. Nämä koronan massapurkaukset saavat aikaan erityisen voimakkaita muutoksia säteilyvöissä niihin törmätessään. Purkaukset ovat yleensä niin nopeita, että niiden eteen muodostuu shokkiaalto. Shokin ja itse purkauksen välissä aurinkotuuli pakkautuu purkauksen eteen, ja tätä pyörteistä aluetta, jossa magneettikentän suunnassa ja voimakkuudessa on suurta heilahtelua, kutsutaan välivyöhykkeeksi.

Tässä väitöskirjassa tutkitaan nimenomaan välivyöhykkeiden aikaansaamia muutoksia ulomman säteilyvyön olosuhteissa. Tutkimuksessa tarkasteltiin huomattavasti lyhyempiä aikaskaaloja kuin aiemmin, jotta välivyöhykkeen aiheuttamat muutokset voitiin erottaa heti sen jälkeen Maan lähiavaruuteen iskeytyvän massapurkauksen aiheuttamista muutoksista. Käyttämällä ulommassa säteilyvyössä sijaitsevien satelliittien tieteellisiä mittauksia, työssä määritettiin erityyppisten sähkömagneettisten aaltojen aktiivisuus Maan magnetosfäärissä sekä elektronivuon muutos verraten vuon arvoja välittömästi ennen ja jälkeen välivyöhykkeen vaikutusta. Aaltoaktiivisuus on korkea välivyöhykkeiden aikana, minkä ansiosta monet vuorovaikutukset ovat mahdollisia, joko antaen elektroneille energiaa tai poistamalla niitä säteilyvöistä. Elektronivuon muutokset riippuvat energiasta ja etäisyydestä Maasta. Elektronivuon arvoista ja Maan magneettikentän mallinnuksesta johdettua suuretta, faasiavaruustiheyttä, tarkastelemalla selvitettiin, että useimpien välivyöhykkeiden vaikutuksesta elektroneita poistuu systeemistä, joko planeettainväliseen avaruuteen tai Maan ilmakehään. Sen sijaan vain sellaiset välivyöhykkeet, jotka aikaansaavat magneettisen myrskyn, voivat energisoida elektroneita pysyvästi.

Contents

Preface

First and foremost, I want to thank my supervisors Prof. Emilia Kilpua and Asst. Prof. Adnane Osmane. They have provided me with guidance and encouragement throughout my doctoral studies, and it has been my pleasure to work with Emilia from my Bachelor's thesis to this doctoral thesis. I am also grateful to Prof. Emer. Hannu Koskinen who steered me in the direction of space physics – a field of science that I have since found extremely fascinating!

I wish to thank my pre-examiners Asst. Prof. Lauren Blum and Dr. Lauri Holappa for their time in reading and evaluating this thesis. I would also like to thank in advance Prof. Xinlin Li who has accepted to act as my opponent during the defence. I appreciate his expertise on the topic of this thesis.

My warm thanks also go to all my co-authors on the publications which are the basis of this thesis: Assoc. Prof. Allison Jaynes, Dr. Drew Turner, Dr. Michael Henderson, Dr. Steven Morley, Ms. Harriet George, Dr. Lucile Turc, Dr. Sanni Hoilijoki, Mr. Leonid Olifer, and Prof. Minna Palmroth. Their feedback has been invaluable for the success of the research presented here. Additionally, I am grateful for Assoc. Prof. Jaynes for hosting me at the University of Iowa, and Dr. Turner for hosting me at the Johns Hopkins University Applied Physics Laboratory. These research visits have been great experiences that have taught me a lot and expanded my research skills. I am also grateful for Dr. Henderson and Dr. Morley for being my mentors during the Los Alamos Space Weather Summer School, granting me an opportunity to learn using a new data set directly from its experts.

I thank my colleagues in the space physics corridor for creating a welcoming and cheerful work environment. Special thanks go to the best office mate Dr. Maxime Grandin, my fellow doctoral researchers Harriet and Mr. Chaitanya Sishtla, as well as Lucile, Dr. Eleanna Asvestari, Dr. Diana Morosan, Dr. Daniel Price, Dr. Simon Good, Dr. Matti Ala-Lahti, and Dr. Erika Palmerio. Thank you for the support and fun "coffee" breaks! ♕

Last but not least, I sincerely thank my family for always supporting me during my studies. Kiitos isä ja äiti.

The research presented in this thesis has been supported by the Finnish Centre of Excellence in Research of Sustainable Space. Research visits, attending conferences, and building my international network have been made possible by travel grants from the University of Helsinki Doctoral School in Natural Sciences; the Emil Aaltonen Foundation; the Finnish Concordia Fund; the Vilho, Yrjö and Kalle Väisälä Foundation of the Finnish Academy of Science and Letters; the Magnus Ehrnrooth Foundation; and the Vela Fellowship of the Los Alamos National Laboratory.

Milla Kalliokoski
Helsinki, August 2022

List of Abbreviations

AE	Auroral Electrojet index (total)
AL	Auroral Electrojet index (westward)
CME	Coronal Mass Ejection
COI	Cone of Influence
CXD	Combined X-ray Dosimeter
Dst	Disturbance storm time index
ECT	Energetic Particle, Composition, and Thermal Plasma instrument suite
EMFISIS	Electric and Magnetic Field Instrument Suite and Integrated Science
EMIC	Electromagnetic Ion Cyclotron waves
GOES	Geostationary Operational Environmental Satellite
GPS	Global Positioning System
ICME	Interplanetary Coronal Mass Ejection
IMF	Interplanetary Magnetic Field
LANL	Los Alamos National Laboratory
MagEIS	Magnetic Electron Ion Spectrometer
MEPED	Medium Energy Proton and Electron Detector
MLT	Magnetic Local Time
NASA	National Aeronautics and Space Administration
Pc	Continuous Pulsations (ULF waves)
POES	Polar Operational Environmental Satellite
PSD	Phase Space Density
RBSP	Radiation Belt Storm Probes (Van Allen Probes)
REPAD	Relativistic Electron Pitch Angle Distribution
REPT	Relativistic Electron Proton Telescope
SYM-H	Symmetric disturbance index (H-component)
TS04	Tsyganenko and Sitnov (2005) magnetic field model
ULF	Ultra-Low Frequency
UT	Universal Time
VLF	Very Low Frequency
WFR	Waveform Receiver
WPI	Wave-Particle Interaction

List of Publications

This thesis is comprised of an introductory review of the outer radiation belt dynamics and three original research articles published in peer-reviewed international journals. The research articles are referred to in text by their Roman numerals and are presented below.

I Kalliokoski M. M. H., Kilpua E. K. J., Osmane A., Turner D. L., Jaynes A. N., Turc L., George H., Palmroth M. (2020), Outer radiation belt and inner magnetospheric response to sheath regions of coronal mass ejections: a statistical analysis, *Annales Geophysicae, 38*, 683–701, doi:10.5194/angeo-38-683-2020.

II Kalliokoski M. M. H., Kilpua E. K. J., Osmane A., Jaynes A. N., Turner D. L., George H., Turc L., Palmroth M. (2022), Phase space density analysis of outer radiation belt electron energization and loss during geoeffective and nongeoeffective sheath regions, *Journal of Geophysical Research: Space Physics, 127*, e2021JA029662, doi:10.1029/2021JA029662.

III Kalliokoski M. M. H., Henderson M. G., Morley S. K., Kilpua E. K. J., Osmane A., Olifer L., Turner D. L., Jaynes A. N., George H., Hoilijoki S., Turc L., Palmroth M. (2022), Outer radiation belt flux and phase space density response to sheath regions: Van Allen Probes and GPS observations, *Journal of Geophysical Research: Space Physics*, preprint: doi:10.1002/essoar.10511548.1.

Articles not included in this thesis

The author of this thesis has also worked on other research topics during the doctoral training in collaboration with other researchers which has led to the following publications.

1. George H., Kilpua E. K. J., Osmane A., Lejosne S., Turc L., Gradin M., **Kalliokoski M. M. H.**, Hoilijoki S., Ganse U., Alho M., Battarbee M., Bussov M., Dubart M., Johlander A., Manglayev T., Papadakis K., Pfau-Kempf Y., Suni J., Zhou H., Palmroth M. (2022), Estimating inner magnetospheric radial diffusion using a hybrid-Vlasov simulation, *Frontiers in Astronomy and Space Sciences, 9*, 866455, doi:10.3389/fspas.2022.866455.

2. Osmane A., Savola M., Kilpua E., Koskinen H., Borovsky J. E., **Kalliokoski M.** (2022), Quantifying the nonlinear dependence of energetic electron fluxes in the Earth's radiation belts with radial diffusion drivers, *Annales Geophysicae, 40*, 37–53, doi:10.5194/angeo-40-37-2022.

3. Grandin M., Palmroth M., Whipps G., **Kalliokoski M.**, Ferrier M., Paxton L. J., Mlynczak M. G., Hilska J., Holmseth K., Vinorum K., Whenman B. (2021), Large-scale dune aurora event investigation combining citizen scientists' photographs and spacecraft observations, *AGU Advances, 2*, e2020AV000338, doi:10.1029/2020AV000338.

4. George H., Kilpua E., Osmane A., Asikainen T., **Kalliokoski M. M. H.**, Rodger C. J., Dubyagin S., Palmroth M. (2020), Outer Van Allen belt trapped and precipitating electron flux responses to two interplanetary magnetic clouds of opposite polarity, *Annales Geophysicae, 38*, 931–951, doi:10.5194/angeo-38-931-2020.

5. Kilpua E. K. J., Juusola L., Grandin M., Kero A., Dubyagin S., Partamies N., Osmane A., George H., **Kalliokoski M.**, Raita T., Asikainen T., Palmroth M. (2020), Cosmic noise absorption signature of particle precipitation during interplanetary coronal mass ejection sheaths and ejecta, *Annales Geophysicae, 38*, 557–574, doi:10.5194/angeo-38-557-2020.

6. Kilpua E. K. J., Fontaine D., Moissard C., Ala-Lahti M., Palmerio E., Yordanova E., Good S. W., **Kalliokoski M. M. H.**, Lumme E., Osmane A., Palmroth M., Turc L. (2019), Solar wind properties and geospace impact of coronal mass ejection-driven sheath regions: variation and driver dependence, *Space Weather, 17*, 1257–1280, doi:10.1029/2019SW002217.

7. Kilpua E. K. J., Good S. W., Palmerio E., Asvestari E., Lumme E., Ala-Lahti M., **Kalliokoski M. M. H.**, Morosan D. E., Pomoell J., Price D. J., Magdalenić J., Poedts S., Futaana Y. (2019), Multipoint observations of the June 2012 interacting interplanetary flux ropes, *Frontiers in Astronomy and Space Sciences, 6*, 50, doi:10.3389/fspas.2019.00050.

8. Palmroth M., Praks J., Vainio R., Janhunen P., Kilpua E. K. J., Afanasiev A., Ala-Lahti M., Alho A., Asikainen T., Asvestari E., Battarbee M., Binios A., Bosser A., Brito T., Dubart M., Envall J., Ganse U., Ganushkina N. Yu., George H., Gieseler J., Good S., Grandin M., Haslam S., Hedman H.-P., Hietala H., Jovanovic N., Kakakhel S., **Kalliokoski M.**, Kettunen V. V., Koskela T., Lumme E., Meskanen M., Morosan D., Mughal M. R., Niemelä P., Nyman S., Oleynik P., Osmane A., Palmerio E., Peltonen J., Pfau-Kempf Y., Plosila J., Polkko J., Poluianov S., Pomoell J., Price D., Punkkinen A., Punkkinen R., Riwanto B., Salomaa L., Slavinskis A., Säntti T., Tammi J., Tenhunen H., Toivanen P., Tuominen J., Turc L., Valtonen E., Virtanen P., Westernlund T. (2019), FORESAIL-1 CubeSat mission to measure radiation belt losses and demonstrate deorbiting, *Journal of Geophysical Research: Space Physics, 124*, 5783–5799, doi:10.1029/2018JA026354.

1 Introduction

Space – the vast expanse of everything else in the universe – has always fascinated people on Earth. The concept typically evokes images of distant stars and galaxies, but this foreign environment begins very close to us. The near-Earth space is increasingly important to the modern, technology-based society. While it is hard to define a specific boundary where the Earth's atmosphere ends, conventionally the Kármán line at 100 km altitude is cited as the starting point of outer space.

Space physics is a field of science that focuses on the part of space closest to us, the solar system. Our own planet and its coupling to phenomena originating from the Sun are unquestionably a key focal point in this system which we want to understand. The incessant flow of ionized plasma from the Sun, known as solar wind, carries with it the solar plasma and magnetic fields into the interplanetary space. The solar wind interacts with the geomagnetic field and generates activity that for example manifests as the beautiful aurora. However, the near-Earth space and the variability within are hardly benign and present a space weather hazard. Nevertheless, this environment is a trove for all kinds of scientific interests on plasma dynamics – one which we can observe in situ.

Shortly after the start of the Space Age, intense radiation around the Earth was discovered by the Explorer 1 and Explorer 3 satellites in 1958 (Van Allen et al., 1958; Van Allen, 1959). The radiation signals were caused by energetic charged particles trapped by the Earth's magnetic field. Later, these regions of high particle fluxes, which span from about 1,000 km to 60,000 km (0.2–10 Earth radii or R_E) above the planet's surface, were termed the Van Allen radiation belts. Other planets, like Jupiter, also possess radiation belts.

The Earth's radiation belts are perhaps the most important space environment to us. A multitude of satellites orbit around the Earth through the radiation belts. Their numbers are quickly increasing with new players entering the business as launch costs are going down and the small and cheaper nanosatellites are becoming more popular. Especially the geostationary orbit, which is within the highly dynamic outer radiation belt, hosts many navigation and communication satellites because this orbit

allows them to stay above the same spot on Earth. At the same time, the outer belt poses a danger for these spacecraft due to the intense particle radiation. Charged particles can be accelerated in the belt to very high energies (from kiloelectronvolts to megaelectronvolts) via various processes, and they degrade the satellites and can cause single-event upsets (e.g., Baker et al., 2018).

The processes in the radiation belts that cause such energization or, on the other hand, mechanisms which cause particles to be lost from the system are not perfectly understood. Neither is it clear how external driving affects the radiation belts. This includes a lack of detailed knowledge on the processes that dominate in different parts of the system when a specific solar wind transient impacts the near-Earth space. Understanding these connections is the cornerstone for research efforts in improving space weather forecasting. Space weather is not only relevant for satellites, but also for astronauts passing through the radiation belts and even for infrastructure on the ground (e.g., Pulkkinen, 2007).

Furthermore, the outer radiation belt is a very variable system with changes occurring on a broad range of timescales from minutes to days. Especially, the mechanisms operating rapidly (< 1 h) are not well understood. This largely stems from the lack of observational capabilities with sufficiently high data density, which can only be reached by multi-satellite missions. Recently, particle data from navigation satellites has been made public (Morley et al., 2017), which enable new radiation belt science to be discovered.

The work presented in this thesis provides new information on how electrons in the outer radiation belt behave and which processes typically govern their dynamics when a certain type of solar wind transients hit the Earth. These key drivers of radiation belt activity are the turbulent and compressed sheath regions associated with interplanetary coronal mass ejections. The work explores the following topics:

- Typical sheath properties, geomagnetic activity and intensity of the induced plasma waves in the radiation belt system when sheaths impact the magnetosphere (Paper I).
- Response of the outer belt electron fluxes to sheaths (requiring consideration on short timescales) as a function of energy and radial location (Paper I and Paper III).
- Details of the physical processes governing the electron dynamics during the sheath impact (Paper II).
- The typical balance of adiabatic and nonadiabatic effects in the electron response to sheaths (Paper III).

- The dependency of the outer belt electron response on the geoeffectiveness of the sheaths (Papers I–III).

This thesis consists of an introductory part followed by the collection of the three original research articles referred to as Papers I–III. The introductory part is organized as follows. Chapter 2 introduces the central space physics topics considered in this thesis with emphasis on the relevant concepts for electron dynamics, such as wave-particle interactions, in the outer radiation belt. Also, it provides a brief overview of the structure of the near-Earth space and describes the properties of sheath regions. Chapter 3 outlines the different data sets and methods used in the research presented in this thesis. Next, Chapter 4 discusses the sheath events that were selected for the studies and how they impact the outer radiation belt. Namely, the associated wave activity and changes in the electron fluxes are summarised. The response is considered both for all the selected sheath events and for subsets of the sheaths where the division is based on the sheath geoeffectiveness. Chapter 5 discusses the outer belt electron response to sheaths when considering the electron phase space density, which is a derived quantity that sheds light on the nonadiabatic processes. Again, the geoeffectiveness of the sheaths is taken into account. Chapter 6 provides a summary of the key results presented in this thesis and reviews the impact of this work. The following outlook discusses interesting and important future possibilities for further studies. Finally, Chapter 7 concludes the introductory part by summarising Papers I–III and the author's contribution to each study.

2 Earth's radiation belt system

The radiation belts and the impact of sheath regions on them are the focus of this thesis. This chapter introduces the radiation belt system and the electron dynamics in the geomagnetic field and in response to wave-particle interactions and other processes. Also, the solar wind as a driver of activity in the radiation belt system, especially focusing on the sheath regions, is briefly discussed. This background supports the understanding of the research results provided in later chapters.

2.1 Magnetosphere and radiation belts of the Earth

The Earth's intrinsic magnetic field produces a cavity around our planet that shields us from the solar wind. This region is called the magnetosphere and it is defined as the region where the motion of charged particles is dominated by the geomagnetic field instead of the interplanetary magnetic field (Gold, 1959). The geomagnetic field is roughly dipolar, but the solar wind compresses the magnetosphere on the sunward side and stretches it out on the opposite side, creating the long magnetotail. The magnetopause is the outer boundary of the magnetosphere, and it represents the layer where the pressures of the geomagnetic field and solar wind are balanced. The location of the subsolar magnetopause varies, and strong dynamic pressure in the solar wind pushes the magnetopause Earthward (Shue et al., 1998). Outside the magnetopause there is the magnetosheath and the bow shock. In this thesis we focus on the inner magnetosphere.

In the inner magnetosphere, charged particles are trapped by the geomagnetic field with their motion bound by the magnetic field lines (see Section 2.2.1). They create torus-like regions around the Earth that are called the radiation belts. The belts are illustrated in Figure 2.1. The radiation belts are divided in two regions. The inner belt is dominated by high-energy protons (> 10 MeV) and it is relatively quiescent (e.g., Selesnick and Albert, 2019). The outer belt is dominated by energetic electrons from 10s of keV to several MeV, and the electron fluxes vary widely driven by geomagnetic activity and solar wind transients (e.g., Reeves et al., 2003; Turner

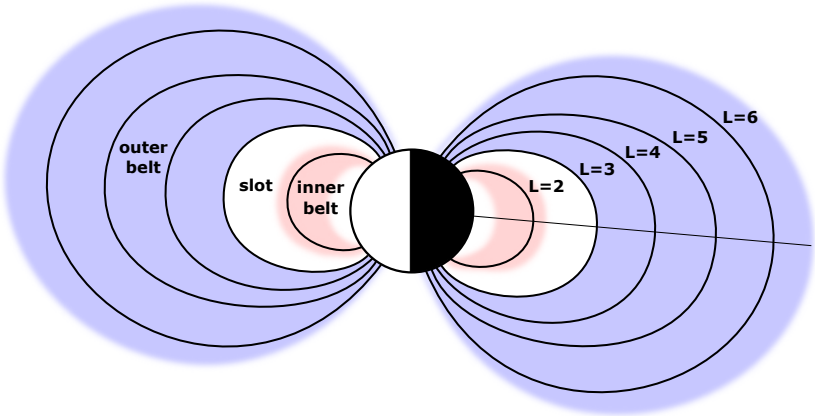

Figure 2.1: Illustration of the Earth's radiation belts. Black curved lines depict the geomagnetic field and the colored areas represent regions with high particle fluxes, showing the inner and outer belt. The L-shells of the field lines are indicated.

et al., 2019). There is a slot region between the inner and outer belts where the particle fluxes are low. The extent of the slot region depends on energy, and it also sometimes gets filled with electrons during strong activity (e.g., Reeves et al., 2016). At times, a third belt appears (Baker et al., 2013b). This three-belt structure forms via the loss of high energy particles; there is a remnant belt consisting of the leftover flux closer to the Earth, while at the outermost part of the outer belt fluxes are replenished.

When electron fluxes in the radiation belts are discussed, the location under consideration is usually described with the McIlwain's L parameter in reference to the geomagnetic field. The L parameter is defined as the distance from the dipole center to the equatorial point of the considered field line (McIlwain, 1961). That is, a single field line corresponds to a single L-shell. For more realistic, nondipolar fields, the generalized quantity is the Roederer's L^* parameter (Roederer, 1970). This however does not indicate spatial location and it is more typically used for phase space density rather than fluxes (see Sections 2.2.1 and 2.2.2). While the extent of the belts depend on energy, generally the inner belt is at $L = 1$–2 and the outer belt around $L = 3$–8 with the slot region in between. The intense region at $L = 3.5$–5 is often called the heart of the outer belt.

Other inner magnetospheric regions that are worth noting here are the ring current and the plasmasphere. The main carriers of the ring current are positive ions

drifting around the Earth (Daglis et al., 1999). Changes in ring current affect the magnitude of the equatorial geomagnetic field, which is monitored as an indication of geomagnetic activity (e.g., Dst and SYM-H indices; see Section 2.3.1). The plasmasphere consists of low-energy (~ 1 eV) and high-density plasma which co-rotates with the Earth. The plasmapause is the boundary of this region, characterized by an order of magnitude change in the plasma density. The location of the plasmapause depends on geomagnetic activity (e.g., O'Brien and Moldwin, 2003). The plasmapause is an important threshold for radiation belt dynamics. This is because different plasma waves causing contrasting wave-particle interactions occur inside and outside the plasmasphere (see Section 2.2.3). The ring current and plasmasphere are not spatially separate from the radiation belts and these regions overlap.

The inner magnetosphere also houses various plasma waves that can interact with the radiation belt particles (see Section 2.2.3). The generation of these waves is driven by both internal and external processes and instabilities, and some waves are more common in specific parts of the magnetosphere. Wave-particle interactions are key processes in energizing the outer belt electrons which, in turn, can be hazardous for satellites in the belt. Understanding conditions in the radiation belts is a substantial part for being able to forecast space weather. The particle dynamics relevant for the work presented in this thesis are discussed next.

2.2 Particle dynamics in the radiation belt system

Charged particles in the Earth's radiation belts are strongly governed by the geomagnetic field. In this section, the main characteristics of particle motion, the phase space density as a quantity to represent the particle dynamics and the different physical processes acting on electrons in the radiation belts are introduced.

2.2.1 Adiabatic invariants

Adiabatic invariants are constants of motion when changes in the investigated parameter occurs slowly. In the magnetospheric context, they describe the three fundamental quasi-periodic motions of charged particles in the geomagnetic field: 1) gyration about magnetic field lines, 2) bounce along the field lines, and 3) drift about the Earth. These components of the particle trajectories are illustrated in Figure 2.2. The combined motions are said to create a drift shell. When all invariants are conserved (i.e., changes are slow), the drift shell is stable and can be used for predicting particle trajectories. Here slow changes refer to variations on much longer timescales than is associated with these three fundamental motions. Drift is the slowest process,

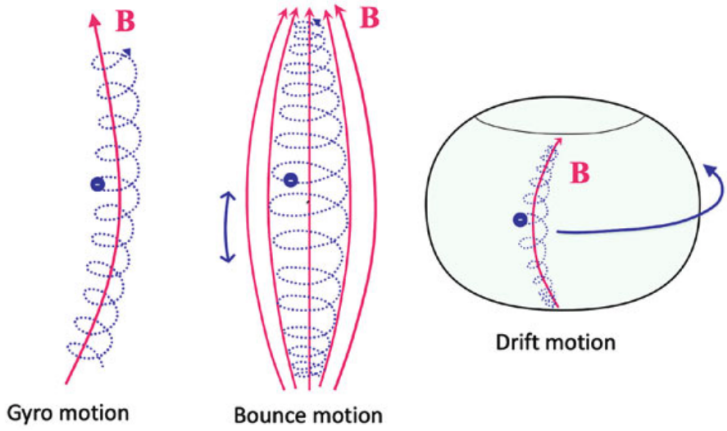

Figure 2.2: Gyration around a magnetic field line, bounce motion along the field line bounded by the magnetic mirrors of stronger field between the hemispheres and drift around the Earth are the fundamental components of charged particle motion in the Earth's radiation belt system. Each of these motions is associated with a constant of motion, i.e., with the three adiabatic invariants μ, K and L^*, respectively. Reproduced from Koskinen and Kilpua (2022).

while gyration is the fastest. The timescales for a particle depends on its energy and where in the radiation belts it is located (L-shell). For a 1 MeV electron in the heart of the outer belt at $L = 4$, the drift period is about 16 minutes, the bounce period about 0.27 seconds and the gyration period about 0.22 milliseconds.[1] Clearly, the invariant associated with drift motion is the easiest to violate, causing changes in the distribution of radiation belt particle populations (see Section 2.2.3). The following presents the definitions of the adiabatic invariants, which can be found in more detail in textbooks on the subject, for example, Roederer (1970) and Koskinen and Kilpua (2022).

The first adiabatic invariant is the magnetic moment corresponding to the gyration around a field line. It is given by

$$\mu = \frac{p_\perp^2}{2m_0 B} = \frac{p^2 \sin^2 \alpha}{2m_0 B}, \tag{2.1}$$

where $p_\perp$ is the component of relativistic momentum that is perpendicular to the

[1]These periods are approximated for an equatorial electron in a dipole field using the online calculator provided by Solène Lejosne: `https://solenelejosne.com/bounce/`

magnetic field, m_0 is particle's rest mass, B is the magnetic field magnitude and α is the pitch angle. Pitch angle is the angle between the magnetic field and the particle's velocity. As μ is a constant, given that there is no very rapid changes in the geomagnetic field, Equation 2.1 can be used to find the pitch angle of a particle at some other point than where its pitch angle is known:

$$\frac{\sin^2 \alpha_0}{B_0} = \frac{\sin^2 \alpha}{B}. \tag{2.2}$$

Conservation of μ implies that the perpendicular momentum must increase when the particle travels towards an intensifying magnetic field. At a strong enough point in the magnetic field, the parallel momentum becomes zero and the particle can no longer continue along the field line – it bounces back. This point in the magnetic field is called the magnetic mirror point (B_m). Since the geomagnetic field strengthens towards the Earth, particles typically have mirror points at each hemisphere which form a magnetic bottle where the particle bounces back and forth. If a particle travels very fast along the magnetic field line, it might be lost to the atmosphere before mirroring. Such particles are said to be in the bounce loss cone, and they are lost due to collisions with atmospheric particles.

The second adiabatic invariant corresponds to this bounce motion along the field line. It is given by

$$J = \oint p_{\parallel} ds, \tag{2.3}$$

where $p_{\parallel}$ is the component of relativistic momentum that is parallel to the magnetic field and ds is distance along the field line. It is customary to express the second invariant as only a function of magnetic field (when μ is conserved) as follows

$$K = \frac{J}{2\sqrt{2m_0\mu}} = \int_{s_m}^{s'_m} \sqrt{B_m - B(s)}\, ds. \tag{2.4}$$

Here s_m and s'_m are the distances of the particle's mirror points where the particle bounces, and $B(s)$ and B_m are magnetic field magnitudes at point s along the field line and at the mirror point, respectively.

The third invariant is the magnetic flux enclosed by the particle's drift shell and is given by

$$\Phi = \oint \vec{A} \cdot d\vec{l} = \int \vec{B} \cdot d\vec{S}, \tag{2.5}$$

where $\vec{A}$ is the magnetic vector potential, $d\vec{l}$ is the curve along the particle guiding center drift shell, $\vec{B}$ is the magnetic field vector and dS is the area enclosed by the drift shell. Stokes theorem is used to get the second form of the integral. In radiation belt studies, it is typical to consider a quantity that is inversely proportional to the magnetic flux:

$$L^* = \frac{2\pi M}{|\Phi| R_E}, \tag{2.6}$$

where M is the magnetic moment of the Earth's dipole field and R_E is the radius of the Earth. This presentation of the third invariant is termed L^*, or Roederer's L parameter, which is the radial distance to the equatorial point where the particle would be found if all nondipolar perturbations in the geomagnetic field were adiabatically turned off leaving only the dipole field (Roederer, 1970). It should be noted that in a nondipolar field L^* does *not* represent a spatial coordinate, instead L^* is a property of a stably trapped particle (Roederer and Lejosne, 2018). That is, in absence of acceleration or loss processes, L^* defines a surface with constant phase space density. If a particle will encounter a boundary of the radiation belt system (i.e., the magnetopause or the atmosphere) during its drift leading to its loss from the system, the particle does not have an L^* value. The particle is said to be in the drift loss cone.

Therefore, the L and L^* parameters coincide in a dipole field, but in a nondipolar field, which is a more realistic description of the Earth's magnetic field especially during geomagnetically active times, these parameters are different. Typically, L is used with particle fluxes whereas L^* is better suited for phase space density (see Section 2.2.2).

To summarize, the three adiabatic invariants are μ, K and L^*. They describe the kinematic state of a particle in the geomagnetic field. During slow changes in the radiation belt system, the invariants are conserved which means that particles on a certain drift shell will remain on that drift shell. If there are disturbances (e.g., plasma fluctuations) with shorter or comparable timescales than the characteristic invariant timescales, the invariance is violated and particles can move to different drift shells. This variation is *nonadiabatic* and thus introduces irreversible changes[2] in the radiation belt system, such as acceleration, loss or radial diffusion. Generally, violation of the third invariant is associated with radial diffusion, violation of the second and first invariants with pitch angle diffusion, and violation of the first invariant with resonant high-frequency interactions and drift. The key wave-particle

[2]Irreversibility is defined for a particle population; a single particle can always revisit its initial state.

interactions governing electron dynamics in the radiation belts are discussed in Section 2.2.3.

It is noted that μ can be fully derived from observational data (given that magnetometer and pitch angle resolved particle data are available), but K and L^* require knowledge of the global geomagnetic field as the particle's trajectory needs to be traced. Observations provide only local information and therefore geomagnetic field models are needed.

The adiabatic invariants are useful, for example, in the calculation of phase space density as will be detailed in the following section. The invariants provide an adiabatic coordinate space for phase space density. To be precise, the invariants describe the momentum space and an additional three coordinates are needed for the spatial space in order to construct the full six-dimensional phase space. These spatial coordinates are called the phase angles ϕ_i related to the gyration, bounce and drift motion. As long as μ, K and L^* are adiabatic invariants, phase space density can be averaged over the phase angles, and therefore the momentum coordinate space (μ, K, L^*) is sufficient for representing a phase-averaged phase space density. In this thesis, the phase space coordinates are considered to refer only to the momentum coordinates (μ, K, L^*).

2.2.2 Phase space density

Phase space density (PSD) is a quantity that allows more detailed investigation and interpretation of radiation belt electron dynamics than just the electron flux measurements. It combines the measurements with information from global modeling in a specific way in order to transform the flux recorded as a function of energy in the spatial domain into a coordinate system closely related to the motion of the particles in the geomagnetic field – the phase space coordinates. The key point is that PSD is expressed in terms of the adiabatic invariants and thus remains constant under adiabatic changes. Only nonadiabatic processes (which violate at least one of the invariants) impact the value of PSD and the nature of these processes can be identified by analysing the evolution of PSD and the shape of its radial profiles.

Fundamentally, PSD is defined as the particle flux j divided by the squared relativistic momentum p, i.e.,

$$f = \frac{j(E, \alpha, \vec{x}, t)}{p^2}, \tag{2.7}$$

where the flux is measured as a function of energy E, pitch angle α, location $\vec{x}$ and time t. The relativistic momentum is given by

$$p^2c^2 = E^2 + 2m_0c^2E, \tag{2.8}$$

where E is the kinetic energy of the particle. The total energy of the particle is the kinetic energy combined with the rest energy (m_0c^2).

However, additional steps need to be taken for a more complete view of the radiation belt dynamics. That is, the PSD given by Equation 2.7 will correspond to different adiabatic invariants at different times, and as such does not provide much further information than the flux itself. Instead, PSD should be properly transformed into the phase space coordinates: $f(\mu, K, L^*, t)$.[3]

The real power of PSD is achieved when PSD is calculated from the flux measurements while retaining the first and second adiabatic invariants as constants. This allows investigation of the PSD as a function of the third invariant, L^*. The shape of the radial profile (PSD vs L^*) reveals if enhancement and losses are local or occur at a larger scale, and what are the likely physical processes contributing to the acceleration, transport and loss of particles in the radiation belts (e.g., Chen et al., 2007; Turner et al., 2012; Shprits et al., 2017).

Signature PSD radial profiles are shown in Figure 2.3. For example, local acceleration produces a local peak in the profile, while a local dip is caused by local loss, though the identification can sometimes be complicated. These processes and their causes are further discussed in Sections 2.2.3 and 2.2.4.

The PSD calculation procedure is described in many publications (e.g., Green and Kivelson, 2004; Chen et al., 2005; Green, 2006; Hartley and Denton, 2014), and the implementation depends on the used data set. In the work presented in this thesis, original programs have been created for the calculations. Section 3.2.4 provides the particulars of the implementation for two different data sets employed in Paper II and Paper III. The PSD calculation can be in general summarised with the following steps which are repeated for each time step:

1. Choose K and determine the corresponding pitch angle.
2. Choose μ and determine the corresponding particle energy.
3. Compute the corresponding L^*.
4. Calculate PSD with Eq. 2.7.

Thus, the starting point is to choose the μ and K values where PSD is computed. The choice of these invariants reflects which particle populations the PSD represents.

[3]Note that the notation for phase averages is dropped for simplicity.

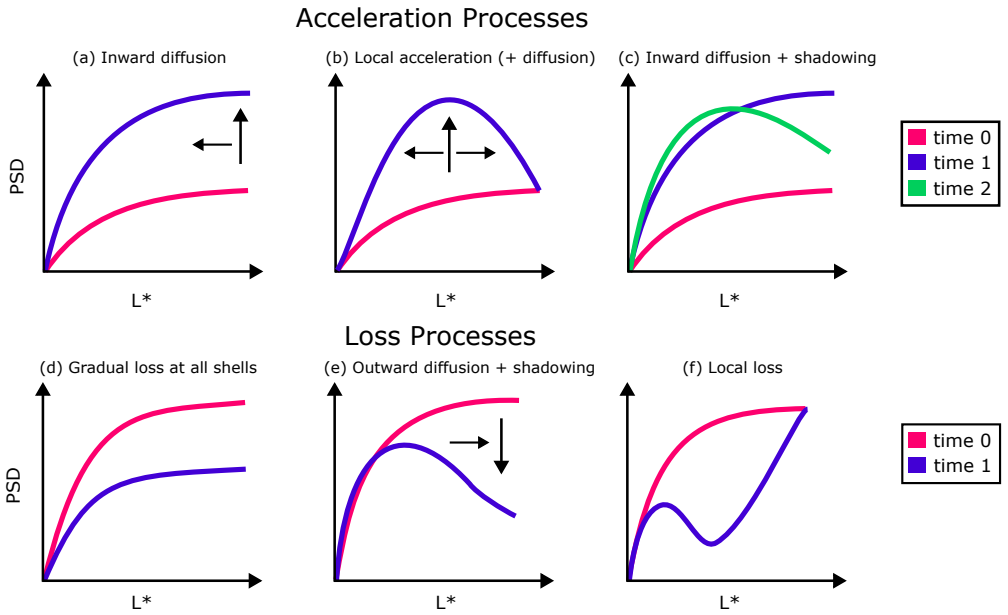

Figure 2.3: Schematics of the temporal evolution of PSD as a function of L^* to illustrate the identification of different processes acting on radiation belt particles. (a) Increasing PSD with a positive gradient indicates substorm injections and inward radial diffusion (but a negative gradient at L^* values higher than observed cannot be ruled out). (b) A local peak is a result of local acceleration (but care must be taken in the interpretation because peak-like features can be caused also by other processes). (c) When the processes featured in panel a are accompanied by loss at high L^*, a peak-like profile can form. (d) Gradual loss at all L^* indicates pitch angle scattering by hiss and chorus waves. (e) Sudden loss at high L^* indicates loss to the magnetopause, typically due to the combination of the compression of the magnetopause and outward radial diffusion. (f) A local dip is a result of local loss. Reproduced from Koskinen and Kilpua (2022).

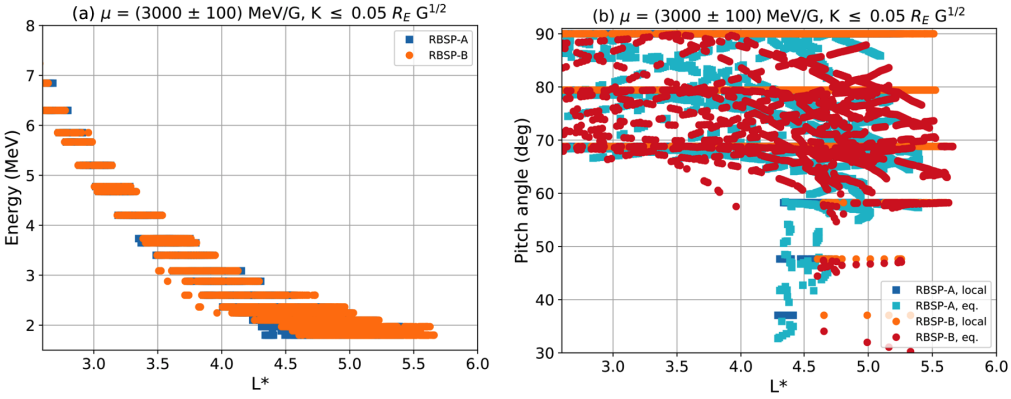

Figure 2.4: Illustration of the ranges in energy and pitch angle corresponding to chosen μ and K values. This example uses RBSP data and considers near-equatorially mirroring relativistic electron populations with $\mu = 3000$ MeV/G and $K \leq 0.05$ R$_E$G$^{1/2}$. (a) Electron energies range in this case in 1–7 MeV. (b) Pitch angles range from 30° to 90°. Equatorial pitch angles are derived from the observed local pitch angles.

Higher μ values indicate higher-energy populations, but the energy corresponding to the chosen μ depends on L^* and the range can be large. Low values of K indicate particles that have pitch angles close to 90°, i.e., particles that mirror near the equator. Again, there is a range of pitch angles that correspond to the chosen K. Figure 2.4 provides an example of these ranges.

As discussed earlier, a global geomagnetic field model is a requirement for calculating K and L^*, and thus needed for computing PSD. For K, the electron bounce motion is traced along a field line to the mirror point (which allows finding the pitch angles corresponding to the chosen K), and the electron drift shell is traced for L^*. For μ, the local magnetic field magnitude can be taken either from the employed model or from actual spacecraft measurements if available. The studies presented in this thesis use the TS04 model (Tsyganenko and Sitnov, 2005) which describes the nondipolar magnetospheric magnetic field also during geomagnetically active times. It takes solar wind parameters as input. The TS04 model provides the external field and it is combined with a model of the internal field given by the International Geomagnetic Reference Field (Finlay et al., 2010).

Uncertainties in particle measurements originating from instrumental issues naturally carry over to the PSD values, but the main source of uncertainty is the geomagnetic field model. Satellite observations cannot provide the necessary information of

the magnetic field on the global scale, and it is therefore also difficult to determine how accurately the field model represents the real geomagnetic field at any given moment. Uncertainty grows during geomagnetically active times when the field becomes more complex. The model can be tested with the PSD matching technique where PSD from inter-calibrated spacecraft are compared. If the satellites are in magnetic conjunction (matching phase space coordinates), they are expected to observe the same PSD. Deviations indicate inaccuracy in the adiabatic invariants.[4] Morley et al. (2013) tested various geomagnetic field models using PSD matching and showed that the TS04 model performed the best.

Additional use of modeling (e.g., when the considered spacecraft does not have a magnetometer or a pitch-angle resolved particle instrument) introduces further uncertainty. For example, a modeled pitch angle distribution may not always sufficiently represent the true distribution. Similarly, poor instrumental resolution in energy or pitch angle propagate into poor resolution in the computed PSD. Hence, resolution can be artificially increased (see Section 3.2.4). Limited L^* coverage can complicate the interpretation of PSD profiles as important gradients might not be resolved. This can be alleviated by combining data from two missions with different L^* ranges (e.g., Boyd et al., 2018; Turner et al., 2021). All in all, uncertainties from different sources are propagated from step to step in the calculation of PSD and it is difficult to derive conclusive error bars.

2.2.3 Waves and wave-particle interactions

There exist multiple modes of electromagnetic waves in the magnetosphere. These waves are generated by different source processes and they interact differently with the charged particles in this region. Typically, solar wind driving and subsequent geomagnetic activity excite waves, which cause a dynamic response of the radiation belt particles. Wave-particle interactions (WPI) can lead to the acceleration, transport or loss of particles in the radiation belts, which means they violate the adiabatic invariants. Lower frequency waves can violate the third adiabatic invariant and thus disrupt the stable drift shells and enable radial diffusion. Higher frequencies are required to violate the second and first invariants whose characteristic timescales are much shorter, and the particles can subsequently gain energy or experience scattering loss depending on the interaction. Different wave modes can also act in synergy or one can impede the effects of another (e.g., Jaynes et al., 2015; Zhang et al., 2019).

[4] It is also possible that discrepancy between the PSD values emerges due to nonadiabatic processes, but they must occur on timescales less than the drift time of the particles between the two spacecraft.

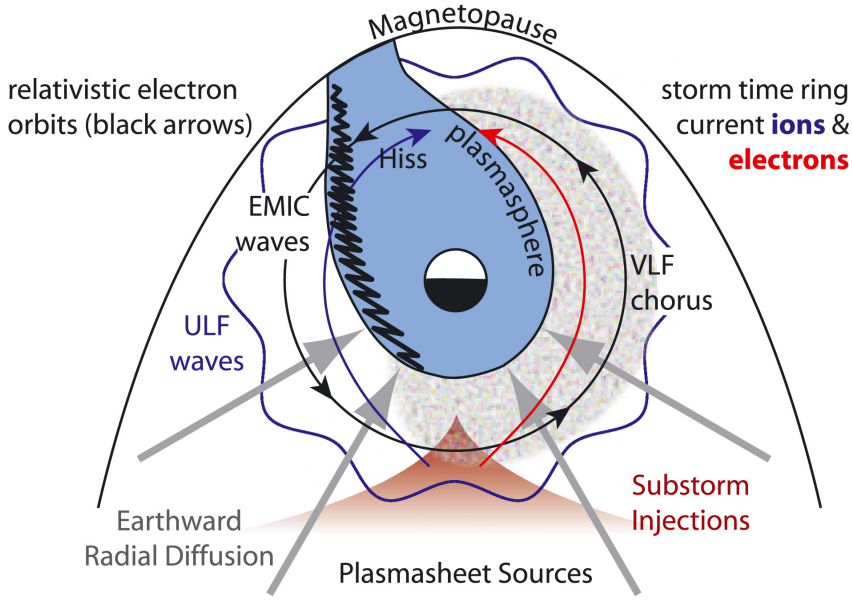

Figure 2.5: Illustration of the typical location of different plasma wave modes in the Earth's inner magnetosphere in the equatorial plane. Earth is in the center with dusk on the left and dawn on the right. ULF waves can occur throughout the magnetosphere. EMIC waves are depicted with the thick black lines on the day and dusk side, and they can occur also outside the plasmasphere. Plasmaspheric hiss occurs inside the plasmasphere (blue region) and chorus waves occur outside it, typically on the dawn side (grey region). Reproduced from Reeves et al. (2016) with permission (Copyright 2015. The Authors).

Therefore, the radiation belts are a highly complex system, and predicting electron dynamics is extremely difficult.

Different waves dominate in different regions of the radiation belt system, for example, inside and outside the dense plasmasphere. The typical regions where the key wave modes occur are presented in Figure 2.5. In the following, the wave modes and the related wave-particle interactions with the outer belt electrons (reviewed in, e.g., Thorne, 2010) investigated in this thesis are presented. Additionally, this section discusses how these dynamic processes can be identified from radial profiles of PSD.

Ultra-low frequency (ULF) waves, also known as geomagnetic pulsations, can permeate the entire magnetosphere. ULF waves are classified into two groups with continuous (Pc 1–5) or irregular (Pi 1–2) pulsation periods (Jacobs et al., 1964). For radiation belt electrons, the most important ULF waves are the continuous Pc5

pulsations whose frequencies are in the range 2–7 mHz and Pc1–2 pulsations whose frequencies are in the range 0.1–5 Hz.

The Pc5 waves can be observed by both in situ and ground-based magnetometers.[5] Various perturbations in the magnetospheric system generate them, for example, Kelvin-Helmholtz instability at the magnetopause (Claudepierre et al., 2008; Wang et al., 2017) or the impact of solar wind shocks and pressure pulses on the magnetosphere (Kepko and Spence, 2003; Claudepierre et al., 2010). Pc5 waves can resonate with the drift motion of radiation belt electrons. This can transport electrons nonadiabatically to different drift shells (i.e., different L^*), which leads to both inward and outward radial diffusion. In this case the third adiabatic invariant is violated. Inward radial diffusion energizes electrons (e.g., Su et al., 2015). Conversely, the electron energy decreases with outward diffusion. The timescale of electrons to diffuse over one L-shell varies from hours to days. The effects of radial diffusion were formulated soon after the discovery of the radiation belts (e.g., Fälthammar, 1965), and are quantified by theoretical and empirical radial diffusion coefficients (see, e.g., Lejosne and Kollmann, 2020, for a review). In regard to the PSD radial profiles, radial diffusion driven by ULF waves acts to flatten steep gradients and peaks. Typically, both inward and outward transport occur simultaneously, and PSD increasing at low L^* is an indication that ULF-driven outward radial diffusion is contributing to losses at high L^* (Turner and Ukhorskiy, 2020); see also Section 2.2.4.

Electromagnetic ion cyclotron (EMIC) waves (Pc1–2 pulsations) are predominantly excited in the equatorial day side and dusk side magnetosphere. They are generated by temperature anisotropies of energetic magnetospheric protons, both inside and outside the plasmasphere (e.g., Engebretson et al., 2008; Pickett et al., 2010) and are observed by space and ground-based magnetometers similar to ULF Pc5 waves. Resonant pitch angle scattering by EMIC waves drives loss of relativistic and ultrarelativistic electrons into the atmosphere (Usanova et al., 2014; Blum et al., 2019). EMIC-driven sudden losses appear as local dips in PSD radial profiles (Aseev et al., 2017; Shprits et al., 2017), as seen in panel f in Figure 2.3. Kurita et al. (2018) showed that fast loss at ultrarelativistic energies can occur at a timescale of a few tens of minutes.

Whistler mode chorus waves occur outside the plasmapause mostly on the equatorial dawn side. They are very low frequency (VLF) waves. During substorm activity, source (10s of keV) and seed (100s of keV) electrons are injected into the radiation belts from the plasma sheet (e.g., Baker et al., 1996). The source population excites

[5]For how to derive the strength of wave activity from magnetometer measurements, see Section 3.2.1.

chorus waves in two bands: the lower band at 0.1–0.5 f_{ce} and the upper band at 0.5–0.8 f_{ce} with a minimum in wave power at 0.5 f_{ce} (Burtis and Helliwell, 1969; Tsurutani and Smith, 1974; Koons and Roeder, 1990), where f_{ce} is the electron cyclotron frequency. Li et al. (2019) proposed that the two-band structure arises from the initially excited chorus waves interacting with the underlying source population via Landau damping, which then causes the gap. Lower and upper band chorus have different wave properties, like the wave normal direction (Li et al., 2016b). The chorus waves accelerate seed electrons progressively to relativistic energies at > 1 MeV (Miyoshi et al., 2013; Jaynes et al., 2015), which can take hours or days (e.g., Li et al., 2014, 2016a). Chorus also scatters low-energy (10s to 100s keV) electrons into the loss cone where they precipitate into the upper atmosphere (Lam et al., 2010). The local acceleration via wave-particle interactions creates a peak in the PSD radial profile as shown in panel b in Figure 2.3. Interpretation of peaks must be performed carefully because local peak-like PSD signatures can emerge also from other processes, such as loss at the magnetopause at high L^* (see the resultant PSD peak in panel c in Figure 2.3). In addition, a wide enough range of L^* values are needed to capture the possible peak. A limited L^*-range can lead to misinterpretation of the electron response. Thus, good coverage of observations of chorus activity is important in the determination of the likely process leading to the peak formation. Chorus activity is typically determined from the in situ spacecraft data, but in the absence of sufficiently extensive observations, the global chorus activity can be estimated by using the precipitating electrons as a proxy (e.g., Li et al., 2013a; Chen et al., 2014b; Ni et al., 2014).

Plasmaspheric hiss waves are incoherent whistler mode emissions that occur inside the plasmasphere at frequencies from about 100 Hz to 0.1 f_{ce}. Hiss is suggested to be generated from chorus waves evolving into hiss when they enter the plasmasphere (Bortnik et al., 2008; Zhou et al., 2016). Plasmaspheric hiss is responsible for the slow gradual decay of the outer belt electron content (e.g., Meredith et al., 2006), as illustrated in panel d in Figure 2.3). When geomagnetic activity subsides, the plasmapause typically expands and an increasingly larger region of radiation belt electrons is exposed to hiss. In contrast to the other waves discussed in this section, hiss operates on longer timescales of a few days (Jaynes et al., 2014).

2.2.4 Magnetopause shadowing

Previously, wave-particle interactions were discussed as key mechanisms leading to electron acceleration, transport and losses. Waves primarily cause losses by scattering electrons from the belts into the atmospheric loss cone. Another key radiation belt

loss mechanism is magnetopause shadowing, described briefly here.

Magnetopause shadowing is a term that describes the loss of radiation belt particles when they cross the magnetopause and are lost to the solar wind. This can happen either when the magnetopause is pressed closer to the Earth or when particles are transported to large L-shells. The inward incursion of the magnetopause occurs when a shock or pressure pulse hits the magnetopause compressing it (Shue et al., 1998), or during periods of strongly southward interplanetary magnetic field when the magnetopause is gradually eroded by magnetic reconnection on the day side. The strongest compressions occur when these two processes work in tandem. As a consequence, the drift paths of electrons trapped in the geomagnetic field can become intercepted by the magnetopause as it moves closer to the Earth. The primary wave mode causing outward radial transport are the ULF Pc5 waves. They can bring electrons from the inner parts of the outer belt to the magnetopause which these particles would not otherwise encounter. Additionally, the adiabatic Dst effect (Kim and Chan, 1997) can result in irreversible losses from the radiation belts. In the Dst effect, the ring current increases during the main phase of a geomagnetic storm and the geomagnetic field weakens, causing the electrons to move outward in order to conserve the third adiabatic invariant. This effect is adiabatic, meaning that the electrons return to their original location after the geomagnetic activity subsides. However, when the electrons are moving outward during the Dst effect, they can encounter the magnetopause and be lost (e.g., Kim et al., 2010).

Typically, magnetopause shadowing losses are caused by the combination of a compressed or eroded magnetopause and ULF-driven outward transport (e.g., Turner et al., 2012; Turner and Ukhorskiy, 2020). This is often the case as pressure pulses and shocks cause both compression and excite Pc5 waves. In PSD radial profiles, loss to the magnetopause appears as a large, orders of magnitude dropout at high L^* (see panel c and e in Figure 2.3). The dropout is typically abrupt (a few hours) and the effect is typically seen at all energies. Contribution of the ULF-driven outward diffusion to the loss can be identified from PSD increasing at low L^* through inward diffusion (indicated in panel c in Figure 2.3).

The lowest L^* where magnetopause shadowing losses are expected is better indicated by the last closed drift shell (LCDS) rather than the magnetopause location (e.g., Olifer et al., 2018). LCDS represents the largest L^* where a radiation belt population remains stably trapped in a given geomagnetic field configuration and particles at larger distances will be lost within one drift orbit. Computing LCDS requires geomagnetic field modeling (e.g., Albert et al., 2018).

2.3 Solar wind drivers of radiation belt variability

Solar wind – plasma and magnetic fields – flowing from the Sun plays a key role in disturbing the Earth's magnetosphere, which can subsequently lead to strong dynamics in the radiation belts. An important factor in this is the southward directed interplanetary magnetic field (IMF), which facilitates magnetic reconnection on the day side magnetosphere. The Earth's magnetic field points northward, and in reconnection, oppositely directed magnetic field lines interact, and as a consequence their topology changes. This allows solar wind energy, mass and momentum to transfer into the magnetosphere and causes large disturbances in the geomagnetic field.

Large-scale structures in the solar wind are the key drivers of the magnetospheric disturbances. These include the interplanetary counterparts of coronal mass ejections (CMEs), which are huge plasma clouds released from the Sun in violent eruptions, and their sheath regions, as well as co-rotating interaction regions between slow and fast solar wind and the following fast streams. These structures have distinct solar wind properties, and therefore lead to different responses of the geospace environment, including the response of the radiation belt electron fluxes (e.g., Kataoka and Miyoshi, 2006; Kilpua et al., 2015, 2017a; Shen et al., 2017; Bingham et al., 2018; Turner et al., 2019).

The focus of this thesis is on sheath regions. The following sections discuss geomagnetic activity in general, defining the concept of geoeffectiveness as used in this thesis, and introduce the characteristics of sheaths. Properties of sheaths and their effect on radiation belt electrons as shown by the work conducted for this thesis are further discussed in Chapters 4 and 5.

2.3.1 Geomagnetic activity

The largest disturbances in the magnetosphere are called geomagnetic storms. They are defined as decreases in the horizontal component of the geomagnetic field due to enhancements of the equatorial ring current. Storms last at least several hours, but they can have durations of several days with more intense storms typically lasting longer (e.g., Haines et al., 2019). The storm period often commences with a brief (a few hours) increase in the horizontal geomagnetic field component due to the impact of a shock or pressure pulse leading the large-scale solar wind structure. The subsequent main phase of a storm, when the horizontal component decreases, is usually relatively short compared to the more gradual recovery phase.

Smaller scale variability on shorter timescales (a couple of hours) is caused by substorms, which are a more frequent occurrence than storms (Partamies et al.,

2013). Substorms can occur both during storm and non-storm times. For more in depth explanation of storm and substorm onset mechanisms, the reader is encouraged to review textbooks on the subject such as Koskinen (2011). During substorms, particles are injected into the radiation belts from the plasma sheet, which generate waves and replenish the electron content in the radiation belts after dropouts (e.g., Forsyth et al., 2016). As such, they are important contributors to the radiation belt electron dynamics.

The level of the disturbance in the magnetosphere due to changes in the ring current is monitored by geomagnetic activity indices such as Dst or SYM-H (Iyemori, 1990). These indices are derived from ground-based measurements of the geomagnetic field at low and mid-latitudes, and they are similar except that Dst is available at 1-hour resolution and SYM-H at 1-minute resolution. The more negative the index, the more active the system is and the stronger variability can be observed. Gonzalez et al. (1994) classified that moderate storms reach Dst < -50 nT and small storms Dst < -30 nT. Substorm activity is monitored from geomagnetic indices derived from higher latitude observatories to capture variations in the auroral electrojet currents in the ionosphere.

In this thesis, the SYM-H and AL indices are used for storm and substorm activity, respectively, where the latter index records the strength of the westward auroral electrojet. The events where the minimum SYM-H is below -30 nT are termed *geoeffective*. If SYM-H remains above -30 nT during an event, that event is called *nongeoeffective*. Many studies on the radiation belt variability focus on events associated with strong geomagnetic storms. However, significant changes in radiation belt electron content do not require strong storms (e.g., Schiller et al., 2014; Anderson et al., 2015; Katsavrias et al., 2015) and they can occur also during geomagnetically quiet times. For example, solar wind structures with high dynamic pressure can compress the magnetosphere significantly and induce plasma waves, although they would not have southward IMF and cause no geomagnetic storm. The effects of nongeoeffective events are also emphasized in the work presented in this thesis.

2.3.2 Sheath regions driven by interplanetary coronal mass ejections

When observed directly in the solar wind, CMEs are called interplanetary coronal mass ejections (ICMEs). They are regular structures in the interplanetary space, but their occurrence rates vary with the solar activity with a few clear ICMEs detected per year during solar minimum compared to several ICMEs per month during times of high solar activity.

A typical ICME structure and its in situ signatures are presented in Figure 2.6 (for real solar wind data and geomagnetic activity during a sheath region, see Figure 5.3). The main structure of an ICME is the ejecta. About a third of ICME ejecta exhibit a clear magnetic cloud or flux rope signature, where magnetic field lines twist around the central axis. The ejecta is shown in red in the illustration, and the flux rope is indicated by the smooth rotation in the magnetic field components. When an ICME has a sufficiently high speed, i.e., exceeding the speed of information in the interplanetary space (Alfvén speed or magnetosonic speed), a shock forms in front of it. Between the shock and the leading edge of the ICME ejecta, piled-up solar wind creates the turbulent and compressed sheath region (e.g., Siscoe and Odstrcil, 2008). The sheath is shown in blue in Figure 2.6.

The shock, sheath and ejecta have different solar wind properties and distinct impact on the magnetosphere (Kilpua et al., 2017b, 2019). As presented in Figure 2.6, shocks appear as a sudden jump in the solar wind parameters. Sheath are characterised by elevated and fluctuating magnetic field and high density (and thus by high dynamic pressure). During the ejecta, the field varies more smoothly and the dynamic pressure is low.

ICME-driven sheaths are efficient drivers of geomagnetic activity (e.g., Tsurutani et al., 1988; Huttunen and Koskinen, 2004), they induce enhanced wave activity (e.g., Kilpua et al., 2013; Hietala et al., 2014), and cause significant variability in the outer radiation belt electron fluxes (e.g., Kilpua et al., 2015; Turner et al., 2019). The impact of sheaths on the wave activity of plasma waves relevant for WPI with outer belt electrons (summarised in Section 2.2.3) was comprehensively analysed in Paper I. The outer belt electron response as a function of electron energy and radial distance from the Earth focusing on the immediate, short timescale response to the sheath regions, was investigated for the first time in Paper I and Paper III. Finally, Paper II studied the dominant dynamic processes during sheaths by interpreting PSD radial profiles along with the observed wave activity.

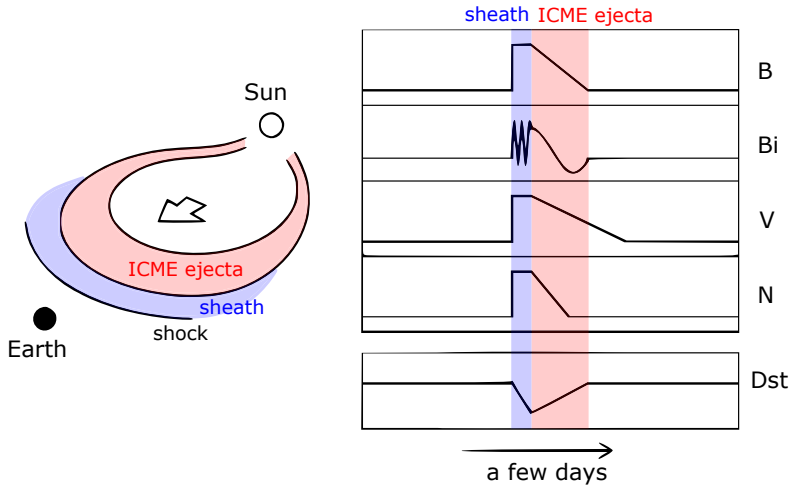

Figure 2.6: Illustration of a typical Earth-directed ICME. The simplified solar wind signatures of shocks, sheaths and ejecta, as expected to be seen in situ near the Earth, are shown in the following order: IMF magnitude, one of its components, solar wind speed and density. The last panel shows the evolution of the Dst geomagnetic activity index during a typical ICME-driven storm. This schematic shows that the sheath region is shorter than the ejecta but that is not always the case. Adapted from Kataoka and Miyoshi (2006) with permission (Copyright 2006 by the American Geophysical Union).

3 Data and methodology to investigate the radiation belts

This chapter describes the fundamental data sets and methodology that supply the basis of the research presented in this thesis. Instruments on observational missions monitoring the near-Earth space provide high-quality data sets available to the public. In particular, Section 3.1 introduces the satellite fleets surveying charged particles and plasma waves in the Earth's radiation belt environment, whose data were used in this thesis. Section 3.2 presents the employed scientific techniques to derive meaningful quantities from the data and how to analyse a set of events to form a statistical understanding of their effects. One of these calculation procedures also includes the use of computational modeling in order to gain a full picture of the system.

3.1 Instrumentation and data sets

Space data collected by satellite missions are crucial in understanding the conditions and variability in the Earth's radiation belt system. The work included in this thesis consists of multi-satellite data analyses. Observations of the solar wind conditions, plasma waves in the inner magnetosphere and particle dynamics in the radiation belts are obtained from various space-borne observatories. This section introduces the satellite instrumentation and data sources used in the publications included in this thesis. The main focus is on the Van Allen Probes and the GPS constellation, and the different aspects they cover, as these satellites are the key data providers on the outer radiation belt electrons in the research presented in this thesis. At the end of this section, also other missions and databases used for investigating wave activity and solar wind parameters are briefly discussed.

3.1.1 Van Allen Probes

NASA launched the twin Van Allen Probes in August 2012 to highly elliptical orbits to study both the inner and outer radiation belts (Mauk et al., 2013). These two spacecraft that were equipped with a multitude of advanced scientific instruments monitored the radiation belt environment with unprecedented detail until October 2019. The seven years of observations have enabled many new findings and have greatly advanced the understanding of particle dynamics in the radiation belts (Baker et al., 2013b; Reeves et al., 2013; Baker et al., 2014; Ukhorskiy et al., 2014; Breneman et al., 2015; Li et al., 2016b; Foster et al., 2017; Claudepierre et al., 2019; Zhao et al., 2019b).

The spacecraft were formerly named the Radiation Belt Storm Probes and are therefore denoted according to the corresponding acronym: RBSP-A and RBSP-B. RBSP measure the particle distributions with instrumentation in the Energetic Particle, Composition, and Thermal Plasma (ECT) instrument suite (Spence et al., 2013). RBSP can measure electrons, protons and ions. In this thesis work, the focus is on the electron fluxes that are monitored by the Magnetic Electron Ion Spectrometer (MagEIS) at energies from 30 keV to 1.5 MeV (Blake et al., 2013) and Relativistic Electron Proton Telescope (REPT) at energies from 1.8 to 10 MeV (Baker et al., 2013a). The obtained fluxes are differential and directional meaning that they are measured in finite-width energy channels and are resolved in pitch angle. Thus, they can be straightforwardly converted into PSD as will be seen later. When analysing the fluxes instead of PSD in this thesis, the omnidirectional fluxes were used which means they are averaged over the pitch angle.

Additionally, only the background corrected MagEIS data were used, where the contamination from inner belt protons and bremsstrahlung X-rays (generated via interaction of energetic electrons with the satellite itself) has been removed (Claudepierre et al., 2015). In the early phase of the RBSP mission up until September 2013, there was considerable variability in the energy scale of the MagEIS energy channels (Boyd et al., 2019). Of the sheath events studied in this thesis, 13 events occurred in this period and thus could be slightly affected by these changes.

RBSP traverse through the radiation belt system spanning $L \sim 2$–6 (from about 600 km to 20,000 km) as enabled by the elliptical orbit. The L-shell is computed from the TS04D global magnetic field model (Tsyganenko and Sitnov, 2005) and is given as part of the magnetic ephemeris data in the ECT data product, which contains also other modeled parameters that are used in PSD calculation. The orbit has a low inclination of 10° which means that RBSP stay close to the equatorial plane and can sample the nearly equatorially mirroring population. The orbital period is

about 9 hours. This means that while RBSP provide a view on different parts of the variable radiation belt particle dynamics with excellent energy resolution and pitch-angle-resolved particle data recorded with 11 s cadence, the satellite revisits the same region only after several hours. So despite the high temporal resolution along the orbit, there will be multi-hour gaps in the data at a given L-shell with the length of the gaps depending on the separation of RBSP-A and RBSP-B (see Figure 3.1a). The RBSP mission is generally advantageous for radiation belt studies, but its applicability to analysing rapid changes, such as sudden losses, can be limited due to the data gaps. Data from other missions, like the GPS constellation, can be combined with RBSP data to increase the spatial resolution (see Section 3.1.3).

The Electric and Magnetic Field Instrument Suite and Integrated Science (EMFISIS) on board RBSP measures the local electromagnetic fields and thus monitors the activity of plasma waves (Kletzing et al., 2013). It includes a fluxgate magnetometer and a search coil magnetometer, and electric fields are additionally measured by the Electric Field and Waves Suite (EFW) instrument (Wygant et al., 2013). Chorus waves and plasmaspheric hiss are recorded by the Waveform Receiver (WFR) from 2 Hz to 12 kHz and the spectra in 65 frequency bins with 6 s cadence is available in the EMFISIS data product.

EMFISIS data can be employed to derive the ULF Pc5 wave activity by applying wavelet transform on the magnetic field measurements (see Section 3.2.1). RBSP can thus monitor the local ULF Pc5 waves, but do not necessarily capture the global scale of the activity. Nevertheless, they provide observations in the heart of the outer belt where wave activity can differ from that measured from geostationary orbit (Engebretson et al., 2018; Georgiou et al., 2018).

The wave measurements can also be used to estimate the magnetospheric electron density by following the upper hybrid resonance frequency (Kurth et al., 2015). Information about the density is important for locating the plasmapause where the plasma abruptly becomes denser closer to the Earth. Chorus waves occur outside the plasmasphere, while hiss occurs inside. However, this density estimate tends to be sporadic, so in Paper I the plasmapause location for identifying chorus waves was derived from an empirical model by O'Brien and Moldwin (2003) that is dependent on the AE index and magnetic local time (MLT).

Van Allen Probes have been the gold standard of radiation belt measurements since their launch, producing high fidelity particle and wave observations. There are many results yet to discover with these data, but going forward the focus is shifting to smaller scale, lower cost successors – nanosatellites – that can be produced more affordably in higher numbers to form a satellite fleet scanning the belts. There also currently exists a group of spacecraft that yields data for radiation belt science,

while that is not their focus. Those data have recently been made public, as will be discussed next.

3.1.2 GPS constellation

The radiation belt particles are also monitored by a satellite constellation that most are familiar with in the context of navigation – the Global Positioning System (GPS). These satellites, built and operated by the Los Alamos National Laboratory, have detectors that measure electrons and protons (Carver et al., 2020). The data are recorded since year 2001 and were published in 2016.

Currently, over 20 of GPS satellites with particle detectors traverse the belts on near-circular medium-Earth orbits (altitude of $\sim 20,000$ km). They are on six different orbital planes which broadens the spatial coverage of the measurements around the Earth. This better coverage and high data density that lead to great temporal resolution at a given L-shell is the key advantage of the GPS satellites as a data source for outer belt studies. GPS can resolve rapid dynamic processes since the multi-satellite data is capable of virtually continuous measurements at a timescale of only a few tens of minutes (Morley et al., 2016). Such coverage is out of reach for the typical near-Earth space science missions consisting of one or two satellites, like the RBSP.

GPS cover the outer radiation belt with $L \sim 4$–8, extending slightly further than RBSP. The orbital inclination of 55° is relatively high. Thus GPS spend a lot of time off-equator which restricts their view on near-equatorially mirroring particles. While the orbital period is 12 hours and it takes one GPS satellite longer to revisit a given L-shell than for the RBSP, there are other GPS satellites available at that location. Therefore, the GPS can provide data at L-shells at those times RBSP are not measuring them and RBSP can also complement the GPS data with observations of the near-equatorial population.

The primary instrument for particle measurements is the Combined X-ray Dosimeter (CXD) but a few GPS satellites carry the Burst Detector Dosimeter for Block II-R. In this thesis, we use data from the former. CXD measures electrons from 120 keV to over 5 MeV with a time cadence of 4 minutes (Tuszewski et al., 2004). The instruments on board different GPS satellites are well inter-calibrated. The CXD instrument detects the particle counts and a flux forward model is needed to derive the differential omnidirectional fluxes. The model is a series of fits to theoretical representations of the flux and consists of three relativistic Maxwellian distributions and one Gaussian function (Morley et al., 2016). The fitted parameters are the number density and temperature for each of the Maxwellians and the rel-

ativistic momentum, width and normalization of the distribution for the Gaussian. The results of this 9 parameter fit are given in the GPS data product. The fit is not always available, for example due to low count rates, and at times it poorly models the actual measurements, which limit the L-range of the usable data. Filtering based on the quality of the flux forward model (Smirnov et al., 2020) especially removes data at high L-shells. Morley et al. (2016) cross-calibrated the CXD data with RBSP fluxes showing that they agree well with each other. The difference is less than a factor of 2 in the range from 140 keV to 4 MeV. That is, GPS data can be well-trusted to report the outer belt conditions at these energies.

The accuracy of the GPS data in radiation belt studies is restricted due to limitations of the instrumentation, in comparison to dedicated science missions. One downside is the requirement of the flux forward model described above as the particle detectors are not as sophisticated as on board, for example, the RBSP. An important deficiency, especially impacting the calculation of PSD, is that GPS particle measurements are not resolved in pitch angle. If such information is needed, a pitch angle distribution model must be employed which introduces some uncertainty in the data (see Section 3.2.4). Furthermore, the GPS satellites do not possess instrumentation to observe electric or magnetic fields. Acquiring information about plasma wave activity in the radiation belts must therefore rely on data from other spacecraft or ground-based observatories. The local magnetic field magnitude is also one parameter for PSD calculation and in the absence of its observation, it must be derived from a global geomagnetic field model.

In summary, despite the limitations of the instrumentation, satellites in the GPS constellation provide useful data for space science and they are an especially important resource for studies on outer radiation belt particle dynamics on short timescales. Since GPS measurements have been shown to compare well with RBSP fluxes, this satellite fleet can be confidently utilized as a key – if not the primary – radiation belt observatory in the post-RBSP era.

3.1.3 Example comparison of RBSP and GPS data

An example sheath event is presented next to illustrate how increasing the number of satellites enhances the resolution of the measurements, and to compare the RBSP and GPS data sets.

A sheath region driven by an ICME impacted the Earth's magnetosphere on 15 February 2014 and caused overall a strong depletion of ultrarelativistic electron fluxes, but there was a brief significant enhancement of the fluxes during the sheath. Figure 3.1 presents this event from the perspective of RBSP (top) and GPS (bottom)

measurements. The data are averaged into 30 minute bins in time (left) or MLT (right), and L-shell bins of size 0.1. At the time of this event, there were electron measurements available from 12 GPS satellites, in contrast to the two spacecraft RBSP mission.

Figure 3.1 demonstrates the differences in the spatial and temporal resolution of RBSP and GPS which simply arises from the fact that with more satellites, GPS can cover a larger area of the outer belt. The panels on the left show that a dozen GPS satellites can provide almost continuous data on a timescale less than an hour, whereas there are gaps of several hours between the RBSP flux measurements on a given L value. While the GPS can reach higher L-shells than RBSP, the data can become limited to a narrow L-range due to counts being below the instrument level (which can indicate electron loss) or poor quality of the flux forward model at high L-shells. Nevertheless, in the covered range GPS data fill in the gaps in RBSP observations and can resolve much more precisely the timescale of the enhancement and depletion.

The panels on the right in Figure 3.1 show how during this event, where data is shown for 2 days, GPS satellites have collected data from all MLT. RBSP observations, on the other hand, are restricted to the day side since the perigee of the elliptical orbits is near local midnight during this event. Thus, the GPS constellation gives a more global picture of the radiation belt electron dynamics.

3.1.4 Other satellite missions and data sources

In this thesis, key data sets come from RBSP and GPS, as described above, but several additional data sets for inner magnetospheric wave activity and the solar wind context are used from various other satellites.

Solar wind conditions, including IMF magnitude, solar wind speed and dynamic pressure were obtained from the Magnetic Fields Investigation (Lepping et al., 1995) and Solar Wind Experiment (Ogilvie et al., 1995) instruments on the Wind spacecraft which, during the time of the studies, was located at the Lagrangian L1 point, $1.5 \cdot 10^6$ km Sun-ward from Earth. Since the focus of the analyses presented in this thesis is on what occurs in the magnetosphere, the Wind data were propagated from L1 to the bow shock nose. That is, the data were shifted in time by estimating the required time shift from the mean solar wind speed.

Information on the level of magnetospheric disturbances caused by the studied events in the form of the geomagnetic activity indices SYM-H and AL was acquired from ground-based observatories whose data are available in NASA's OMNI

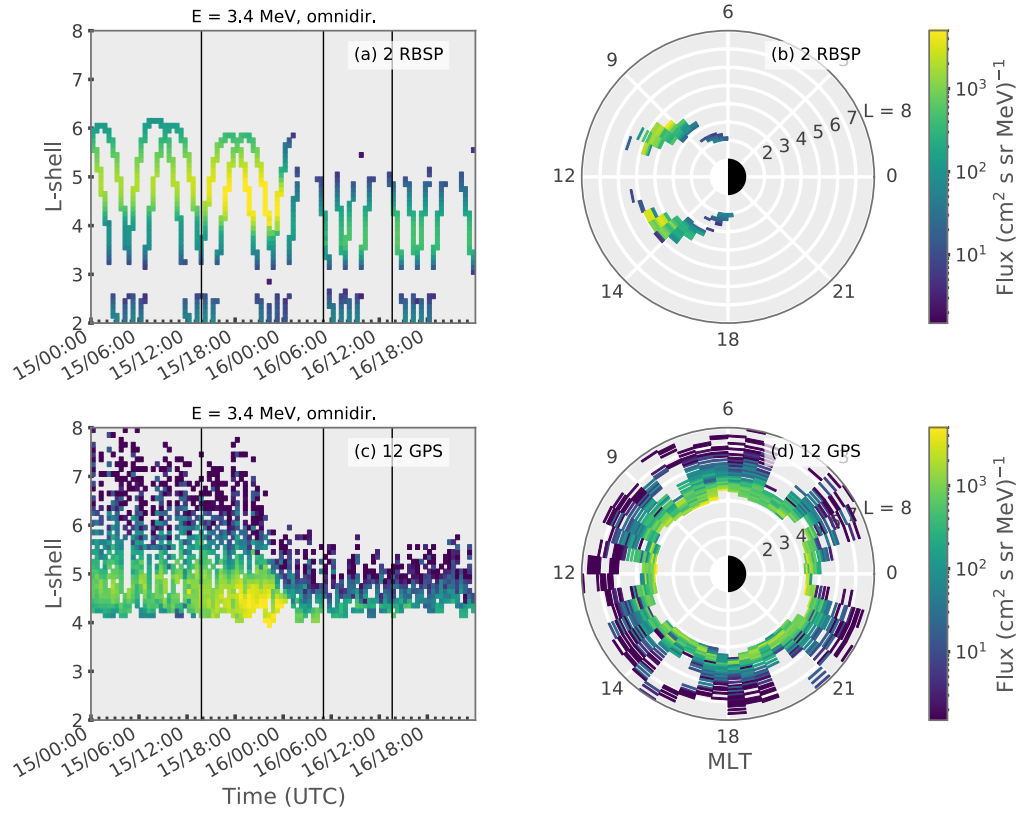

Figure 3.1: Comparison of electron fluxes at energy 3.4 MeV from (a–b) 2 RBSP and (c–d) 12 GPS satellites during a sheath event on 15 February 2014. Panels (a, c) show the fluxes as a function of L-shell and time, while panels (b, d) as a function of L-shell and magnetic local time (MLT). The data are binned 0.1 in L-shell and 30 minutes in time or MLT. In panels (a, c) the black vertical lines indicate the times for the shock, ejecta leading edge and ejecta trailing edge. The sheath region is between the shock front and ejecta (first two lines). This figure illustrates the differences in resolution of RBSP and GPS data due to the different number of satellites.

database[1]. Both of these are 1-minute indices.

Measurements of ULF Pc5 and EMIC waves were obtained from Geostationary Operational Environmental Satellites (GOES). The circular geostationary orbit is at an altitude of about 40,000 km ($L \sim 6.6$). Wave activity was derived from the fluxgate magnetometer measurements which sample the magnetic field at a time cadence of 0.512 s (Singer et al., 1996). This was done by wavelet analysis, and the methodology is presented in Section 3.2.1. With this time resolution, GOES satellites can resolve waves with frequencies up to 1 Hz which restricts the upper limit of the observed EMIC waves (with frequency range of 0.1–5 Hz). Wave measurements at geostationary orbit capture the typically global nature of ULF waves, but there might also be local enhancements in wave activity in the radiation belts that GOES cannot observe (Engebretson et al., 2018; Georgiou et al., 2018). A more complete picture can be achieved by complementing the GOES wave data with local measurements by RBSP.

As described in Section 3.1.1, RBSP measure chorus waves, but since chorus are generally observed on the dawn side (e.g., Lam et al., 2010), the activity of these waves can be missed by RBSP if the perigee of the orbits is near dawn. In such cases in the work presented in this thesis, electron precipitation recorded by the Polar Operational Environmental Satellites (POES) has been used as a proxy for chorus waves as formulated by Chen et al. (2014b). This is justified as both the generation of chorus waves and the subsequent wave-particle interactions effectively scatter low-energy (30–100 keV) electrons into the atmosphere. To measure the precipitation, the POES spacecraft orbit the Earth at low altitudes of about 800 km on polar orbits that pass near the poles. Data from the Medium Energy Proton and Electron Detector (MEPED) on the Space Environment Monitor instrument suite (Evans and Greer, 2004) on board six POES satellites have been used to compute the proxy. MEPED has two telescope which measure the precipitating and trapped fluxes respectively, but at high latitudes the observed populations are mixed due to the loss cone width (Rodger et al., 2010, 2013). Thus, to better estimate the precipitating fluxes for the chorus proxy, data from the two telescopes were merged by computing the geometric mean (e.g., Rodger et al., 2013). MEPED data are contaminated by protons and therefore the reprocessed data were employed in the analysis presented in this thesis (Asikainen and Mursula, 2013; Asikainen, 2017).

[1]Available through NASA's Coordinated Data Analysis Web interface: `https://cdaweb.gsfc.nasa.gov/index.html`

3.2 Methods

More information on the radiation belt dynamics can be revealed by deriving new physical quantities from the satellite data, sometimes with the help of models when observations are lacking the larger scale picture. Furthermore, statistical studies combining data from multiple events shed light on the general radiation belt response. This section explains the analysis methods applied in the publications presented in this thesis. It goes through the procedures of how to obtain the strength of wave activity in different frequency ranges from magnetic field measurements, how to discover the typical trends in solar wind conditions and magnetospheric responses during sheath regions of varying widths, how to quantify the overall response of outer radiation belt electrons to sheath region impact and how to calculate phase space density. Phase space density is a powerful tool for investigating the electron dynamics in the outer belt, and its computation requires knowledge of the global geomagnetic field only available from modeling. The application of the technique is discussed both for RBSP and GPS data, the latter of which requires additional modeling due to restrictions in the measurements.

3.2.1 Wavelet analysis

Plasma waves cause periodic fluctuations in the electric and magnetic fields measured by satellite instrumentation. The recorded data must be processed in order to find out how much wave power is present at each frequency as a function of time. In this thesis, the focus is on the ULF Pc5 and EMIC waves which are identified from magnetometer measurements.

Wavelet analysis is performed by transforming the time series into time-frequency space with the help of a wavelet function (Torrence and Compo, 1998). This methodology allows for obtaining information about both the dominant wave modes and the temporal evolution of the intensity of the waves. Here the continuous wavelet transform applying the Morlet wavelet (Morlet et al., 1982) was used. Continuous transform with a complex wavelet function (e.g., Morlet) is best suited for capturing oscillations from time series data. In short, the analysed time series is convolved with the wavelet for a selected set of wavelet scales which are not equal to but are related to the Fourier period (i.e., the periods of the wave modes). For the Morlet wavelet, the wavelet scale is very close to the Fourier period (Torrence and Compo, 1998). The smallest scale is chosen to be two times the time step of the data in the time series, as that dictates the highest frequency of fluctuations that can be inferred from the data. For example, the time resolution of the GOES magnetome-

ter measurements is about 0.5 s, i.e., two measurements per second, meaning that only fluctuations that occur up to once per second can be resolved. The largest scale depends on the length of the time series. Since the analysed data are not cyclic, some edge effects arise near the start and end of the time series. The region where edge effects are important is called the cone of influence (COI) and its width depends on the scale.

The methodology is illustrated in Figure 3.2 using GOES magnetometer data. The analysis was performed on the magnetic field magnitude using an implementation[2] of the methodology presented in Torrence and Compo (1998). The data were linearly interpolated to ensure that the time step was the same between all data points which is a requirement for the wavelet transform. The key data set returned by the wavelet analysis is the wavelet power spectrum (Figure 3.2b). It shows how wave power is distributed at different frequencies during the event. To convert the data back to a time series for further analysis and to study different wave modes, the next step is to calculate the mean wave power in a given frequency range. The averaging was done in 5 minute bins. In panel b, the ranges for ULF Pc5 and EMIC waves are shown and the mean power is shown in panel c. One can clearly see how the wave power increases from the preceding solar wind to the sheath region.

3.2.2 Superposed epoch analysis

Statistical studies of multiple events enable gaining understanding of the typical parameters associated with sheath regions and their impact on the radiation belt system. Sheath events studied in this thesis occurred during the years 2012–2018 and their duration varied significantly from just 3 h to almost a full day. To study the overall trend in quantities during sheaths, the approximately same physical domains during the sheath regions should be compared to each other. The data must therefore be arranged in a way that the statistical analysis can be performed.

Superposed epoch analysis has previously been used for similar purposes (e.g., O'Brien et al., 2001; Kataoka and Miyoshi, 2006; Turner et al., 2019). A zero epoch time[3] is chosen corresponding to some characteristic of the event and it acts as a reference to align the data from all studied events according to which the data are then superposed. For sheath events, the natural choice is the timing of the easily identified shock where the sheath region begins.

Because of the large variation of the sheath durations, an additional epoch time

[2] `https://github.com/aaren/wavelets`

[3] The results are typically presented as a function of hours or days counted from the zero epoch time so this timing is indicated by zero – hence its name.

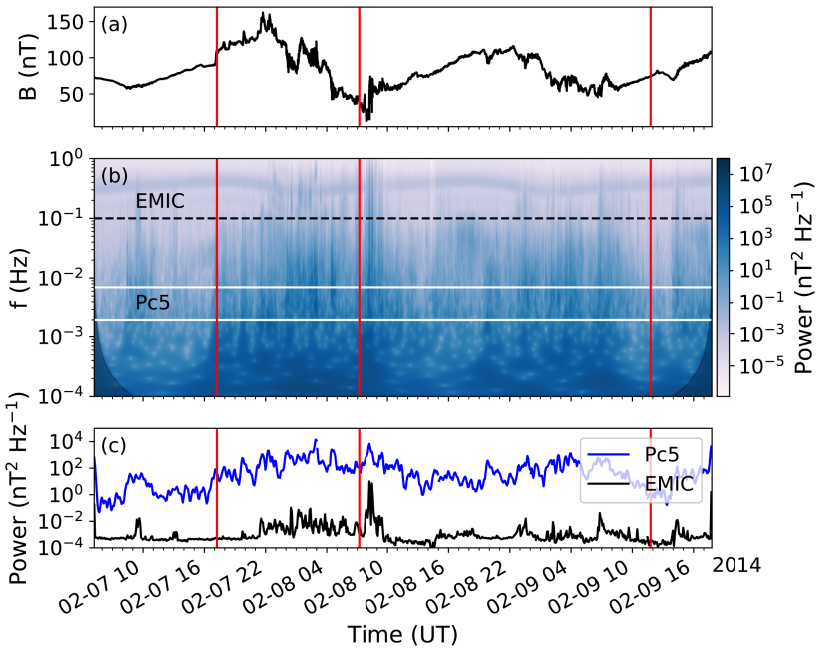

Figure 3.2: (a) Magnetic field magnitude measured at geostationary orbit by GOES-15 during a sheath event. (b) Wavelet power spectrum showing the wave power as a function of frequency and time. The frequency range of ULF Pc5 waves is shown with white lines, and the lowest frequency of the EMIC waves is shown as the black dashed line. The shaded areas near the bottom left and right corners indicate the COI. (c) Wave power of ULF Pc5 and EMIC waves, derived by averaging the power spectrum in the respective frequency ranges. The red vertical lines indicate the sheath and ejecta timings. Adapted from Paper I.

was chosen at a later time, in this case, at the ejecta leading edge where the sheath region ends. Without this second reference time, the trend only near the start of the sheath could be determined as the ejecta starting at different times during different events would begin to interfere with the statistical results. In order to focus on the sheath and prevent contributions from the ejecta, the data were aligned to both reference times simultaneously. To accomplish this, all studied sheaths were normalized to the same duration. This was chosen to be the mean duration of the sheath regions of all events, which was 12.0 h.

The two reference times version of the technique is called double superposed epoch analysis and it has been used in previous statistical studies of the typical properties of solar wind structures, especially for sheath regions (e.g., Kilpua et al., 2015, 2019; Masías-Meza et al., 2016). This technique was employed in Paper I to study the solar wind parameters during sheaths and the geomagnetic activity, wave power and overall trends in electron fluxes in the heart of the outer radiation belt caused by the sheaths.

The double superposed epoch analysis is illustrated in Figure 3.3. The implementation of the method was that for each event, the sheath was rescaled to start at time zero and end 12 hours after that. The data during the sheath was then linearly interpolated so that all events shared the same time step. Sheaths that were longer than 12 h were compressed meaning that some information was lost and sheaths shorter than 12 h were stretched and most affected by the interpolation. However, the resampling of the data during sheaths did not significantly affect the results which was tested by considering a subset of events with a smaller range of sheath durations. Electron flux and wave power data can change by orders of magnitude during the events, so interpolation was performed on the logarithm of those data. The statistical trends were found by superposing the data according to the reference times and computing the mean at each time step. Other statistical properties can also be computed, such as the lower and upper quartiles which present the level where a quarter of the data is below or above that level, respectively. They show the range of variability in the data.

3.2.3 Response parameter

The method of superposed epoch analysis discussed previously indicate the overall trends in parameters, like the electron fluxes and wave power, during sheaths. Some of the variations can be averaged out when calculating the mean from a set of events as sheaths can cause both loss and enhancement of the flux. To look in more detail at which L-shells and energies electron fluxes tend to increase or decrease in response

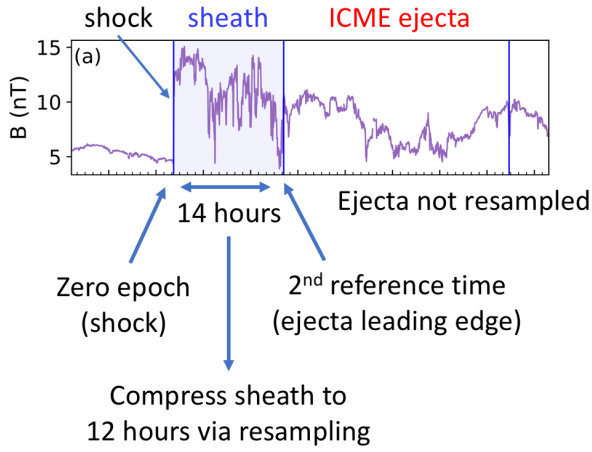

Figure 3.3: Illustration of the superposed epoch analysis method with two reference times: one at the shock where the sheath starts and the other at the ejecta leading edge where the sheath ends. Data during the sheath is either compressed (shown here) or stretched via resampling to the common duration of 12 h.

to the impact of sheath regions, the fluxes before and after the sheath were compared with each other. The response parameter was calculated as the ratio of these pre- and post-sheath fluxes.

Such analysis has been performed for example by Reeves et al. (2003) who studied the response of relativistic electrons at geostationary orbit to geomagnetic storms in general. They compared the maximum flux over several days before and after the storm, excluding the day of the storm, to see if storms caused overall enhancements or losses. Similar work on storm response was carried out by Turner et al. (2015) who studied also the energy and L-shell dependence of the response. They calculated the response parameter as the ratio of post-storm to pre-storm maximum flux which were found in a 72-hour window after and before 12 hours from the storm main phase. Turner et al. (2019) investigated the response of outer belt electron fluxes to different storm drivers, including sheath events, and the response parameter was defined as in Turner et al. (2015).

This thesis presents a similar response parameter analysis as Turner et al. (2019) to investigate the response of the outer belt electrons to sheath regions. However, instead of studying the response over relatively long periods (72 h, excluding the day of the storm) which can miss the short timescale variation caused by specific solar

wind driver structures, the analysis presented in Paper I and Paper III focused on the more immediate response caused solely by the sheath regions, calculating the response parameter using data just before and after the sheath. These works also did not limit the study to the storm periods. This approach mostly excludes possible contributions from the preceding or trailing solar wind structures, such as the ICME ejecta, in particular with the high data density GPS measurements.

In Paper I, the response parameter was calculated using RBSP data whose resolution permitted for 6 hours as the shortest timescale with sufficient L-shell coverage. Since the timescale is significantly briefer than in previous response studies, the pre-sheath and post-sheath fluxes were taken as the average instead of the maximum flux. The response parameter was thus defined as

$$R = \frac{< j_{post-sheath} >}{< j_{pre-sheath} >}, \tag{3.1}$$

where the brackets indicate the average over 6 hours. This response parameter was calculated in 0.1 sized L-shell bins at different energies for the omnidirectional fluxes. The calculation is illustrated in Figure 3.4. The value of R indicates the level of change in the fluxes but here the focus is on the overall response instead of the strength of the response. Therefore, following previous studies (Reeves et al., 2003; Turner et al., 2015, 2019), the outer belt electron response is categorized as follows. If fluxes increased by over a factor of 2 ($R > 2$), the response is *enhancement*. If fluxes decreased by over a factor of 2 ($R < 0.5$), the response is *depletion*. Finally, if fluxes did not change significantly ($0.5 \leq R \leq 2$) the response is termed *no change*.

It is noted that the 6-hour average after the sheath region is during in the impact of the ejecta. While it is expected that major variation caused by the ejecta manifests over a longer timescale as the mean ejecta duration in the events considered in this thesis is 28.4 h, fluctuations during the early ejecta could affect the response analysis results. This is an additional argument for using the flux average instead of the flux maximum since the latter is more prone to being influenced by the ejecta. An even shorter time period for the flux averaging for the response parameter calculation would offer further confidence in the response being due to the sheath only, but this is not feasible with RBSP data.

In Paper III, response calculations used data from GPS satellites. The GPS constellation provides broader coverage of the outer belt than RBSP (see Section 3.1.3), so the data enable consideration of shorter timescales while retaining sufficient L-shell coverage for the analysis. With GPS data, the response parameter could be computed from 30-minute averages before and after the sheath, confirming the immediate outer belt electron response to the sheath.

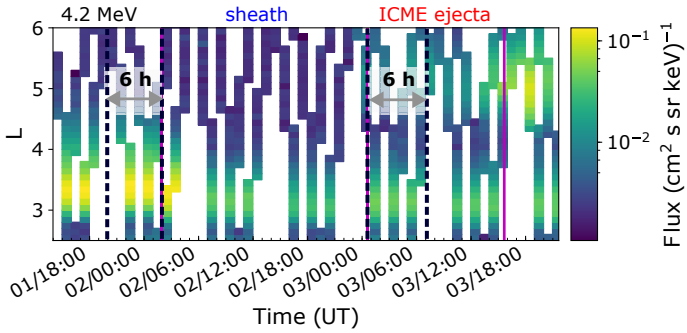

Figure 3.4: Illustration of the calculation of the response parameter from outer radiation belt electron fluxes. The plotted RBSP flux has been binned 0.1 in L-shell and 1 h in time. To calculate the response parameter, flux is averaged before and after the sheath (between the black dashed lines), and those averaged fluxes are compared to each other to determine the response (enhancement, depletion or no significant change). The response is calculated separately for each L-shell.

While the discussion here on the application of the response parameter focused on the variation of outer belt electron fluxes, the same methodology can be applied to other quantities as well. Paper III included analysis of the response of electron PSD in the outer belt which sheds more light on the processes that cause the observed flux enhancement and losses, as will be described in the next section.

Finally, it is noted that the response parameter approach ignores the details of the electron flux variation during the sheath region, namely how fast the changes occur. For example, there can be a brief enhancement during the sheath although the overall response captured by the response parameter would be depletion (as shown in a case study in Paper II). Further studies must be performed to investigate the timescale and magnitude of changes during sheaths.

3.2.4 Phase space density calculation from RBSP and GPS data

Electron flux can change purely through adiabatic processes that are reversible (e.g., the Dst effect mentioned in Section 2.2.4). The key interest however is typically on irreversible processes that energize electrons or cause them to be lost from the system entirely. Phase space density (PSD) presented in the phase space coordinate system is an important quantity for investigating these processes that violate the adiabatic invariants (Kim and Chan, 1997). A careful analysis of the shape and evolution of PSD radial profiles, especially when information on wave activity is also available,

sheds light on the likely wave-particle interactions and other processes that cause acceleration, transport or loss, for example, as shown in Paper II.

The general procedure in deriving PSD from satellite measurements combined with global geomagnetic field modeling has been introduced in Section 2.2.2, and the current section presents more details in applying the calculation steps to RBSP and GPS data. The implementations are different for the two missions due to the different instrumentation on board these spacecraft. GPS satellites lack magnetometers and pitch angle resolved particle measurements, so in contrast to RBSP, calculation of PSD from GPS data needs to rely more on modeling. The PSD calculation and analysis codes employed in Paper II and Paper III were created by the author of this thesis.

PSD from RBSP data

Particle instruments on board RBSP measure the pitch angle resolved differential electron fluxes with pitch angle bins of size 16.4° and 10.6° for MagEIS and REPT, respectively. The EMFISIS suite provides local magnetic field measurements which were used to compute μ (Equation 2.1). The magnetic ephemeris data include K and L^* calculated from the TS04 global geomagnetic field model (Tsyganenko and Sitnov, 2005) so they are readily applicable to PSD calculation. K and L^* have 5° resolution in (equatorial) pitch angle and typically 5 min resolution in time.

PSD calculation in this thesis used MagEIS measurements for electrons in the keV energy range and REPT measurements in the MeV range. The available data cover energies from 30 keV to 10 MeV. The fluxes were binned to 1 min time resolution which allowed for smoother PSD profiles than binning to the time resolution of the TS04 model results. The energy resolution of the data was also improved. For example, the REPT instrument has 12 energy channels of which the lowest 9 were used. The channels are not distributed evenly in energy and their widths vary. The array of channels has gaps in energy where electrons are not strictly monitored by the instrument.[4] Two artificial energy channels, inserted in between the instrumental channels and covering the gaps in energy, supply additional data points which improves the resolution of the computed PSD. The flux values in these artificial channels were obtained by interpolating the measured flux from the adjacent real energy channels (in log-log space for flux and energy), but only if there were measurements available in both real channels on the considered time step. This raised the number of used energy channels from 9 to 25 for REPT and from 16 to 46 for MagEIS.

[4]However, the given lower and upper limits of the instrumental energy channels are not exact and electrons with energies below and above a channel's limits can be measured by that channel.

While the central energy is given for the real instrumental channels, this energy was calculated as the geometric mean of the channel limits for the artificial channels based on Chen et al. (2005). Following Chen et al. (2005), the relativistic momentum was computed for each energy channel (true or artificial) as the arithmetic mean of the channel limits (E^{ch}_{min} and E^{ch}_{max}):

$$\langle p^2c^2\rangle_{ch} = \frac{1}{2}\big[E^{ch}_{min}(E^{ch}_{min} + 2m_0c^2) + E^{ch}_{max}(E^{ch}_{max} + 2m_0c^2)\big]. \tag{3.2}$$

Along with the differential electron flux, this relativistic momentum can be inserted into Equation 2.7 to derive PSD. Including a conversion factor accounting for the nominal units (Hilmer et al., 2000; Chen et al., 2005), the equation for PSD becomes

$$f_{ch} = 3.32 \cdot 10^{-11} \frac{j_{ch}}{\langle p^2c^2\rangle_{ch}}, \tag{3.3}$$

where momentum is given in units $(\mathrm{MeV})^2$ and flux in units $(\mathrm{cm}^2\ \mathrm{s\ sr\ MeV})^{-1}$, and the resulting PSD is obtained in units $(\mathrm{c/MeV/cm})^3$ where c is the speed of light. However, as stated earlier, PSD from Equation 3.3 is not yet in the desired phase space coordinates.

The procedure for acquiring proper values of PSD follows the steps outlined in Section 2.2.2. Instead of setting a single value for μ and K, PSD from RBSP data was computed for μ and K constrained by a fixed range. The ranges permit better resolution as more data points can be acquired. Especially the magnetic ephemeris data do not have sufficient resolution in K to limit PSD to one K value. The ranges must be carefully chosen to allow for adequate resolution of PSD as a function of L^* but to avoid significant fluctuations from too many data points at different energies and pitch angles. Calculating RBSP PSD at single values of μ and K requires fitting to energy and pitch angle distributions (e.g., Morley et al., 2013; Boyd et al., 2014). In the calculation of RBSP PSD used in the work presented in this thesis, no fitting was performed.

The RBSP observe the local pitch angles which were then mapped to equatorial pitch angles based on conservation of the first adiabatic invariant (Equation 2.2), utilizing the modeled equatorial magnetic field magnitude. Modeled K and L^* were interpolated to these equatorial pitch angles. The relativistic momentum from Equation 3.2 and the locally measured magnetic field magnitude were used to compute μ and thus the calculation used the local pitch angles. Since μ is an adiabatic invariant, the local value corresponds to the equatorial one. At this point, the RBSP flux data as a function of energy, pitch angle and location has been converted to PSD

(Equation 3.3) and associated with the corresponding adiabatic invariants at each time step.

Finally, the desired PSD was obtained by picking the values where μ and K correspond to the chosen ranges. The obtained PSD has fluctuations due to the employed μ and K ranges which contribute to the uncertainty. Broad enough ranges are however required for sufficient resolution. The fluctuations arise from finding PSD points within the μ and K ranges from two or more energy channels or pitch angle bins on a single time step. These PSD values can be different but correspond to similar L^* and thus show up at the same place in the profile. REPT energy channels, in particular, may have order of magnitude jumps in adjacent channels contributing to the fluctuation. Such effects have been seen in other studies with similar methodology (e.g., Schiller et al., 2014). For smoother radial profiles that are easier to interpret, RBSP PSD was averaged into 0.15 L^* bins in the radial profiles presented in this thesis.

PSD from GPS data

In contrast to RBSP, calculating PSD from GPS data requires running the geomagnetic field model, using it for deriving all adiabatic invariants, and employing a pitch angle distribution model. Data from all available CXD-equipped GPS satellites were used, with the exception of satellite ns60 which has unreliable counts-to-flux fits due to intermittent noise. PSD was calculated separately for each GPS satellite, and then all PSD were combined via binning.

The calculation of GPS PSD closely follows the steps described in Section 2.2.2. Due to the use of modeling and fitting, single values for μ and K can be set. As part of the work included in this thesis, the TS04 model was run for all satellites for the investigated time intervals. This utilized the LANLGeoMag code library (Henderson et al., 2018) which takes the satellite position as input. The model yields equatorial pitch angles corresponding to the selected K, the corresponding L^* values, and the local and equatorial magnetic field strengths used for μ calculation and pitch angle conversions.

The electron energy corresponding to the chosen μ at each time step was solved from Equation 2.1 with the relativistic momentum given by Equation 2.8. The flux forward model converted the CXD electron measurements to omnidirectional flux at these energies, restricted from 140 keV to 4 MeV where data is reliable (Morley et al., 2016). The applied goodness of fit filtering compares modeled counts to the measured counts and discards the data when the discrepancy is too high (Smirnov et al., 2020). It is noted that the method is biased to exclude also low fluxes in

addition to poor fits, which leads to removal of data at high L-shells.

The next important step was the derivation of directional fluxes from the omnidirectional measurements. The angular distribution of flux was derived with the empirical relativistic electron pitch angle distribution (REPAD) model by Chen et al. (2014a). REPAD can describe various shapes of the pitch angle distribution. Its inputs are electron energy, satellite location (L-shell and MLT), and the AE geomagnetic activity index. The directional flux as a function of electron energy and equatorial pitch angle is

$$j(E, \alpha_{eq}) = N(E)\hat{j}(E, \alpha_{eq}), \tag{3.4}$$

where N is a normalization factor and $\hat{j}$ is the model output. The model was normalized by the measured omnidirectional flux which can be expressed as

$$\begin{aligned} J(E) &= \frac{1}{4\pi}\int\int j(E,\alpha)d\Omega = \int_0^{\pi/2} j(E,\alpha)\sin(\alpha)d\alpha \\ &= N(E)\int_0^{\pi/2} \hat{j}(E,\alpha_{eq})\sin(\alpha)d\alpha \end{aligned} \tag{3.5}$$

where the integral over the full solid angle has been simplified by assuming that the fluxes are gyrotropic and symmetrical in pitch angle. Equation 3.4 has been substituted in the last step. It is pertinent to note that REPAD models the equatorial pitch angle distribution but the measured omnidirectional fluxes are local. In order to solve for the normalization, a change of variables was performed according to Hess (1968, p.65) and Equation 3.5 becomes

$$J(E) = N(E)\frac{B}{2B_{eq}}\int_0^{\alpha_{90}} \hat{j}(E,\alpha_{eq})\frac{\sin(2\alpha_{eq})}{\sqrt{1-\frac{B}{B_{eq}}\sin^2(\alpha_{eq})}}d\alpha_{eq}, \tag{3.6}$$

where B/B_{eq} is the ratio of local to equatorial magnetic field magnitudes and the equatorial pitch angle corresponding to local 90° pitch angle is given by (based on conservation of μ; Equation 2.2)

$$\alpha_{90} = \arcsin\left(\sqrt{\frac{B_{eq}}{B}}\right). \tag{3.7}$$

When GPS satellites are at high latitudes during their orbit, the range of observable equatorial pitch angles becomes restricted. Since the modeled equatorial pitch angle distribution was normalized by local measurements, the modeled directional

flux at near-equatorially mirroring pitch angles not seen by GPS can be considered an extrapolation which contributes to uncertainty in PSD. The level of uncertainty was reduced by considering how much of the full equatorial pitch angle distribution was observable by GPS, i.e., only directional fluxes where the following ratio was small enough were used:

$$\frac{I_{GPS}}{I_{tot}} = \frac{\int_0^{\alpha_{90}} f(E, \alpha_{eq}) \sin(\alpha_{eq}) d\alpha_{eq}}{\int_0^{\pi/2} f(E, \alpha_{eq}) \sin(\alpha_{eq}) d\alpha_{eq}} < 0.1. \tag{3.8}$$

The integral I_{GPS} represents the fraction of the distribution observed by GPS which is compared to the full distribution represented by I_{tot}. In principle, the modeled pitch angle distribution could be cross-calibrated against pitch angle resolved measurements, for example, from RBSP during conjunctions. However, as a benefit of the GPS data set is its continued availability after the end of the RBSP mission, it is therefore better not to rely on RBSP observations in calculation of GPS PSD.

Finally, after deriving the directional fluxes for the selected μ and K, PSD was simply obtained from Equation 2.7. As with the flux forward model goodness of fit filtering, the filtering of the REPAD model tends to remove data at high L^*. The resultant GPS PSD is thus limited in the range of L^* it covers. However, the temporal resolution is greater than for PSD computed from RBSP data, owing to the higher data density provided by the GPS constellation, which is especially illustrated in Paper III.

4 Wave activity and electron flux variability in the outer radiation belt driven by sheaths

Turbulent and high-pressure sheath regions driven by ICMEs compress the magnetopause and induce plasma waves in the inner magnetosphere which, in turn, affect the electrons in the Earth's radiation belts. The work presented in this thesis comprises a comprehensive analysis of the variations in the geospace in response to ICME-driven sheaths. This chapter discusses how the studied sheath events were selected, their typical features in the solar wind, geomagnetic activity during sheaths and the wave activity associated with the sheath impact. The results are compared and contrasted to the level of activity before the event and during the following ejecta. This chapter also details the changes in the outer radiation belt electron fluxes on different timescales as observed by the RBSP and GPS spacecraft. The results presented here are published in Paper I and Paper III.

4.1 Event selection

The work presented in this thesis focuses on sheaths that impacted the Earth during 2012 to 2018. This time period was chosen as the RBSP spacecraft were measuring the radiation belts during that time, providing high quality data on the radiation belt particle fluxes and local wave activity in the heart of the outer belt.

During these six years, 37 sheath events were identified from solar wind observations based on the nominal characteristics of sheaths (see Section 2.3.2). The selection of events was based on the sheath lists compiled by Palmerio et al. (2016) and Kilpua et al. (2019) for the periods 2012–2015 and 2016–2018, respectively, but three additional sheath events in 2016 were also included. The starting point of the sheath event identification were ICME catalogs that list the arrival and end times of ICMEs that have hit the Earth. For example, Richardson and Cane (2010) pro-

vide such a list of ICMEs.[1] The start time of the sheath region was taken as the time of the shock arrival as reported in the University of Helsinki Heliospheric Shock Database.[2] The shock is identified from solar wind data in the OMNI database which is recorded by spacecraft at the L1 point. Additionally, Wind data was visually inspected to adjust the timing of the ICME ejecta leading edge (i.e., the end time of the sheath region) and the ejecta trailing edge. These timings were shifted by the time it took on average for solar wind to propagate from L1 to the bow shock nose.

In contrast to previous studies analysing the impact of ICMEs and sheaths on the radiation belts, the work presented in this thesis did not impose any constrains on the events, other than that the sheath and ejecta boundaries were relatively well-defined. This means that the selected 37 sheath events include nongeoeffective sheaths in addition to sheaths that caused significant geomagnetic activity. Geoeffectiveness was defined so that for geoeffective events, the SYM-H index reached a minimum below -30 nT during the sheath or 2 hours after it (the extension takes into account lag in the ring current response). The geoeffectiveness of the ejecta was not considered. For nongeoeffective sheaths, the SYM-H index did not drop below -30 nT. There were 17 geoeffective and 20 nongeoeffective sheaths. This SYM-H limit was specifically chosen to include also weak geomagnetic storms in the geoeffective events instead of just moderate or strong storms (SYM-H minimum below -50 nT or -100 nT as categorized in Gonzalez et al., 1994) in order to have comparable subsets for the statistical analysis.

The durations of the sheath regions and the ejecta also vary widely. Sheaths lasted 3.0–22.7 hours (standard deviation of 5.3 h) and ejecta lasted 5.8–55.1 hours (standard deviation of 11.1 h). The mean duration of the investigated sheaths is 12.0 hours and for the ejecta it is 28.4 hours. The mean sheath duration was used to scale all sheaths to a similar length in order to perform statistical analysis.

4.2 Properties of sheaths and the associated inner magnetospheric wave activity

The turbulent sheath regions preceding ICMEs were introduced in Section 2.3.2. They are regions with large dynamic pressure and a high level of fluctuations in the magnetic field. These telltale signatures are clearly seen in the superposed epoch analysis results presented in Figure 4.1. The median of the data form all studied

[1] The Richardson and Cane ICME catalog is available at `https://izw1.caltech.edu/ACE/ASC/DATA/level3/icmetable2.htm`

[2] The Heliospheric Shock Database is available at `http://www.ipshocks.fi`

37 sheath events is shown with the black line, and the sheath region interval is indicated by the dashed vertical lines. The statistical analysis method was described in Section 3.2.2.

The shock is readily identifiable as a large and simultaneous jump in the IMF magnitude, solar wind speed and dynamic pressure measured in situ near the Earth. The IMF magnitude, solar wind speed and dynamic pressure stay all enhanced throughout the sheath. The IMF magnitude increases again at the ejecta leading edge, while the dynamic pressure (panel c in Figure 4.1) quickly drops in the following ejecta which illustrates that the sheath consists of compressed piled-up plasma in front of the ejecta. The pressure pulses associated with sheaths compress the day side magnetosphere significantly as shown by the day side magnetopause location estimated from the Shue et al. (1998) model in panel f. Sometimes the magnetopause is pushed briefly beyond the geostationary orbit at 6.6 R_E. Examples of such cases are sheath events studied in Paper II and Lugaz et al. (2016). This provides prime conditions for electron loss in the outer radiation belt via magnetopause shadowing (see Section 2.2.4). The superposed epoch analysis in Paper I was repeated for sheaths divided by geoeffectiveness, which showed that geoeffective sheaths have stronger pressure pulses and thus push the magnetopause further inward.

Along with the ICME ejecta, sheaths are important drivers of geomagnetic disturbances, but in the data set studied in this thesis, the ejecta caused a stronger response as shown by the SYM-H index in panel d. Substorm activity shown by the AL index (panel e) is, on average, similar between the sheath and ejecta with stronger activity during the ejecta in the lower quartile. Figure 4.1 shows the results of the superposed epoch analysis for all the studied sheaths, which have large variation in their geomagnetic impact. Geoeffective sheaths are associated with even more geoeffective ejecta, and also substorm activity is larger during both the sheath and ejecta during geoeffective events. Nongeoeffective sheaths are associated with weaker substorm activity. Therefore, geoeffective sheaths drive more substorm injections which replenish the belts with lower energy electrons and excite chorus waves.

During geomagnetic activity the magnetosphere is abundant with waves, which interact with radiation belt particles. Intense wave activity can also be generated during geomagnetically quieter times when the system is however otherwise disturbed, for example, by the impact of a sheath carrying northward magnetic field. In fact, sheaths are excellent drivers of wave activity regardless of their geomagnetic impact, as has been shown in Paper I.

Panels g–i in Figure 4.1 show how activity of chorus, ULF Pc5 and EMIC waves increases during the sheaths in contrast to the level of wave activity before the event. Chorus wave activity remains elevated during the ejecta due to the continued

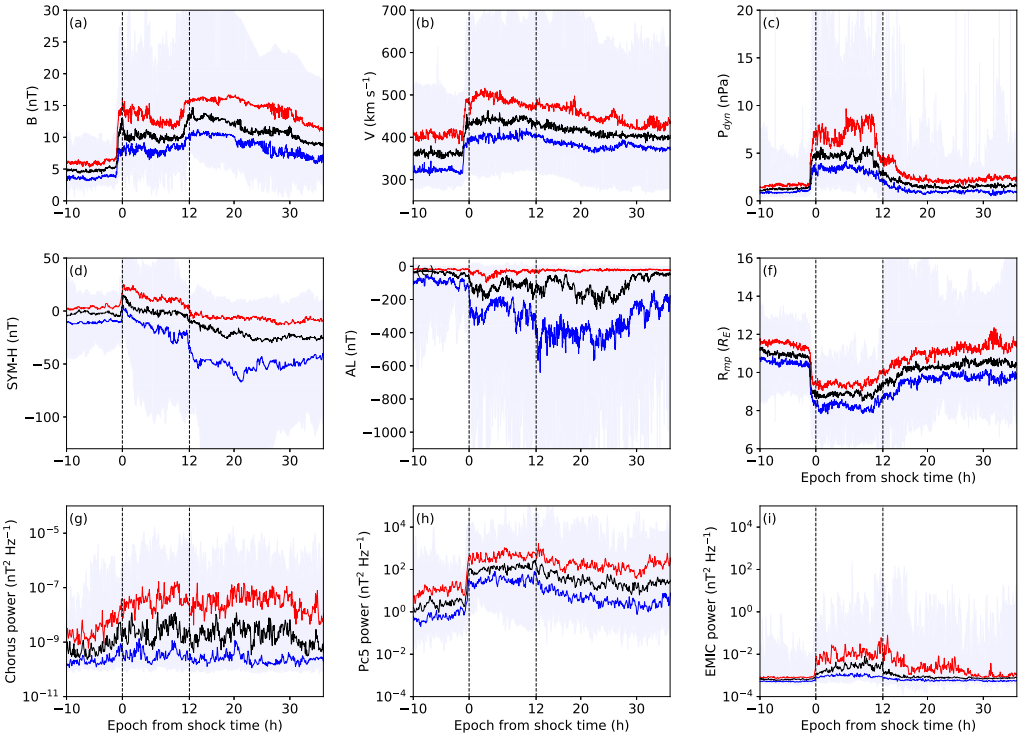

Figure 4.1: Results of superposed epoch analysis for solar wind properties (Wind data), geomagnetic activity (OMNI data) and wave activity (RBSP and GOES data) for 37 sheath events. The panels show (a) IMF magnitude, (b) solar wind speed, (c) solar wind dynamic pressure, (d) SYM-H index, (e) AL index, (f) modeled subsolar magnetopause location (Shue et al., 1998), and the wave power of (g) chorus waves from RBSP and (h) ULF Pc5 and (i) EMIC waves from GOES-15. Red, black and blue lines show the upper quartile (75% of data), median (50% of data) and lower quartile (25% of data), respectively. The extrema of all data are shaded in light blue. The dashed vertical lines indicate the sheath region between the two reference epoch times. Adapted from Paper I.

substorm activity, but the power of ULF waves drops. Similar results have been obtained by Kilpua et al. (2013) and Hietala et al. (2014).

Information on what kind of wave activity is present in the radiation belt system helps to better identify the dynamic processes acting on the radiation belt particles. It is also important to know whether the wave measurements were obtained inside or outside the plasmasphere to separate chorus from plasmaspheric hiss waves. However, as typically ULF Pc5, EMIC and chorus wave activity are all elevated during sheaths, it can be difficult to isolate the effects of these waves. It is often not evident which wave mode provides the dominant source of acceleration or loss (e.g., Shprits et al., 2018; Mann et al., 2018). Su et al. (2015) studied a time period where relativistic electron fluxes increased by an order of magnitude when there were strong ULF Pc5 wave activity but no chorus waves, demonstrating the potential of ULF waves for accelerating outer belt electrons. ULF and chorus waves can also act in synergy, with local acceleration by chorus providing the first and ULF-driven inward radial diffusion the second step of energization (Zhao et al., 2019a; Simms et al., 2021). All different waves (ULF Pc5, EMIC, chorus, hiss) are needed to produce realistic radiation belt conditions in simulations (e.g., Drozdov et al., 2020).

4.3 Electron flux response to sheaths

Sheaths excite strong wave activity and waves play a key role in radiation belt particle dynamics. Therefore, sheaths cause major variation in the outer radiation belt electron fluxes. It is difficult to predict how the belt reacts to a given solar wind transient, but statistical studies on how electron fluxes change when various sheath regions impact the Earth's magnetosphere build the groundwork to understand the dominant physical processes.

Some earlier studies of the outer belt sheath response have investigated electron fluxes at the geostationary orbit (Hietala et al., 2014; Kilpua et al., 2015). They showed that sheaths cause energetic electrons (> 2 MeV) to deplete significantly. Turner et al. (2019) studied the response in more detail using RBSP data to derive the response at a variety of energies and L-shells. They studied both full ICME events with sheath and ejecta, and events where only the sheath region impacted the magnetosphere. This study showed that these events depleted the outer belt at high energies (> 1 MeV) but effectively enhanced fluxes at lower energies. Depletion was more common for isolated sheaths than for the full ICME events, whereas enhancements at 10s to 100s keV were more common for the latter.

However, Turner et al. (2019) ignored the day of the impact and derived the

response from the maximum flux from 84 h to 12 h before the event and from 12 h to 84 h after the event. Thus, their results reflect the overall outer belt response to the events, and in the case of full ICME events include contributions from both the sheath and ejecta. Various studies have revealed much faster dynamics in the radiation belts. Soon after the launch of the RBSP, Reeves et al. (2013) reported that local acceleration appeared to be the dominant process enhancing electron fluxes significantly over 11 hours during a geomagnetic storm. The initial increase of a couple of orders of magnitude was observed to occur in 6 hours. Furthermore, Kim et al. (2021) identified rapid enhancements of MeV electrons that had timescales of 30 minutes, and also Olifer et al. (2021) resolved an outer belt electron flux enhancement over a period of only 30 minutes with RBSP data. However, such observations require some luck in the timing of the event with respect to the phasing of the RBSP orbits and cannot be continuously resolved with the data. Rapid dropouts have also been reported in the literature, for example, Olifer et al. (2018) revealed fast radiation belt losses on timescales from 30 minutes to 2 hours during geomagnetic storms using GPS data.

Thus, the outer belt response parameter must be derived on shorter timescales in order to resolve fast changes. A sufficiently short timescale also enables separating the response to different solar wind structures arriving in succession (instead of relying on serendipitous events when the structure of interest arrives in isolation) – in this case, to separate the response to sheaths from the response to ejecta. In Paper I, the impact of the selected 37 sheath events on the outer belt electron fluxes was investigated on a timescale of 6 hours. To reveal further details while maintaining the response as a function of a range of electron energies and L-shells, a data set with broader coverage is needed. As discussed in Section 3.1, the GPS constellation can provide such data and enable deriving the response parameter from fluxes only 30 minutes before and after sheaths. Therefore, the response study was repeated with GPS data on a timescale of 30 minutes in Paper III.

4.3.1 Flux response results for all sheath events

The results of Paper I and Paper III are shown in Figure 4.2. First, it is explained how to read the plot. The first three columns show the likelihood of enhancement, depletion and no significant changes as defined in Section 3.2.3 based on the value of the response parameter. The 6-hour response from RBSP data covers L = 2.5–6.4 (top row) and the 30-minute response from GPS data covers L = 4–6.9 (bottom row), and the bin size in L is 0.1. The GPS response has been calculated between 140 keV to 4 MeV at the energies corresponding to the energy channels of the RBSP

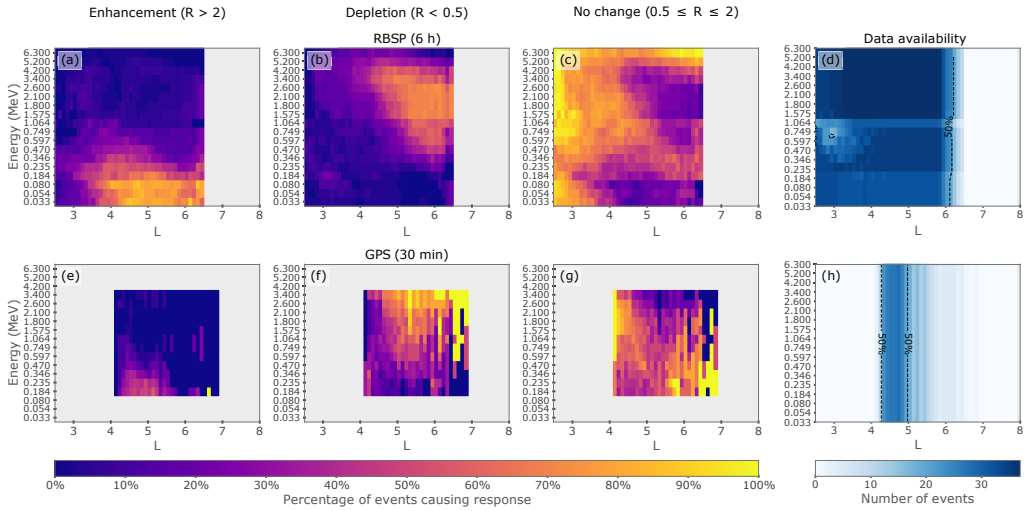

Figure 4.2: Outer belt electron flux response calculated from 6-hour averaged RBSP data (top) and 30-minute averaged GPS data (bottom). The panels show the fraction of sheath events at each energy and L bin, compared to the number of sheaths where data is available in each bin, causing (a, e) enhancement, (b, f) depletion or (c, g) no significant change in flux. For any energy-L pair, the sum of percentages in that bin from all three categories is 100%. Panels (d, h) show the number of events where data is available, i.e., where the response parameter could be calculated at the given timescale at each energy and L bin. The dashed lines indicate where data is available from over half of the events. Reproduced from Paper III.

particle instruments. For each of the 37 sheath events, the response was categorized in each energy-L bin, and the number of sheaths causing a specific response in each bin was counted. This number was converted to a percentage value by dividing it by the number of events where data was available. Therefore, each panel indicates the percentage of sheath events causing enhancement, depletion or no change in each energy-L bin, i.e., the colors represent the likelihood of the different responses based on statistics from the 37 sheath events.

The data availability is shown in the last column of Figure 4.2. It shows the number of events where flux measurements are available in the 6-hour or 30-minute intervals both before and after the sheath, so that the response could be calculated. This indicates how the 6-hour timescale sufficiently captures the outer belt response at all energies and L-shells for almost all events. Despite the higher data density of the GPS, good data coverage is very limited and it was possible to calculate the

30-minute response for more than half of the events only at $L \sim 4$–5. This highlights how deriving the outer belt response at a timescale of only a few tens of minutes is pushing the GPS data usage to the limits of its resolution.

The energy and L-shell dependent outer belt electron flux response to the investigated sheaths, combining the results derived from RBSP and GPS data, is as follows:

1. Enhancement is common at 10s to 100s keV, occurring at $L > 4$ in more than 50% of the events. The likelihood of enhancement at higher energies (400–800 keV) increases with decreasing L. The 10s to 100s keV electrons are rarely depleted.

2. Depletion is common for relativistic and ultrarelativistic electrons, occurring in more than 50% of the events at > 1 MeV energies at $L > 4$. With increasing L, the likelihood for depletion increases at lower energies (reaching about 400 keV). The MeV electrons are rarely enhanced.

3. No changes are typical in the inner part of the outer belt ($L < 3$) and in the L-dependent energy range between the enhancement at lower and depletion at higher energies, which form a band of no changes throughout the belt ($L = 4$–6).

Below, the likely physical processes leading to these statistical responses at different energies in different parts of the outer belt are hypothesised with clues from the results of the superposed epoch analysis.

Enhancement Outer belt electron fluxes at 10s to 100s keV energies at $L > 4$ are enhanced likely as the result of substorm injections. The injected low-energy electrons provide a source for chorus waves which further energise the injected electrons via local acceleration. Wave activity of both chorus and ULF Pc5 waves is significantly elevated during sheaths, as shown by the superposed epoch analysis. This implies that both local acceleration and inward radial diffusion can contribute to the outer belt electron flux enhancements, especially up to 1 MeV energies and below $L \sim 4$ where injections do not reach. Additionally, adiabatic processes (i.e., the Dst effect) cannot be ruled out as they can be present in the flux variations. The next chapter discusses the response analysis that was repeated for PSD, which reveals that only a part of these enhancements are due to actual, nonadibatic energization.

Chorus can accelerate electrons to energies > 1 MeV, but only in a few events are enhancements observed at such high energies. This implies that special conditions

are required for efficient and sustained acceleration to multi-MeV energies. Li et al. (2015a) showed that such conditions consists of prolonged southward IMF, high solar wind speed and low dynamic pressure, where the lowered pressure allows the magnetopause to move outward reducing the magnetopause shadowing losses that effectively deplete outer belt MeV electrons. Accelerating electrons to MeV energies can also require a longer timescale than is captured by this response analysis.

Depletion In agreement with the earlier sheath studies, depletion is common at MeV energies. Distinctively, the results show that sheaths also deplete 100s keV electrons at high L-shells, which was not observed by Turner et al. (2019) who considered longer time periods. This energy- and L-dependent response is therefore specifically a feature caused by the sheath and not the ICME event as a whole. Different loss processes likely dominate in different parts of the outer belt. At high L-shells, magnetopause shadowing removes electrons from the system as sheaths compress the magnetopause. The elevated ULF wave activity during sheaths likely enhances the losses via outward radial diffusion. Sustained magnetopause shadowing depletes all energies approximately equally, given that electrons reach the magnetopause, and thus the energy extent of the observed depletion is large at $L > 5$. At 10s keV energies the drift around the Earth can take several hours and thus the low-energy population can be only partly depleted before the magnetopause relaxes. Furthermore, the lack of depletion at 10s keV energies indicates that the substorm injections dominate the electron flux response at these energies.

At lower L-shells, less electrons are transported outward to be lost at the magnetopause, and the depletion likely becomes more dominated by energy-dependent WPI. Depletion is common only at > 1 MeV energies at $L < 5$. Electrons at these ultrarelativistic energies can be efficiently scattered and precipitate into the atmosphere via interactions with EMIC waves, whose wave activity is elevated during sheaths. EMIC waves tend to scatter electrons with low pitch angles below 45° (e.g., Usanova et al., 2014), so investigating the pitch angle distribution of outer belt electrons during sheath events could shed more light on the dominant loss mechanisms. Again, adiabatic effects could be included in the electron flux response. The PSD response is discussed in the next chapter, which reveals true losses to be common and supports the loss processes that were suggested here.

No change Electron fluxes largely remain within a factor of 2 from their pre-event values (no change response) in the inner parts of the outer belt. This is likely explained by the inner radiation belt, which extends to about $L \sim 3$, and the slot region at $L \sim 2$–4. The extent in L is dependent on energy, with the inner belt

reaching higher L-shells at lower energies and the slot region extending to higher L-shells at larger energies (Reeves et al., 2016). The inner belt populations are only weakly affected by magnetospheric disturbances and there are little high energy (> 1 MeV) electrons (e.g., Fennell et al., 2015; Li et al., 2015b). The slot region is characterized by the low level of fluxes, and especially electrons at larger energies ($>\sim 300$ keV) remain unchanged even during sheath impacts. At lower energies, the sheaths can cause the slot region to be filled, and some enhancements are observed at < 300 keV near $L \sim 3$ (see panel a in Figure 4.2).

The no change response is also common for 100s keV electrons at high L-shells ($L > 4$). This might not be due to lack of dynamics at this energy range, but might be explained by substorm injections quickly replenishing electrons that were lost during the event in those populations, as has been suggested by Turner et al. (2019). However, as discussed before, Turner et al. (2019) considered much longer timescales where there is plenty of time for recovery. Significant changes are neither observed at $L > 4$ with the 30-minute response from GPS data, which implies that the recovery must have taken place during the sheath region passage. More detailed studies of the outer belt variability during the sheath are needed to understand the response of the 100s keV electron populations at $L > 4$.

The processes that likely govern the outer belt electron dynamics in response to sheath impacts could be largely deduced from the 6-hour RBSP response (top row in Figure 4.2). The RBSP response was reproduced with 6-hour GPS data in Paper III, with high correlation between the results, indicating the good inter-calibration between these missions. The 30-minute GPS response (bottom row Figure 4.2) also evidences the similar response and has good correlation with the 6-hour RBSP response. Since computing the response from data only half an hour before and after the sheath largely ignores processes caused by the ejecta, this confirms that the energy- and L-dependent electron dynamics discussed above are caused by the sheaths.

However, the shorter timescale response reveals also some important differences. Namely, enhancement is less common and depletion is more common than in the 6-hour response. It is noted that this is not because of the low data availability for the 30-minute GPS response. Similar results were obtained when the response was recalculated from both RBSP and GPS for an identical set of events. This indicates that during the first 6 hours of the ejecta, electron fluxes are already being recovered. The recovery is not only due to substorm injections, which increase the likelihood of enhancement at < 500 keV, but also subsequent acceleration to higher energies takes place, which decrease the likelihood of depletion at > 500 keV. The prevalence of

magnetopause shadowing losses also decreases since the magnetopause relaxes and moves outward towards its nominal position and ULF wave activity wanes during the early ejecta as shown by the superposed epoch analysis. This higher tendency for sheaths to cause depletion was also found by Turner et al. (2019), who reported the response to isolated sheaths in comparison to full ICME events with both sheath and ejecta. The results presented in Paper III thus confirm that this is a characteristic of all sheath regions.

It is remarked here that with the response analysis, even when studying the change immediately (30 minutes) after the sheath, only changes resulting from the impact of the entire sheath region are considered. This is due to how the response parameter is defined as the ratio of the post-event to the pre-event fluxes, i.e., it does not consider how the fluxes vary during the sheath period. For example, during the sheath event featured in Figure 3.1, flux of ultrarelativistic electrons was enhanced for a few hours, but the calculated response parameter would only show the overall depletion. Studies detailing the timescale of changes that occur during the passage of the multi-hour sheath regions are required to further deepen the understanding of outer belt electron dynamics in response to magnetic disturbances driven by solar wind transients.

4.3.2 Flux response results for sheath events divided by their geoeffectiveness

Figure 4.3 shows the outer belt electron flux response to geoeffective and nongeoeffective sheath events in the same format as before, calculated from RBSP data. The 30-minute response is also reported from GPS data in Paper III, which reproduces the results.

It is evident that the impact of geoeffective sheaths results both in more enhancements and more depletion of the electron fluxes. The results of the superposed epoch analysis for sheaths divided based on their geoeffectiveness implies that geoeffective sheaths provide more favorable conditions for both efficient energization and losses. Geoeffective sheaths are associated with stronger substorm activity, higher wave activity of all wave modes and stronger compression of the magnetopause as shown in Paper I. Thus, there are more substorm injections and acceleration via WPI, as well as more loss at the magnetopause, with contributions from ULF-driven radial diffusion and scattering by EMIC waves.

For nongeoeffective sheaths, the no change response is clearly more common. However, importantly, significant changes in the electron flux are also caused by nongeoeffective sheaths with similar energy and L-shell dependence at higher L-

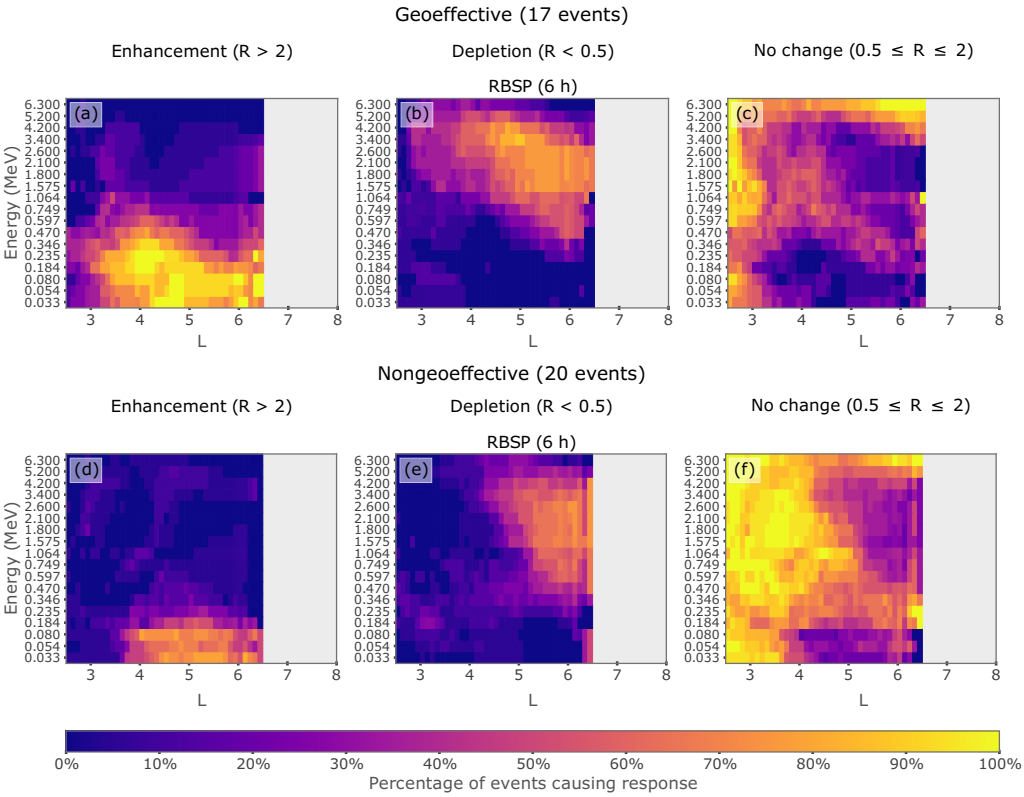

Figure 4.3: Outer belt electron flux response calculated from 6-hour averaged RBSP data for (a–c) geoeffective and (d–f) nongeoeffective sheath events. The format is the same as in the top row of Figure 4.2. Reproduced from Paper I.

shells. The difference is that nongeoeffective sheaths affect only the outer parts of the outer belt at $L > 4$, whereas the effects of geoeffective sheaths reach deeper in the belt and enhancements and depletions are observed throughout the outer belt.

The response of geoeffective sheaths is in agreement with the study by Turner et al. (2019) who analysed events associated with geomagnetic storms and reported significant changes in fluxes down to $L \sim 3$. Since the work presented in this thesis did not restrict the selection of events based on their geoeffectiveness, it could be shown that also sheaths with a weak geomagnetic impact can be important drivers of the radiation belt dynamics. The work thus emphasizes the need to take into consideration also events that do not drive geomagnetic storms when investigating how electron fluxes change in the outer radiation belt.

Finally, it is again noted that the changes in electron fluxes can be caused by fully adiabatic processes, which are reversible and thus do not reflect true energization or losses. In order to extract information on the nonadiabatic processes, the response is calculated from PSD in the next chapter, which reveals a more fundamental difference between the electron dynamics caused by geoeffective and nongeoeffective sheaths.

5 Electron energization and loss mechanisms revealed by phase space density analysis

ICME-driven sheaths are associated with plenty of wave activity in the inner magnetosphere, which provides avenues for efficient WPI that can accelerate, scatter or transport outer radiation belt electrons. Therefore, it is especially interesting to study outer belt electron PSD and the processes that drive the electron dynamics during the impact of sheaths. This chapter discusses the outer belt response, similar to the previous chapter, but considering PSD computed from RBSP and GPS data at 6-hour and 30-minute timescales, respectively. The results for geoeffective and nongeoeffective sheaths are compared and important differences in the dominant mechanisms are observed. This chapter also exemplifies the identification of acceleration, transport and loss processes from PSD radial profiles and observations of concurrent wave activity during two selected sheath events representing a geoeffective and nongeoeffective event. The results presented here are published in Paper II and Paper III.

5.1 Electron PSD response to sheaths

As explained in Section 2.2.2, PSD is a useful tool for analysing radiation belt dynamics, and the details on how to derive PSD values from RBSP and GPS data with the help of modeling were described in Section 3.2.4. The PSD response was calculated for the same 37 sheath events described in Section 4.1. The method for computing the response parameter was the same as employed in the previous chapter for electron fluxes (as defined in Section 3.2.3).

The results of the PSD response analysis are shown in Figure 5.1 where the response has again been divided based on whether the sheaths were geoeffective or nongeoeffective. The format is the same as in the figures of the previous chapter

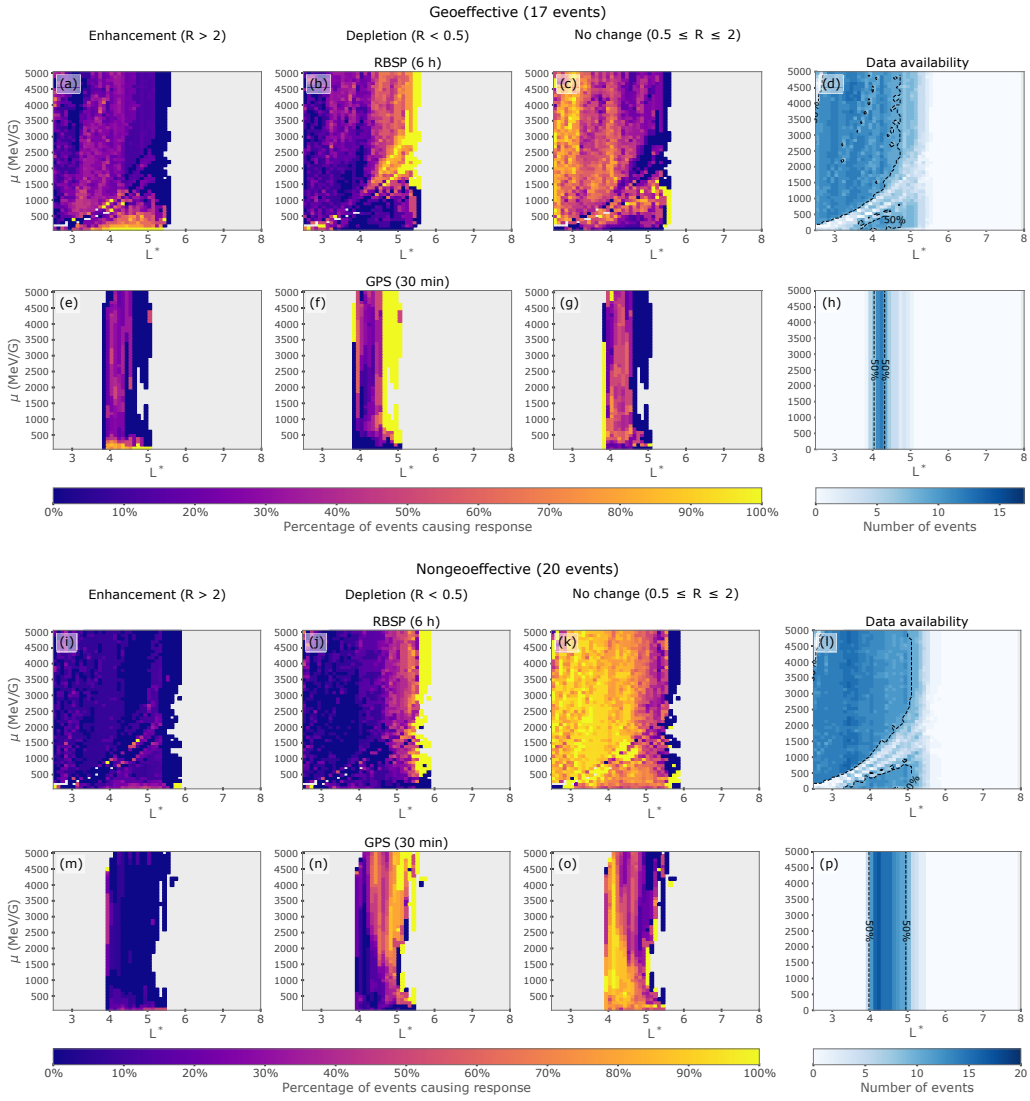

Figure 5.1: Outer belt electron PSD response calculated for geoeffective sheath events with (a–d) 6-hour averaged RBSP data and (e–h) 30-minute averaged GPS data, and for nongeoeffective sheath events with (i–l) 6-hour averaged RBSP data and (m–p) 30-minute averaged GPS data. The format is the same as in Figure 4.2, except that now the panels show the results for each μ and L^* bin. Reproduced from Paper III.

(cf. Figure 4.2), but the results are expressed in terms of the adiabatic invariants μ and L^* instead of energy and L-shell. The response was computed for a broad range of electron populations from $\mu = 100$ MeV/G to 5000 MeV/G, with increments of 100 MeV/G. The bin size is 0.1 in L^*. The PSD was considered for near-equatorially mirroring electrons with $K \leq 0.05\ \mathrm{R}_E\mathrm{G}^{1/2}$ for RBSP and $K = 0.02\ \mathrm{R}_E\mathrm{G}^{1/2}$ for GPS. It is noted that the calculation of RBSP PSD employed a range in μ which was 6.7% of the central value in order to increase the resolution (e.g., $\mu = (3000 \pm 100)$ MeV/G). Thus, after $\mu = (1500 \pm 50)$ MeV/G, the RBSP values start to slightly overlap with each other as the μ bin size is 100 MeV/G. This is not expected to have a considerable impact as the results were reproduced by the GPS data, whose data availability is higher for the 6-hour response at $L^* = 4$–5 (see Paper III).

For the 6-hour averaged RBSP response, data are available in a larger range at $L^* \sim 2.5$–6. The availability of the data is more restricted for the 30-minute GPS response, which stems from the very short timescale and the filtering performed in the calculation of PSD. There was GPS PSD both 30-minutes before and after the sheath for over half of the nongeoeffective sheath events at $L^* = 4$–5. For geoeffective sheaths, the data were more limited to $L^* = 4$–4.5. Nevertheless, the 30-minute GPS response evidences overall similar results as the RBSP response and the correlation between them is good.

The main findings from the results presented in Figure 5.1 are as follows:

1. Only geoeffective sheaths can be efficient at energizing outer belt electrons. Acceleration is observed for the 30-minute response at $L^* = 4$–5 for low μ (< 500 MeV/G) and for all studied populations at $L^* \sim 4$.

2. Both geoeffective and nongeoeffective sheaths can be efficient at driving loss of outer belt electrons, especially at $L^* > 4.5$.

Below, the likely nonadiabatic physical processes that can be inferred from the PSD response results and the differences in the importance of those mechanisms between geoeffective and nongeoeffective sheaths are discussed.

Enhancement Geoeffective sheaths can cause the electron PSD to enhance significantly, unlike nongeoeffective sheaths. It is however important to note that, while only geoeffective sheaths can produce conditions for efficient energization, not all geoeffective sheaths can accelerate electrons, as an enhancing response was observed for only about 30–40% of the sheaths for which data are available at $L^* \sim 4$. Energization at low μ is likely due to substorm injections, as geoeffective sheaths generally

induce strong substorm activity as shown, e.g., by Pulkkinen et al. (2007) and Paper I. At higher μ, acceleration is by WPI with chorus waves or ULF Pc5 driven inward radial diffusion which are common during sheaths and especially during the geoeffective ones. The 30-minute GPS response shows most acceleration at $L^* \sim 4$ where local peaks indicating local acceleration by chorus are frequently observed (e.g., Reeves et al., 2013; Li et al., 2014, 2016a; Turner et al., 2014a; Kanekal et al., 2015). Local acceleration is also expected to occur near the plasmapause (Horne et al., 2005; Boyd et al., 2018), which is typically located at a distance around 4–5 R_E during sheath regions as shown by superposed epoch analysis in Paper I, but there can be significant event to event variation. WPI with chorus can also accelerate electrons to MeV energies (Miyoshi et al., 2013; Jaynes et al., 2015) that correspond to the high μ values. Boyd et al. (2018) additionally showed that local acceleration is the dominant mechanism for outer belt electron energization during the RBSP era. Inward radial diffusion driven by ULF waves can further energize the electrons accelerated by chorus waves (Zhao et al., 2019a; Simms et al., 2021). Further inward at $L^* < 4$ the acceleration observed in the 6-hour RBSP response can likely also be caused by ULF-driven inward radial diffusion (e.g., Turner and Ukhorskiy, 2020). However, without confirmation from the 30-minute response at such low L^*, it cannot be confirmed if that acceleration is caused by the sheath or the early ejecta.

For nongeoeffective sheaths, the data availability is higher (almost 100% at $L^* = 4$–5 for the 6-hour GPS response as reported in Paper III), but practically no significant enhancements in PSD were observed, with a couple exceptions. Enhancements at very low μ values could be due to substorm injections (note that geoeffectiveness was determined using the SYM-H index that can be at non-storm values even though some relatively weak substorms would occur). There is substorm activity which further generates chorus waves also during nongeoeffective sheaths, even though it is not as dramatic as during sheaths associated with stronger geomagnetic activity, as shown in Paper I. The RBSP response also indicates acceleration at $L^* \sim 3$ in a few events, which, like above, can be caused by inward diffusion and might be caused by the ejecta instead of the sheath.

The observation of efficient outer belt electron acceleration generally only during geoeffective sheaths implies that the enhancements in electron flux during nongeoeffective sheaths (see Figure 4.3) are predominantly due to adiabatic processes. Paper I showed that the SYM-H index tends to increase during nongeoeffective sheaths, which weakens the ring current and, in turn, the geomagnetic field strengthens. In order to preserve the third adiabatic invariant, electrons move inward and cause fluxes to adiabatically increase at lower L^*. This can be thought as the opposite

counterpart of the Dst effect that occurs during geomagnetic storms.[1] However, it is noted that the studied electron fluxes were spin-averaged, whereas only the near-equatorial population was studied with PSD. In Paper III it was confirmed with pitch angle resolved RBSP data that these adiabatic enhancements are also seen in the 90° pitch angle electron population which is sampled by the computed PSD. Nevertheless, further studies of the PSD response at different K values and the directional fluxes at different pitch angles can deepen the understanding of the balance between adiabatic and nonadiabatic effects.

Depletion Both geoeffective and nongeoeffective sheaths can efficiently drive the loss of outer belt electrons at a large range of energies. Loss is observed at all sampled μ except for the very lowest values. Loss is frequently observed at the highest sampled L^* which implies that the loss is caused by magnetopause shadowing at the compressed magnetopause with contributions from outward radial diffusion driven by elevated ULF wave activity (Turner and Ukhorskiy, 2020), as was already discussed based on the flux response in Chapter 4. Comparing the 6-hour responses, the losses penetrate deeper into the outer belt during geoeffective events, reaching $L^* \sim 4$. However, the 30-minute response during nongeoeffective sheaths shows losses reaching down to $L^* \sim 4$ at the higher μ values (> 2000 MeV/G). The losses are also more common at these μ values than at the lower μ or in the 6-hour response. Since the magnetopause incursion is less dramatic and the ULF wave activity is less elevated for nongeoeffective sheaths (Paper I), it is unlikely that all losses were driven by the magnetopause shadowing process. At lower L^*, pitch angle scattering via WPI with, e.g., EMIC waves likely plays a major role in the losses. EMIC waves interact with ultrarelativistic electrons and can scatter them quickly (Aseev et al., 2017; Shprits et al., 2017; Kurita et al., 2018), which supports the higher likelihood of loss at higher μ values for the 30-minute response of nongeoeffective sheaths. EMIC-driven scattering can also contribute to loss during geoeffective sheaths during which the activity of these waves is higher. However, for geoeffective sheaths it is difficult to determine the μ and L^* dependencies of the loss, as the data availability is overall lower and also quickly drops to only a few events at $L^* > 4.5$.

No change For nongeoeffective sheaths, the no change response is much more common than for geoeffective sheaths. This is because there are less decreases in electron fluxes (see Figure 4.3) and, as discussed above, also more adiabatic processes

[1] In the Dst effect, the SYM-H index drops during the storm main phase, the ring current increases and the geomagnetic field weakens, causing the electrons to move outward.

during nongeoeffective events which conserve PSD. The response calculated from RBSP data that covers $L^* < 4$ confirms the conclusions in the earlier chapter as well, showing that geoeffective sheaths are able to affect the inner parts of the outer belt, whereas there are practically no changes in the electron populations in that region during nongeoeffective sheaths.

The PSD response also confirms the differences between the 6-hour and 30-minute responses discussed in Chapter 4. Accelerating events are more common (better shown by geoeffective sheaths) and losses are less common (better shown by nongeoeffective sheaths) with the longer timescale of 6 hours. This further confirms that the longer time period underestimates the losses driven by ICME sheaths as the outer belt electron populations are replenished during the early ejecta. The recovery is likely driven by substorm injections and subsequent energization, and the relaxation of the magnetopause location to further distances which lessens the efficiency of loss via magnetopause shadowing. As shown by the superposed epoch analysis (see Figure 4.1), the wave activity of ULF Pc5 and EMIC waves is also lower during the ejecta, decreasing the likelihood of loss, while the chorus activity is on a similar level and chorus can continue to locally accelerate electrons. It is noted, by comparing the 30-minute and 6-hour responses, that nonadiabatic energization takes places during the ejecta following nongeoeffective sheaths but only enough to recover the outer belt populations at $L^* \sim 4.5$ from the sheath-driven losses.

As for the electron fluxes discussed in the previous chapter, the response parameter analysis for PSD does not take into account the details of the changes during the sheaths. The response also does not consider the PSD radial profiles which strongly aid the identification of the physical mechanisms acting on the radiation belt electrons. Therefore, detailed case studies of the PSD evolution during the passage of the sheath are needed. Such case studies are presented in the next section.

5.2 Interpretation of PSD radial profiles during sheath events

Simplified schematics of the PSD radial profiles and their interpretations were discussed in Section 2.2.2. In general, local peaks indicate local acceleration, while a large decrease in PSD at high L^* is a sign of loss at the magnetopause. Identification of physical processes from real data can be tricky as many processes can act in tandem and the data provide only a snap shot of the outer belt conditions at the location of the spacecraft. For example, Olifer et al. (2021) showed that such

conditions could potentially lead to misinterpretation without careful analysis. Long gaps in the data, as has been seen to exist for RBSP, further complicate the picture that can be drawn of the temporal evolution of PSD. Thus, care must be taken when interpreting PSD radial profiles. The analysis can be supported by consulting simultaneous measurements of inner magnetospheric wave activity since they indicate which WPI processes can be expected occur (see Section 2.2.3). A comprehensive timeline can be constructed by gathering information on the different aspects of the system from many sources (e.g., Da Silva et al., 2020).

The PSD response showed a distinct difference between geoeffective and nongeoeffective sheath regions. Therefore, it is interesting to pick one sheath from both categories for more detailed investigation. The selected geoeffective sheath (SYM-H minimum of -90 nT) arrived at Earth on 2 October 2013 and its duration was 22.7 h. The nongeoeffective sheath (SYM-H minimum of -32 nT)[2] arrived on 15 February 2014 with a duration of 15.2 h. The response parameter considered the overall changes that occurred during those long sheath periods, so it is clear that the possible complexity of the response could be missed.

Figure 5.2 shows the PSD radial profiles calculated from RBSP data with the methodology presented in Section 3.2.4, and the data are smoothed to reduce fluctuations as described there. The profiles were calculated for nearly-equatorially mirroring electrons with $K \leq 0.05$ $\mathrm{R}_E\mathrm{G}^{1/2}$, corresponding predominantly to 70°–90° pitch angles, and for two μ ranges: (300 ± 10) MeV/G and (3000 ± 100) MeV/G. These ranges cover energies at 100s of keV and several MeV, respectively. The energies and pitch angles corresponding to the chosen ranges of these adiabatic invariants depend on L^* (see Figure 2.4). The corresponding energy decreases with increasing L^*.

Before scrutinizing the shape and evolution of the PSD radial profiles, the simultaneous conditions in the radiation belt system are considered for context. These are collected in Figure 5.3. The solar wind parameters for the two sheaths and the intensity of the geomagnetic activity they cause are shown on the left. The geoffective sheath clearly caused a geomagnetic storm with strong substorm activity both near the start and end of the sheath, whereas the nongeoffective sheath had some substantial substorm activity only near the end of the sheath. This activity excited chorus waves in these locations, as shown on the top right of Figure 5.3. The RBSP missed the dawn side, where chorus waves predominantly occur (Lam et al., 2010), for both events. Thus, chorus activity was inferred from a proxy based on precipitating electron measurements (scattered to the loss cone via WPI with chorus) from

[2]This is below the threshold of -30 nT used to define nongeoeffective events earlier, but the minimum is reached at the very end of the sheath and the SYM-H actually remains positive during most of the sheath (see Figure 5.3).

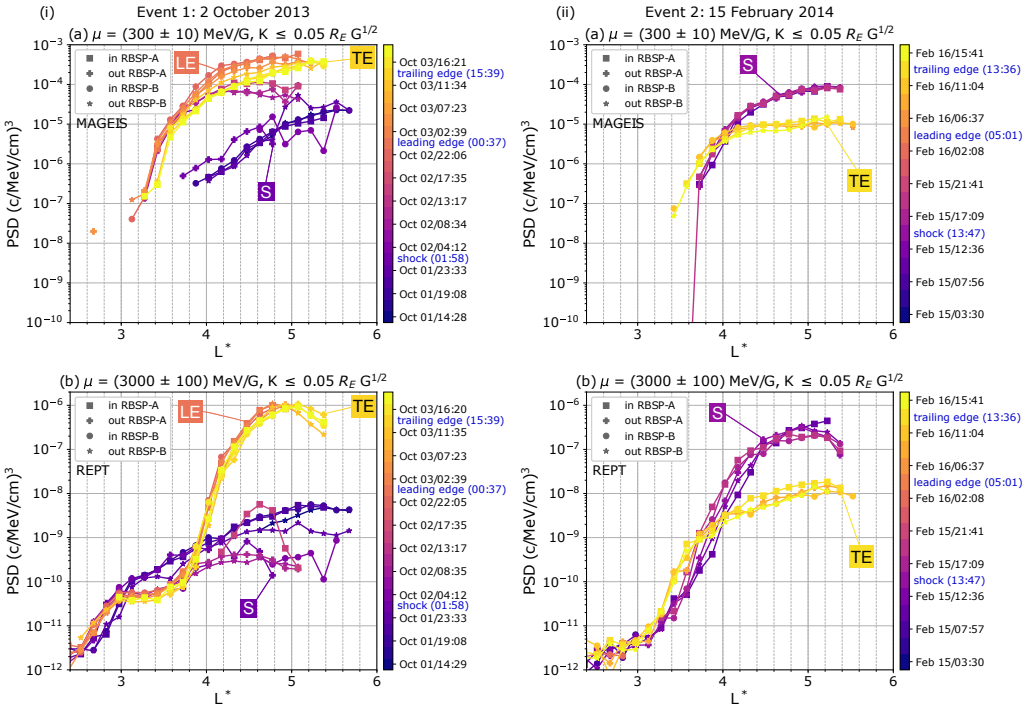

Figure 5.2: Radial profiles of RBSP PSD for (i) geoeffective and (ii) nongeoeffective sheaths. PSD is calculated for (a) $\mu = (300 \pm 10)$ MeV/G and (b) $\mu = (3000 \pm 100)$ MeV/G which correspond to electron energies ∼600 keV and ∼3 MeV at $L^* = 4$ and ∼400 keV and ∼2 MeV at $L^* = 5$, respectively. Each profile represents an inbound or outbound pass of the two RBSP spacecraft, indicated by different marker shapes (see legend). The color of each profile indicates the time which is shown on the color bar. The passes that occur during the shock (S), ejecta leading edge (LE) and ejecta trailing edge (TE) have been identified and the timing of these boundaries are indicated in blue. The sheath region is between the S and LE boundaries. Reproduced from Paper II.

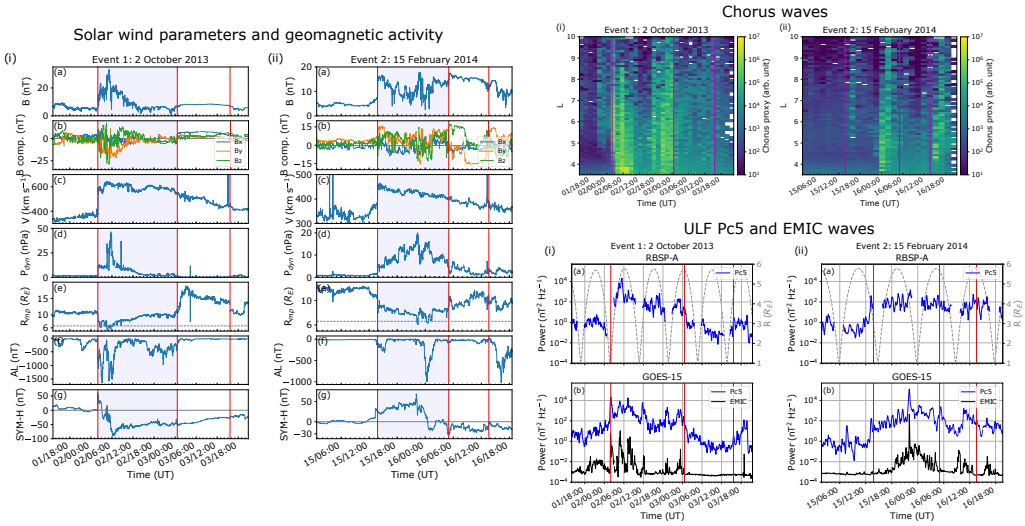

Figure 5.3: Properties of the geoeffective (Event 1) and nongeoeffective (Event 2) sheaths on the left, and the radiation belt wave conditions on the right. Left: magnetic field magnitude and components, solar wind speed and dynamic pressure, modeled magnetopause location (Shue et al., 1998), AL index for substorm activity and SYM-H index for geomagnetic activity. Right: Chorus waves from POES proxy, and ULF Pc5 and EMIC wave power from RBSP and GOES-15. Reproduced from Paper II.

POES data, as was briefly described in Section 3.1.4. Both events also compressed the magnetopause briefly below the geostationary orbit (at 6.6 R_E). For the nongeoeffective sheath, the magnetopause was compressed for a longer period owing to the broader dynamic pressure pulse. The lower panels on the right show the ULF Pc5 and EMIC wave activity from geostationary orbit measured by GOES-15 and ULF Pc5 waves from the heart of the outer belt as observed by RBSP. The Pc5 activity was similar between the RBSP and GOES measurements confirming the global nature of these waves during the considered events. The wave activity of both Pc5 and EMIC waves was elevated during both sheaths.

Below, the processes likely causing the observed PSD radial profiles for each sheath are discussed. The overall conclusions are as follows:

1. The geoeffective sheath mainly caused energization due to the stronger substorm activity driving more injections and generating more chorus waves that subsequently accelerated electron locally to MeV energies. The pressure pulse associated with this sheath was brief causing the magnetopause to recover

quickly, and as a consequence, no signifanct loss at the magnetopause is expected.

2. The dynamics driven by the nongeoeffective sheath were overall the opposite, as it predominantly caused magnetopause shadowing losses. The pressure pulse was broader and compressed the magnetopause longer, enabling efficient conditions for loss combined with outward radial transport, dominating over any energization that could have been driven by the weak substorm activity.

Geoeffective sheath There are two distinct features in the PSD profiles that imply two different energization mechanism in action during the geoeffective event: increasing positive slope and local peak (cf. panels a and b in Figure 2.3). At the 100s keV energies (top left panel in Figure 5.2, see purple to orange profiles), the slope of the PSD profile is positive and PSD increased with time in two steps. The first step of about two orders of magnitude occurred at $L^* > 3.8$ during the early sheath, and the latter at $L^* > 4$ and about one order of magnitude near the end of the sheath. Both enhancements coincided with strong substorm activity, thus indicating injections of electrons at the sampled energies. The increases also suggest an increasing source population at higher L^* (Chen et al., 2007). ULF-driven inward diffusion can further transport these electrons to the observed range. There is also enhanced activity of chorus waves in the key sub-regions near the start and end of the sheath, which can contribute to the observed enhancements, but no local peak can be identified for $\mu = 300$ MeV/G. Additional measurements beyond the RBSP orbit would be needed to resolve a negative slope if there is any.

On the other hand, there is a local peak at $L^* \sim 4$–5 corresponding to 1.5–3 MeV electrons seen with $\mu = 3000$ MeV/G (bottom left panel in Figure 5.2, see magenta to yellow profiles). The substorm injections provided the seed population to be further accelerated to MeV energies by WPI with the chorus waves (Jaynes et al., 2015; Boyd et al., 2016). The peak growth is only captured by one RBSP satellite (PSD could not be calculated at the chosen μ and K from the other probe at that time), meaning that there is about a 9-hour gap between the magenta and orange profiles, which introduces some uncertainty in the interpretation. Overall, the PSD increased three orders of magnitude in 12 hours. However, local peaks in this L^* range are commonly observed (e.g., Kanekal et al., 2015; Reeves et al., 2013; Li et al., 2014, 2016a; Turner et al., 2014a) and similar growth rates, when diffusion simulations confirm chorus as the main driver of acceleration, have been reported (e.g., Thorne et al., 2013; Li et al., 2014, 2016a). In addition, Boyd et al. (2018) confirmed the existence of the local peak in this event by using data from the THEMIS spacecraft

that reaches $L^* > 5$.

The PSD peak was first observed around the middle of the sheath and it persisted throughout the rest of the event (i.e., at least 12 hours), which strongly indicates that there is an active energization source, such as local acceleration or a sustained source population further out. Otherwise, the peak would flatten over time due to ULF-driven radial diffusion. There are no signatures of inward radial diffusion at these energies, which supports the conclusion that the peak was formed by local acceleration.

Some loss processes can also be identified in the PSD profiles for $\mu = 3000$ MeV/G. There was a brief loss at the start of the geoeffective sheath for the MeV electrons, coinciding with the deepest magnetopause incursion, which suggests losses at the magnetopause (cf. panel e in Figure 2.3). This loss was not seen at the lower energies, which could be explained by rapid recovery by the substorm injections and the magnetopause quickly recovering not allowing as much time for the loss as for the faster higher energy electrons. There also appears to be a dip in the profiles near $L^* \sim 3.3$ (compare purple to yellow profiles) that occurs during the first half of the sheath. It is a signature of local loss (cf. panel f in Figure 2.3), which is likely caused by WPI with EMIC waves (Aseev et al., 2017; Shprits et al., 2017) whose activity was elevated during that time. EMIC-driven scattering typically dominates losses at low pitch angles (Usanova et al., 2014), but they can also drive fast losses for near-equatorially mirroring electrons (Drozdov et al., 2019) that were sampled with the chosen K range. Depletion of MeV electrons is common but the dominant causes are not clear (e.g., Turner et al., 2013, 2014a,b; Aseev et al., 2017). It is also possible that the appearance of a dip was created by the combination of magnetopause shadowing reaching low L^* when local acceleration had already begun at higher L^*. This highlights the difficulty in interpreting PSD profiles when different mechanisms take place simultaneously.

Nongeoeffective sheath The interpretation of the PSD radial profiles during the nongeoeffective sheath is more straightforward. For both 100s keV and MeV energies, there is a clear decrease in PSD at $L^* > 4$ of about an order of magnitude in 13 hours (right hand panels in Figure 5.2, see purple to yellow profiles). The dropout occurred in the latter half of the sheath. There however was no RBSP PSD available at the chosen adiabatic invariant coordinates during the dropout, so it remains unresolved whether the loss was slow or abrupt. In any case, such large decreases are indicative of loss at the magnetopause as mentioned earlier. The ULF wave activity was also elevated during the whole nongeoeffective sheath which could drive radial diffusion. This is confirmed for both μ ranges where

the PSD increased at $L^* < 4$ during the loss, i.e., electrons were transported inward and thus, at the same time, outward diffusion was also taking place. Turner and Ukhorskiy (2020) described how the increasing PSD at lower L^* and decreasing PSD at higher L^* are a signature of magnetopause shadowing where ULF-driven outward diffusion contributes to losses at the compressed magnetopause.

The difference of the two events is clear and it echoes the general conclusions of the statistical PSD response discussed in the previous section. Losses occurred during both sheaths. However, the much weaker substorm activity during the non-geoeffective sheath did not produce sufficient chorus activity to overtake the losses, in contrast to the geoeffective sheath. The relatively fast recovery of the compressed magnetopause during the geoeffective event provided conditions for efficient energization to MeV energies (Li et al., 2015a).

It is noted that there can be large gaps in the RBSP PSD data. They are due to both the inherent low time resolution of a two satellite mission as discussed in Section 3.1.3 and the fact that the probes are not always measuring electrons in the appropriate ranges of μ and K. Because of this, the timescales of the acceleration and loss processes during the geoeffective and nongeoeffective sheath, respectively, could not be resolved beyond a timescale of several hours. Complementing data sets, such as provided by GPS, must thus be utilized in order to reach more detailed understanding of fast radiation belt processes.

6 Conclusion and Outlook

The work presented in this thesis aimed to deepen the understanding of the impact of ICME-driven sheath regions on the radiation belt system. The goal was achieved utilizing multi-point and multi-satellite data sets to gather a comprehensive picture of the radiation belt dynamics, especially those governing the outer belt electrons. In the following, the contribution of this doctoral research to radiation belt science and the interesting future avenues for further work are discussed.

6.1 Impact of thesis work

To briefly summarize the work presented in this thesis, turbulent sheath regions associated with ICMEs can drive significant changes in the outer radiation belt electrons. This arises from the strong compression of the magnetopause and the diverse, high wave activity caused by the sheaths (Paper I), which provide conditions for both energization and loss. Low energy (10s to 100s keV) electron fluxes typically experience enhancement and ultrarelativistic (> MeV) fluxes are depleted, but both also evidence a dependence on the radial location with higher energy electrons being enhanced with decreasing L-shell and lower energy electrons being depleted with increasing L-shell (Paper I and Paper III). Geoeffective sheaths (SYM-H < -30 nT) can cause changes throughout the outer belt, but also nongeoeffective sheaths can play an important role in the outer belt variability. This work highlighted the importance of high data density in resolving the response on short timescales. This allowed confirming that the changes were driven specifically by the sheath region (Paper III). PSD analysis revealed the dominance of sheath-driven losses and showed that only geoeffective sheaths can provide favorable conditions for efficient electron acceleration (Paper II and Paper III).

Paper I presented the first comprehensive statistical study of the overall geospace response to sheath regions. The analysis included a variety of parameters from the sheath properties to the induced wave activity and changes in outer belt electron fluxes. Solar wind characteristics of sheaths and their impact on geomagnetic activ-

ity have been investigated previously (e.g., Kilpua et al., 2019), but Paper I combined these observations with various wave data to provide context for the electron dynamics. This study also focused on sheath events observed in the recent years when high quality measurements from the RBSP are available. This is in contrast to earlier work utilizing flux measurements at the geostationary orbit (e.g., Hietala et al., 2014; Kilpua et al., 2015), which are unable to address the detailed L-shell and energy dependencies of the response, thus missing the clear distinction in the response of the low energy and the ultrarelativistic electron populations (predominant enhancement and depletion, respectively). Importantly, Paper I considered the electron flux response on a much shorter timescale than previous studies using RBSP data (Turner et al., 2015, 2019). Thus, the energy and L-shell resolved response could be shown, for the first time, specifically for the sheath region in events where the sheath and ejecta impact the magnetosphere in succession. Furthermore, the study emphasized that sheaths do not need to cause strong geomagnetic activity in order to significantly affect the outer belt electrons. Nongeoeffective sheaths can produce a similarly energy-dependent response, albeit only in the outer parts of the outer belt ($L > 4$). This motivates the radiation belt community to consider also less geoeffective sheath events and detail the wave-driven radiation belt variability during them, such as done by Da Silva et al. (2020).

Paper II studied further the outer belt electron dynamics, comparing and contrasting the changes driven by a geoeffective and nongeoeffective sheath. The notable upgrade from the previous work discussed above, in terms of identifying the dominant nonadiabatic, physical mechanisms, was computing PSD. This quantity enabled, with careful analysis of concurrent wave activity and other magnetospheric conditions, showing that the overall response was the opposite during these two sheaths. The geoeffective sheath mainly caused electron energization, but also some loss, and the nongeoeffective sheath led to significant losses. This work adds to the understanding of the key processes driven by the impact of sheaths, showing that, at least in these two events, all major changes occurred during the sheath and not the ejecta. The study also illustrated the importance of utilizing various data sources, such as the chorus proxy, to identify the processes confidently.

Additionally, Paper I and Paper II showed that there are key sheath sub-regions, which have been noted also in other studies. There tends to be large variability near the start and the end of the sheath. That is, these regions are the most geoeffective (Kilpua et al., 2019) with strong substorm activity (Paper I), and cause enhanced ULF wave activity (Kilpua et al., 2013; Ala-Lahti et al., 2021) and enhanced chorus activity that was identified from enhanced electron precipitation (Paper II). Since Paper II studied the changes in electron flux and PSD during the sheath region (as

opposed to the response studies), it was found that the most notable changes occurred also near these important sub-regions. More finer scale sheath sub-structures, which have distinct impact on the outer belt electrons, have also been observed (Blum et al., 2021b). These observations highlight the need for resolving small spatial and temporal scales during sheaths to capture all dynamics.

Paper III generalised what was observed in the case study of Paper II for a larger set of sheath events, namely that loss is commonly caused by sheaths, but acceleration is only observed during geoeffective sheaths. This strengthens the view of sheaths as key drivers of loss (e.g., Kilpua et al., 2015; Alves et al., 2016; Da Silva et al., 2020). However, the study also highlighted that certain sheaths produce significant energization, especially together with geoeffective ejecta (Turner et al., 2019), so understanding which properties enable acceleration processes to dominate is key for space weather forecasting of ICME impact. The conclusions of Paper III of the outer belt response to sheaths were especially reinforced and the energy and location dependency of the response confirmed with GPS data that provide observations at much shorter timescales than RBSP. Thus, this work highlighted the applicability and usefulness of GPS data for scientific use, as advocated by Morley et al. (2016, 2017).

Finally, the broader impact of the work presented in this thesis is to the understanding of the near-Earth space environment response to specific solar wind driver structures. Combining efforts in analysing the different aspects of the response will allow to enhance models of the radiation belt system and improve the forecasting of space weather.

6.2 Outlook

The dynamics of energetic outer radiation belt electrons vary from less than an hour to several days. Knowledge on the relatively slow variability is steadily increasing (see, e.g., the review by Baker et al., 2018), with the main emphasis on modeling radial diffusion that generally acts on timescales of multiple hours or even days (e.g., Lejosne and Kollmann, 2020). The variations on shorter timescales are clearly less understood and there is a need for resolving these faster dynamics. For example, it is believed that EMIC waves drive fast local losses (e.g., Kurita et al., 2018) and chorus waves drive fast local acceleration (e.g., Foster et al., 2017). These also highlight the localized nature of important dynamics on short timescales. Furthermore, processes that can act on very short timescales are associated with nonlinearity, which has been recognized to play an important role for electron energization and loss (e.g., Foster

et al., 2017; Hendry et al., 2019; Hsieh et al., 2020; Osmane et al., 2022). Tools from information theory can be applied to evaluate the significance of nonlinear processes, for example, mutual information (Osmane et al., 2022; Wing et al., 2022).

Rapid radiation belt processes have been reported by studies employing the RBSP data, but they typically rely on serendipitous measurements (e.g., Olifer et al., 2021; Kim et al., 2021). As presented in this thesis, data from the GPS constellation enable resolving the radiation belt electron flux continuously on timescales of only tens of minutes at a given L-shell with broad coverage around the Earth. GPS PSD also compares well with PSD calculated from RBSP data, despite needing more modeling. The recently released GPS data set is thus an excellent resource to utilize in the future works to capture the more detailed, and thus far largely elusive, short timescale dynamics (e.g., Morley et al., 2010; Olifer et al., 2018).

For future developments in understanding the outer belt response to ICME-driven sheath regions, the GPS data set can be employed to investigate the energetic electron variability thoroughly and in detail during the sheaths, not only considering the net effects as given by the response parameter (Paper I and Paper III). The analysis in Paper II uncovered concurrent processes and switching from loss to acceleration, but was hindered by the gaps in RBSP data. GPS data can fill these gaps, and allow for statistical studies on the typical timescales of the changes that have not been resolved comprehensively before with high temporal resolution. The results can be compared to timescales associated with WPI with different waves modes predicted from theory or modeling. This can also be used to investigate the specific effects of discrete structures within the sheaths (Blum et al., 2021b).

More generally, the GPS data set can be used in a similar manner to investigate the electron flux response in finer temporal and spatial scales during other solar wind transients, such as ICME ejecta and slow-fast stream interaction regions. Indeed, there is a lack of extensive analyses of rapid radiation belt processes due to the lack of missions providing sufficiently high data density, until recently with the GPS data release (Morley et al., 2017). This data can also serve as input and benchmark to radiation belt models exploring effects of different acceleration, transport and loss processes (e.g., Bourdarie et al., 2005; Sorathia et al., 2018; Chen et al., 2019; Cervantes et al., 2020; Drozdov et al., 2020). Additionally, the GPS constellation can take the role as the successor of RBSP in monitoring the radiation belt dynamics after the end of the RBSP mission, until more dedicated science missions shall be launched. Another apparent advantage of the GPS data set is its long history, from 2001 to present day. This data set is foreseen to give access to myriad case and statistical studies on an unprecedented temporal resolution.

As presented in this thesis, there is a good synergy between GPS and RBSP

data, and these data can be combined to capitalize the strengths of both missions. Similarly, RBSP data has been complemented with energetic electron measurements from the MMS or THEMIS missions (e.g., Boyd et al., 2018; Cohen et al., 2021; Turner et al., 2021). Such missions cover the outer belt at larger radial distances, thus providing important additional information on the slopes of PSD radial profiles. This can confirm the existence of local peaks at high L^*, when RBSP data by itself could not provide sufficient evidence for local acceleration. Multi-point and multi-satellite observations (RBSP, GPS, MMS, THEMIS, GOES, POES, Arase, Wind, etc.) and ground-based observatories will provide the basis for upcoming pioneering radiation belt research and collaboration. The utilization of the available data sets enables comprehensive analyses to understand each component of the outer belt electron response to sheaths and other drivers.

The next step in radiation belt monitoring along bigger international missions is provided by nanosatellites. In recent years, the popularity of these small satellites has surged and they have become feasible for smaller scale science missions, often involving major contributions from students. Such missions include targeted observation of precipitating fluxes at low Earth orbits, but some aim for orbits in the heart of the outer radiation belt where the radiation conditions are harsh. Thus, the development of new innovations with miniaturisation and sufficient radiation hardness are needed. The author of this thesis has been involved with the Finnish Centre of Excellence in Research of Sustainable Space (FORESAIL) cubesat mission (Palmroth et al., 2019). The three satellites in this mission will provide insight into the precipitating and trapped electrons on the level of earlier big science missions. Other small scale radiation belt missions include the Colorado Student Space Weather Experiment (CSSWE; Li et al., 2013b), the Electron Loss and Fields Investigation (ELFIN; Angelopoulos et al., 2020), the GTOSat mission (Blum et al., 2021a) and many others.

In conclusion, there are now a wealth of data sets and tools that can be used to study the radiation belt particles and wave activity. They provide avenues for interesting future research that will address the detailed radiation belt system response to ICME-driven sheaths and other solar wind transients on shorter timescales than what has been resolved before.

7 Summary of papers and the author's contribution

7.1 Paper I

Kalliokoski M. M. H., Kilpua E. K. J., Osmane A., Turner D. L., Jaynes A. N., Turc L., George H., Palmroth M. (2020), Outer radiation belt and inner magnetospheric response to sheath regions of coronal mass ejections: a statistical analysis, *Annales Geophysicae, 38*, 683–701, doi:10.5194/angeo-38-683-2020.

Summary: A comprehensive statistical analysis of the solar wind properties and magnetospheric impact of 37 ICME-driven sheath regions during 2012–2018. The study shows the overall trends in solar wind parameters, geomagnetic activity, inner magnetospheric plasma wave activity, and outer belt electron fluxes during sheaths. Superposed epoch analysis of waves shows that the wave power of ULF Pc5 and EMIC waves, as measured at the geostationary orbit, is elevated during the sheaths in comparison to the pre-event and ejecta levels. Activity of chorus waves is elevated during the sheaths and ejecta due to the continuous substorm activity during the ICMEs. Sheaths predominantly deplete high-energy outer belt electrons (> 1 MeV) and the likelihood of depletion at 100s keV energies increases with increasing L. Flux enhancements in response to sheaths are common at lower energies (10s to 100s keV) throughout the outer belt. The study suggests that outer belt electron loss is dominated by magnetopause shadowing at large L and by WPI in the heart of the belt. There is higher wave activity and significant changes in outer belt electron fluxes are more common during geoeffective sheaths, but clearly elevated wave activity and significant enhancement and depletion occurs also during nongeoeffective sheaths. The energy- and L-dependent outer belt response was revealed specifically due to employing a short 6-hour timescale in the analysis.

The author's contribution: Selected the sheath events from event catalogs and

checked solar wind data to adjust the event timings. Derived ULF wave activity from GOES measurements. Developed and coded the data analysis programs to carry out the superposed epoch analysis and the response parameter analysis, both for all events and events divided by geoeffectiveness. Performed the data analysis and produced the figures. Interpreted the results and wrote the manuscript with contributions from co-authors. Presented the results in international scientific conferences.

7.2 Paper II

Kalliokoski M. M. H., Kilpua E. K. J., Osmane A., Jaynes A. N., Turner D. L., George H., Turc L., Palmroth M. (2022), Phase space density analysis of outer radiation belt electron energization and loss during geoeffective and non-geoeffective sheath regions, *Journal of Geophysical Research: Space Physics, 127*, e2021JA029662, doi:10.1029/2021JA029662.

Summary: Case studies of the energization and loss mechanims governing the outer radiation belt electron dynamics during a geoeffective and a nongeoeffective ICME-driven sheath region. The PSD radial profiles calculated from RBSP data were investigated along with observations of wave activity to identify the dominant acceleration, transport and loss processes. The PSD was analysed for a broad range of electron populations from 10s of keV to ultrarelativistic (> MeV) energies. The geoeffective sheath predominantly caused energization by substorm injections and chorus-driven local acceleration, whereas the nongeoeffective sheath led to losses at the compressed magnetopause with contributions from ULF-driven outward radial transport. Thus, both sheath events caused significant, nonadiabatic changes in the outer belt electrons but the overall responses were the opposite. The study showed that this distinct difference arose from the different levels of substorm activity driving chorus waves during the events and the different timing of the elevated dynamic pressure in the sheaths. The study also highlighted key sheath sub-regions where significant variation in the radiation belt system occurs. They are located near the shock and the ejecta leading edge, i.e., near the start and end of the sheath region.

The author's contribution: Selected the sheath events for the case study. Derived ULF wave activity from GOES and RBSP measurements and chorus wave activity from the POES data based proxy. Developed and coded the method to compute PSD from RBSP data. The development was done partly under the supervision

of Assoc. Prof. Allison Jaynes during a research visit to the University of Iowa. Performed the data analysis and produced the figures. Interpreted the results and wrote the manuscript with contributions from co-authors. Presented the results in international scientific conferences.

7.3 Paper III

Kalliokoski M. M. H., Henderson M. G., Morley S. K., Kilpua E. K. J., Osmane A., Olifer L., Turner D. L., Jaynes A. N., George H., Hoilijoki S., Turc L., Palmroth M. (2022), Outer radiation belt flux and phase space density response to sheath regions: Van Allen Probes and GPS observations, *Journal of Geophysical Research: Space Physics*, preprint: doi:10.1002/essoar.10511548.1.

Summary: A reproduction of the comprehensive statistical analysis of the response of outer radiation belt electron fluxes to ICME-driven sheath regions analysed in Paper I but using GPS data to achieve a higher time resolution. The analysis was also repeated for PSD in addition to the flux in order to study the physical processes governing the electron dynamics during sheaths. The study shows the good inter-calibration between RBSP and GPS measurements as the response calculated from GPS data reproduces the energy- and L-dependent features in the RBSP response. Additionally, high data density GPS data enables employing a 30-minute timescale in the analysis, which confirms that those features in the response are specifically caused by the sheath region. This immediate sheath response also indicates depletion to be more commonly caused by sheaths, and that the outer belt electron fluxes are replenished during the early ejecta. Response analysis of PSD reveals that permanent loss from the radiation belt system is commonly caused by all sheaths, but that only geoeffective sheaths can effectively accelerate outer belt electrons.

The author's contribution: Developed and coded the method to compute PSD from GPS data. Performed the data analysis and produced the figures. The analysis was done partly under the supervision of Dr. Michael Henderson and Dr. Steven Morley during the Los Alamos Space Weather Summer School held by the Los Alamos National Laboratory. Interpreted the results and wrote the manuscript with contributions from co-authors. Presented the results in international scientific conferences.

Bibliography

Ala-Lahti, M., Dimmock, A. P., Pulkkinen, T. I., Good, S. W., Yordanova, E., Turc, L. and Kilpua, E. K. J., 2021. Transmission of an ICME sheath into the Earth's magnetosheath and the occurrence of traveling foreshocks. *J. Geophys. Res. Space Physics*, 126(12), e29896. doi:10.1029/2021JA029896

Albert, J. M., Selesnick, R. S., Morley, S. K., Henderson, M. G. and Kellerman, A. C., 2018. Calculation of last closed drift shells for the 2013 GEM radiation belt challenge events. *J. Geophys. Res. Space Physics*, 123(11), 9597–9611. doi: 10.1029/2018JA025991

Alves, L. R., Da Silva, L. A., Souza, V. M., Sibeck, D. G., Jauer, P. R., Vieira, L. E. A., Walsh, B. M., Silveira, M. V. D., Marchezi, J. P., Rockenbach, M., Lago, A. D., Mendes, O., Tsurutani, B. T., Koga, D., Kanekal, S. G., Baker, D. N., Wygant, J. R. and Kletzing, C. A., 2016. Outer radiation belt dropout dynamics following the arrival of two interplanetary coronal mass ejections. *Geophys. Res. Lett.*, 43, 978–987. doi:10.1002/2015GL067066

Anderson, B. R., Millan, R. M., Reeves, G. D. and Friedel, R. H. W., 2015. Acceleration and loss of relativistic electrons during small geomagnetic storms. *Geophys. Res. Lett.*, 42(23), 10,113–10,119. doi:10.1002/2015GL066376

Angelopoulos, V., Tsai, E., Bingley, L., Shaffer, C., Turner, D. L., Runov, A., Li, W., Liu, J., Artemyev, A. V., Zhang, X. J., Strangeway, R. J., Wirz, R. E., Shprits, Y. Y., Sergeev, V. A., Caron, R. P., Chung, M., Cruce, P., Greer, W., Grimes, E., Hector, K., Lawson, M. J., Leneman, D., Masongsong, E. V., Russell, C. L., Wilkins, C., Hinkley, D., Blake, J. B., Adair, N., Allen, M., Anderson, M., Arreola-Zamora, M., Artinger, J., Asher, J., Branchevsky, D., Capitelli, M. R., Castro, R., Chao, G., Chung, N., Cliffe, M., Colton, K., Costello, C., Depe, D., Domae, B. W., Eldin, S., Fitzgibbon, L., Flemming, A., Fox, I., Frederick, D. M., Gilbert, A., Gildemeister, A., Gonzalez, A., Hesford, B., Jha, S., Kang, N., King, J., Krieger, R., Lian, K., Mao, J., McKinney, E., Miller, J. P., Norris, A., Nuesca,

M., Palla, A., Park, E. S. Y., Pedersen, C. E., Qu, Z., Rozario, R., Rye, E., Seaton, R., Subramanian, A., Sundin, S. R., Tan, A., Turner, W., Villegas, A. J., Wasden, M., Wing, G., Wong, C., Xie, E., Yamamoto, S., Yap, R., Zarifian, A. and Zhang, G. Y., 2020. The ELFIN Mission. *Space Sci. Rev.*, 216(5), 103. doi:10.1007/s11214-020-00721-7

Aseev, N. A., Shprits, Y. Y., Drozdov, A. Y., Kellerman, A. C., Usanova, M. E., Wang, D. and Zhelavskaya, I. S., 2017. Signatures of ultrarelativistic electron loss in the heart of the outer radiation belt measured by Van Allen Probes. *J. Geophys. Res. Space Physics*, 122(10), 10,102–10,111. doi:10.1002/2017JA024485

Asikainen, T., 2017. Calibrated and corrected POES/MEPED energetic particle observations. In Belehaki, A., Hapgood, M. and Watermann, J., editor, *The ESPAS e-infrastructure: Access to data in near-Earth space*, pages 57–69. EDP Science. doi:10.1051/978-2-7598-1949-2

Asikainen, T. and Mursula, K., 2013. Correcting the NOAA/MEPED energetic electron fluxes for detector efficiency and proton contamination. *J. Geophys. Res. Space Physics*, 118(10), 6500–6510. doi:10.1002/jgra.50584

Baker, D. N., Erickson, P. J., Fennell, J. F., Foster, J. C., Jaynes, A. N. and Verronen, P. T., 2018. Space weather effects in the Earth's radiation belts. *Space Sci. Rev.*, 214(1), 17. doi:10.1007/s11214-017-0452-7

Baker, D. N., Jaynes, A. N., Hoxie, V. C., Thorne, R. M., Foster, J. C., Li, X., Fennell, J. F., Wygant, J. R., Kanekal, S. G., Erickson, P. J., Kurth, W., Li, W., Ma, Q., Schiller, Q., Blum, L., Malaspina, D. M., Gerrard, A. and Lanzerotti, L. J., 2014. An impenetrable barrier to ultrarelativistic electrons in the Van Allen radiation belts. *Nature*, 515(7528), 531–534. doi:10.1038/nature13956

Baker, D. N., Kanekal, S. G., Hoxie, V. C., Batiste, S., Bolton, M., Li, X., Elkington, S. R., Monk, S., Reukauf, R., Steg, S., Westfall, J., Belting, C., Bolton, B., Braun, D., Cervelli, B., Hubbell, K., Kien, M., Knappmiller, S., Wade, S., Lamprecht, B., Stevens, K., Wallace, J., Yehle, A., Spence, H. E. and Friedel, R., 2013a. The Relativistic Electron-Proton Telescope (REPT) instrument on board the Radiation Belt Storm Probes (RBSP) spacecraft: characterization of Earth's radiation belt high-energy particle populations. *Space Sci. Rev.*, 179(1-4), 337–381. doi:10.1007/s11214-012-9950-9

Baker, D. N., Kanekal, S. G., Hoxie, V. C., Henderson, M. G., Li, X., Spence, H. E., Elkington, S. R., Friedel, R. H. W., Goldstein, J., Hudson, M. K., Reeves,

G. D., Thorne, R. M., Kletzing, C. A. and Claudepierre, S. G., 2013b. A long-lived relativistic electron storage ring embedded in Earth's outer Van Allen belt. *Science*, 340(6129), 186–190. doi:10.1126/science.1233518

Baker, D. N., Pulkkinen, T. I., Angelopoulos, V., Baumjohann, W. and McPherron, R. L., 1996. Neutral line model of substorms: Past results and present view. *J. Geophys. Res.*, 101(A6), 12975–13010. doi:10.1029/95JA03753

Bingham, S. T., Mouikis, C. G., Kistler, L. M., Boyd, A. J., Paulson, K., Farrugia, C. J., Huang, C. L., Spence, H. E., Claudepierre, S. G. and Kletzing, C., 2018. The outer radiation belt response to the storm time development of seed electrons and chorus wave activity during CME and CIR driven storms. *J. Geophys. Res. Space Physics*, 123(12), 10,139–10,157. doi:10.1029/2018JA025963

Blake, J. B., Carranza, P. A., Claudepierre, S. G., Clemmons, J. H., Crain, W. R., Dotan, Y., Fennell, J. F., Fuentes, F. H., Galvan, R. M., George, J. S., Henderson, M. G., Lalic, M., Lin, A. Y., Looper, M. D., Mabry, D. J., Mazur, J. E., McCarthy, B., Nguyen, C. Q., O'Brien, T. P., Perez, M. A., Redding, M. T., Roeder, J. L., Salvaggio, D. J., Sorensen, G. A., Spence, H. E., Yi, S. and Zakrzewski, M. P., 2013. The Magnetic Electron Ion Spectrometer (MagEIS) instruments aboard the Radiation Belt Storm Probes (RBSP) spacecraft. *Space Sci. Rev.*, 179(1-4), 383–421. doi:10.1007/s11214-013-9991-8

Blum, L., Kanekal, S., Espley, J., Jaynes, A., Gabrielse, C., Sheppard, D., SChiller, Q. and Turner, D., 2021a. GTOSat: a next-generation cubesat to study Earth's radiation belts. In *43rd COSPAR Scientific Assembly. Held 28 January - 4 February*, volume 43, page 2274

Blum, L. W., Artemyev, A., Agapitov, O., Mourenas, D., Boardsen, S. and Schiller, Q., 2019. EMIC wave-driven bounce resonance scattering of energetic electrons in the inner magnetosphere. *J. Geophys. Res. Space Physics*, 124, 2484–2496. doi:10.1029/2018JA026427

Blum, L. W., Koval, A., Richardson, I. G., Wilson, L. B., Malaspina, D., Greeley, A. and Jaynes, A. N., 2021b. Prompt response of the dayside magnetosphere to discrete structures within the sheath region of a coronal mass ejection. *Geophys. Res. Lett.*, 48(11), e92700. doi:10.1029/2021GL092700

Bortnik, J., Thorne, R. M. and Meredith, N. P., 2008. The unexpected origin of plasmaspheric hiss from discrete chorus emissions. *Nature*, 452(7183), 62–66. doi:10.1038/nature06741

Bourdarie, S., Friedel, R. H. W., Fennell, J., Kanekal, S. and Cayton, T. E., 2005. Radiation belt representation of the energetic electron environment: Model and data synthesis using the Salammbô radiation belt transport code and Los Alamos geosynchronous and GPS energetic particle data. *Space Weather*, 3(4), S04S01. doi:10.1029/2004SW000065

Boyd, A. J., Reeves, G. D., Spence, H. E., Funsten, H. O., Larsen, B. A., Skoug, R. M., Blake, J. B., Fennell, J. F., Claudepierre, S. G., Baker, D. N., Kanekal, S. G. and Jaynes, A. N., 2019. RBSP-ECT combined spin-averaged electron flux data product. *J. Geophys. Res. Space Physics*, 124(11), 9124–9136. doi:10.1029/2019JA026733

Boyd, A. J., Spence, H. E., Claudepierre, S. G., Fennell, J. F., Blake, J. B., Baker, D. N., Reeves, G. D. and Turner, D. L., 2014. Quantifying the radiation belt seed population in the 17 March 2013 electron acceleration event. *Geophys. Res. Lett.*, 41(7), 2275–2281. doi:10.1002/2014GL059626

Boyd, A. J., Spence, H. E., Huang, C. L., Reeves, G. D., Baker, D. N., Turner, D. L., Claudepierre, S. G., Fennell, J. F., Blake, J. B. and Shprits, Y. Y., 2016. Statistical properties of the radiation belt seed population. *J. Geophys. Res. Space Physics*, 121(8), 7636–7646. doi:10.1002/2016JA022652

Boyd, A. J., Turner, D. L., Reeves, G. D., Spence, H. E., Baker, D. N. and Blake, J. B., 2018. What causes radiation belt enhancements: a survey of the Van Allen Probes era. *Geophys. Res. Lett.*, 45(11), 5253–5259. doi:10.1029/2018GL077699

Breneman, A. W., Halford, A., Millan, R., McCarthy, M., Fennell, J., Sample, J., Woodger, L., Hospodarsky, G., Wygant, J. R., Cattell, C. A., Goldstein, J., Malaspina, D. and Kletzing, C. A., 2015. Global-scale coherence modulation of radiation-belt electron loss from plasmaspheric hiss. *Nature*, 523(7559), 193–195. doi:10.1038/nature14515

Burtis, W. J. and Helliwell, R. A., 1969. Banded chorus—A new type of VLF radiation observed in the magnetosphere by OGO 1 and OGO 3. *J. Geophys. Res.*, 74(11), 3002. doi:10.1029/JA074i011p03002

Carver, M., Morley, S. K. and Stricklan, A., 2020. GPS constellation energetic particle measurements. In *2020 IEEE Aerospace Conference*, pages 1–10. doi:10.1109/AERO47225.2020.9172652

Cervantes, S., Shprits, Y. Y., Aseev, N. A., Drozdov, A. Y., Castillo, A. and Stolle, C., 2020. Identifying radiation belt electron source and loss processes by assimilating spacecraft data in a three-dimensional diffusion model. *J. Geophys. Res. Space Physics*, 125(1), e27514. doi:10.1029/2019JA027514

Chen, Y., Friedel, R. H. W., Henderson, M. G., Claudepierre, S. G., Morley, S. K. and Spence, H. E., 2014a. REPAD: An empirical model of pitch angle distributions for energetic electrons in the Earth's outer radiation belt. *J. Geophys. Res. Space Physics*, 119(3), 1693–1708. doi:10.1002/2013JA019431

Chen, Y., Friedel, R. H. W., Reeves, G. D., Onsager, T. G. and Thomsen, M. F., 2005. Multisatellite determination of the relativistic electron phase space density at geosynchronous orbit: Methodology and results during geomagnetically quiet times. *J. Geophys. Res. Space Physics*, 110(A10), A10210. doi:10.1029/2004JA010895

Chen, Y., Reeves, G. D. and Friedel, R. H. W., 2007. The energization of relativistic electrons in the outer Van Allen radiation belt. *Nat. Phys.*, 3(9), 614–617. doi:10.1038/nphys655

Chen, Y., Reeves, G. D., Friedel, R. H. W. and Cunningham, G. S., 2014b. Global time-dependent chorus maps from low-Earth-orbit electron precipitation and Van Allen Probes data. *Geophys. Res. Lett.*, 41(3), 755–761. doi:10.1002/2013GL059181

Chen, Y., Reeves, G. D., Fu, X. and Henderson, M., 2019. PreMevE: New predictive model for megaelectron-volt electrons inside Earth's outer radiation belt. *Space Weather*, 17(3), 438–454. doi:10.1029/2018SW002095

Claudepierre, S. G., Elkington, S. R. and Wiltberger, M., 2008. Solar wind driving of magnetospheric ULF waves: Pulsations driven by velocity shear at the magnetopause. *J. Geophys. Res. Space Physics*, 113(A5), A05218. doi:10.1029/2007JA012890

Claudepierre, S. G., Hudson, M. K., Lotko, W., Lyon, J. G. and Denton, R. E., 2010. Solar wind driving of magnetospheric ULF waves: Field line resonances driven by dynamic pressure fluctuations. *J. Geophys. Res. Space Physics*, 115(A11), A11202. doi:10.1029/2010JA015399

Claudepierre, S. G., O'Brien, T. P., Blake, J. B., Fennell, J. F., Roeder, J. L., Clemmons, J. H., Looper, M. D., Mazur, J. E., Mulligan, T. M., Spence, H. E.,

Reeves, G. D., Friedel, R. H. W., Henderson, M. G. and Larsen, B. A., 2015. A background correction algorithm for Van Allen Probes MagEIS electron flux measurements. *J. Geophys. Res. Space Physics*, 120(7), 5703–5727. doi:10.1002/2015JA021171

Claudepierre, S. G., O'Brien, T. P., Looper, M. D., Blake, J. B., Fennell, J. F., Roeder, J. L., Clemmons, J. H., Mazur, J. E., Turner, D. L., Reeves, G. D. and Spence, H. E., 2019. A revised look at relativistic electrons in the Earth's inner radiation zone and slot region. *J. Geophys. Res. Space Physics*, 124(2), 934–951. doi:10.1029/2018JA026349

Cohen, I. J., Turner, D. L., Michael, A. T., Sorathia, K. A. and Ukhorskiy, A. Y., 2021. Investigating the link between outer radiation belt losses and energetic electron escape at the magnetopause: a case study using multi-mission observations and simulations. *J. Geophys. Res. Space Physics*, 126(6), e2021JA029261. doi:10.1029/2021JA029261

Da Silva, L. A., Shi, J., Alves, L. R., Sibeck, D., Souza, V. M., Marchezi, J. P., Medeiros, C., Vieira, L. E. A., Agapitov, O., Jauer, P. R., Alves, M. E. S., Wang, C., Li, H., Liu, Z., Dal Lago, A., Alves, M. V., Rockenbach, M. S., Baker, D. N., Zhang, S. Y. and Kanekal, S. G., 2020. Dynamic mechanisms associated with high-energy electron flux dropout in the Earth's outer radiation belt under the influence of a coronal mass ejection sheath region. *J. Geophys. Res. Space Physics*, 126(1), e2020JA028492. doi:10.1029/2020JA028492

Daglis, I. A., Thorne, R. M., Baumjohann, W. and Orsini, S., 1999. The terrestrial ring current: Origin, formation, and decay. *Rev. Geophys.*, 37(4), 407–438. doi:10.1029/1999RG900009

Drozdov, A. Y., Aseev, N., Effenberger, F., Turner, D. L., Saikin, A. and Shprits, Y. Y., 2019. Storm time depletions of multi-MeV radiation belt electrons observed at different pitch angles. *J. Geophys. Res. Space Physics*, 124(11), 8943–8953. doi:10.1029/2019JA027332

Drozdov, A. Y., Usanova, M. E., Hudson, M. K., Allison, H. J. and Shprits, Y. Y., 2020. The role of hiss, chorus, and EMIC waves in the modeling of the dynamics of the multi-MeV radiation belt electrons. *J. Geophys. Res. Space Physics*, 125(9), e28282. doi:10.1029/2020JA028282

Engebretson, M. J., Lessard, M. R., Bortnik, J., Green, J. C., Horne, R. B., Detrick, D. L., Weatherwax, A. T., Manninen, J., Petit, N. J., Posch, J. L. and Rose,

M. C., 2008. Pc1-Pc2 waves and energetic particle precipitation during and after magnetic storms: Superposed epoch analysis and case studies. *J. Geophys. Res. Space Physics*, 113(A1), A01211. doi:10.1029/2007JA012362

Engebretson, M. J., Posch, J. L., Braun, D. J., Li, W., Ma, Q., Kellerman, A. C., Huang, C. L., Kanekal, S. G., Kletzing, C. A., Wygant, J. R., Spence, H. E., Baker, D. N., Fennell, J. F., Angelopoulos, V., Singer, H. J., Lessard, M. R., Horne, R. B., Raita, T., Shiokawa, K., Rakhmatulin, R., Dmitriev, E. and Ermakova, E., 2018. EMIC wave events during the four GEM QARBM challenge intervals. *J. Geophys. Res. Space Physics*, 123(8), 6394–6423. doi:10.1029/2018JA025505

Evans, D. S. and Greer, M. S., 2004. Polar orbiting environmental satellite space environment monitor – 2: Instrument descriptions and archive data documentation. Technical Report version 1.4, Space Environment Center, Boulder, Colorado

Fälthammar, C.-G., 1965. Effects of time-dependent electric fields on geomagnetically trapped radiation. *J. Geophys. Res.*, 70(11), 2503–2516. doi:10.1029/JZ070i011p02503

Fennell, J. F., Claudepierre, S. G., Blake, J. B., O'Brien, T. P., Clemmons, J. H., Baker, D. N., Spence, H. E. and Reeves, G. D., 2015. Van Allen Probes show that the inner radiation zone contains no MeV electrons: ECT/MagEIS data. *Geophys. Res. Lett.*, 42(5), 1283–1289. doi:10.1002/2014GL062874

Finlay, C. C., Maus, S., Beggan, C. D., Bondar, T. N., Chambodut, A., Chernova, T. A., Chulliat, A., Golovkov, V. P., Hamilton, B., Hamoudi, M., Holme, R., Hulot, G., Kuang, W., Langlais, B., Lesur, V., Lowes, F. J., Lühr, H., MacMillan, S., Mandea, M., McLean, S., Manoj, C., Menvielle, M., Michaelis, I., Olsen, N., Rauberg, J., Rother, M., Sabaka, T. J., Tangborn, A., Tøffner-Clausen, L., Thébault, E., Thomson, A. W. P., Wardinski, I., Wei, Z. and Zvereva, T. I., 2010. International Geomagnetic Reference Field: the eleventh generation. *Geophys. J. Int.*, 183(3), 1216–1230. doi:10.1111/j.1365-246X.2010.04804.x

Forsyth, C., Rae, I. J., Murphy, K. R., Freeman, M. P., Huang, C. L., Spence, H. E., Boyd, A. J., Coxon, J. C., Jackman, C. M., Kalmoni, N. M. E. and Watt, C. E. J., 2016. What effect do substorms have on the content of the radiation belts? *J. Geophys. Res. Space Physics*, 121(7), 6292–6306. doi:10.1002/2016JA022620

Foster, J. C., Erickson, P. J., Omura, Y., Baker, D. N., Kletzing, C. A. and Claudepierre, S. G., 2017. Van Allen Probes observations of prompt MeV radiation belt

electron acceleration in nonlinear interactions with VLF chorus. *J. Geophys. Res. Space Physics*, 122(1), 324–339. doi:10.1002/2016JA023429

Georgiou, M., Daglis, I. A., Rae, I. J., Zesta, E., Sibeck, D. G., Mann, I. R., Balasis, G. and Tsinganos, K., 2018. Ultralow frequency waves as an intermediary for solar wind energy input into the radiation belts. *J. Geophys. Res. Space Physics*, 123(12), 10,090–10,108. doi:10.1029/2018JA025355

Gold, T., 1959. Motions in the magnetosphere of the Earth. *J. Geophys. Res.*, 64(9), 1219–1224. doi:10.1029/JZ064i009p01219

Gonzalez, W. D., Joselyn, J. A., Kamide, Y., Kroehl, H. W., Rostoker, G., Tsurutani, B. T. and Vasyliunas, V. M., 1994. What is a geomagnetic storm? *J. Geophys. Res.*, 99(A4), 5771–5792. doi:10.1029/93JA02867

Green, J. C., 2006. Using electron phase space density signatures to identify the electromagnetic waves responsible for accelerating relativistic electrons in Earth's magnetosphere. In *Magnetospheric ULF Waves: Synthesis and New Directions*, volume 169, page 225. doi:10.1029/169GM15

Green, J. C. and Kivelson, M. G., 2004. Relativistic electrons in the outer radiation belt: Differentiating between acceleration mechanisms. *J. Geophys. Res. Space Physics*, 109(A3), A03213. doi:10.1029/2003JA010153

Haines, C., Owens, M. J., Barnard, L., Lockwood, M. and Ruffenach, A., 2019. The variation of geomagnetic storm duration with intensity. *Solar Phys.*, 294(11), 154. doi:10.1007/s11207-019-1546-z

Hartley, D. P. and Denton, M. H., 2014. Solving the radiation belt riddle. *Astronomy and Geophysics*, 55(6), 6.17–6.20. doi:10.1093/astrogeo/atu247

Henderson, M., Morley, S., Niehof, J. and Larsen, B., 2018. drsteve/LANLGeoMag: v1.5.16. doi:10.5281/zenodo.1195041

Hendry, A. T., Santolik, O., Kletzing, C. A., Rodger, C. J., Shiokawa, K. and Baishev, D., 2019. Multi-instrument observation of nonlinear EMIC-driven electron precipitation at sub-MeV energies. *Geophys. Res. Lett.*, 46(13), 7248–7257. doi:10.1029/2019GL082401

Hess, W. N., 1968. *The Radiation Belt and Magnetosphere*. Blaisdell Publishing Company. p. 65

Hietala, H., Kilpua, E. K. J., Turner, D. L. and Angelopoulos, V., 2014. Depleting effects of ICME-driven sheath regions on the outer electron radiation belt. *Geophys. Res. Lett.*, 41(7), 2258–2265. doi:10.1002/2014GL059551

Hilmer, R. V., Ginet, G. P. and Cayton, T. E., 2000. Enhancement of equatorial energetic electron fluxes near L=4.2 as a result of high speed solar wind streams. *J. Geophys. Res.*, 105(A10), 23311–23322. doi:10.1029/1999JA000380

Horne, R. B., Thorne, R. M., Shprits, Y. Y., Meredith, N. P., Glauert, S. A., Smith, A. J., Kanekal, S. G., Baker, D. N., Engebretson, M. J., Posch, J. L., Spasojevic, M., Inan, U. S., Pickett, J. S. and Decreau, P. M. E., 2005. Wave acceleration of electrons in the Van Allen radiation belts. *Nature*, 437(7056), 227–230. doi:10.1038/nature03939

Hsieh, Y.-K., Kubota, Y. and Omura, Y., 2020. Nonlinear evolution of radiation belt electron fluxes interacting with oblique whistler mode chorus emissions. *J. Geophys. Res. Space Physics*, 125(2), e27465. doi:10.1029/2019JA027465

Huttunen, K. and Koskinen, H., 2004. Importance of post-shock streams and sheath region as drivers of intense magnetospheric storms and high-latitude activity. *Ann. Geophys.*, 22(5), 1729–1738. doi:10.5194/angeo-22-1729-2004

Iyemori, T., 1990. Storm-time magnetospheric currents inferred from mid-latitude geomagnetic field variations. *J. Geomag. Geoelec.*, 42(11), 1249–1265. doi:10.5636/jgg.42.1249

Jacobs, J. A., Kato, Y., Matsushita, S. and Troitskaya, V. A., 1964. Classification of geomagnetic micropulsations. *J. Geophys. Res.*, 69(1), 180–181. doi:10.1029/JZ069i001p00180

Jaynes, A. N., Baker, D. N., Singer, H. J., Rodriguez, J. V., Loto'aniu, T. M., Ali, A. F., Elkington, S. R., Li, X., Kanekal, S. G., Fennell, J. F., Li, W., Thorne, R. M., Kletzing, C. A., Spence, H. E. and Reeves, G. D., 2015. Source and seed populations for relativistic electrons: Their roles in radiation belt changes. *J. Geophys. Res. Space Physics*, 120(9), 7240–7254. doi:10.1002/2015JA021234

Jaynes, A. N., Li, X., Schiller, Q. G., Blum, L. W., Tu, W., Turner, D. L., Ni, B., Bortnik, J., Baker, D. N., Kanekal, S. G., Blake, J. B. and Wygant, J., 2014. Evolution of relativistic outer belt electrons during an extended quiescent period. *J. Geophys. Res. Space Physics*, 119(12), 9558–9566. doi:10.1002/2014JA020125

Kalliokoski, M. M. H., Henderson, M. G., Morley, S. K., Kilpua, E. K. J., Osmane, A., Olifer, L., Turner, D. L., Jaynes, A. N., George, H., Hoilijoki, S., Turc, L. and Palmroth, M., 2022a. Outer radiation belt flux and phase space density response to sheath regions: Van Allen Probes and GPS observations. *J. Geophys. Res. Space Physics*. Preprint, doi:0.1002/essoar.10511548.1

Kalliokoski, M. M. H., Kilpua, E. K. J., Osmane, A., Jaynes, A. N., Turner, D. L., George, H., Turc, L. and Palmroth, M., 2022b. Phase space density analysis of outer radiation belt electron energization and loss during geoeffective and nongeoeffective sheath regions. *J. Geophys. Res. Space Physics*, 127(3), e2021JA029662. doi:10.1029/2021JA029662

Kalliokoski, M. M. H., Kilpua, E. K. J., Osmane, A., Turner, D. L., Jaynes, A. N., Turc, L., George, H. and Palmroth, M., 2020. Outer radiation belt and inner magnetospheric response to sheath regions of coronal mass ejections: a statistical analysis. *Ann. Geophys.*, 38(3), 683–701. doi:10.5194/angeo-38-683-2020

Kanekal, S. G., Baker, D. N., Henderson, M. G., Li, W., Fennell, J. F., Zheng, Y., Richardson, I. G., Jones, A., Ali, A. F., Elkington, S. R., Jaynes, A., Li, X., Blake, J. B., Reeves, G. D., Spence, H. E. and Kletzing, C. A., 2015. Relativistic electron response to the combined magnetospheric impact of a coronal mass ejection overlapping with a high-speed stream: Van Allen Probes observations. *J. Geophys. Res. Space Physics*, 120(9), 7629–7641. doi:10.1002/2015JA021395

Kataoka, R. and Miyoshi, Y., 2006. Flux enhancement of radiation belt electrons during geomagnetic storms driven by coronal mass ejections and corotating interaction regions. *Space Weather*, 4(9), 09004. doi:10.1029/2005SW000211

Katsavrias, C., Daglis, I. A., Turner, D. L., Sand berg, I., Papadimitriou, C., Georgiou, M. and Balasis, G., 2015. Nonstorm loss of relativistic electrons in the outer radiation belt. *Geophys. Res. Lett.*, 42(24), 10,521–10,530. doi:10.1002/2015GL066773

Kepko, L. and Spence, H. E., 2003. Observations of discrete, global magnetospheric oscillations directly driven by solar wind density variations. *J. Geophys. Res. Space Physics*, 108(A6), 1257. doi:10.1029/2002JA009676

Kilpua, E. K. J., Balogh, A., von Steiger, R. and Liu, Y. D., 2017a. Geoeffective properties of solar transients and stream interaction regions. *Space Sci. Rev.*, 212, 1271–1314. doi:10.1007/s11214-017-0411-3

Kilpua, E. K. J., Fontaine, D., Moissard, C., Ala-Lahti, M., Palmerio, E., Yordanova, E., Good, S. W., Kalliokoski, M. M. H., Lumme, E., Osmane, A., Palmroth, M. and Turc, L., 2019. Solar wind properties and geospace impact of coronal mass ejection-driven sheath regions: Variation and driver dependence. *Space Weather*, 17(0). doi:10.1029/2019SW002217

Kilpua, E. K. J., Hietala, H., Koskinen, H. E. J., Fontaine, D. and Turc, L., 2013. Magnetic field and dynamic pressure ULF fluctuations in coronal-mass-ejection-driven sheath regions. *Ann. Geophys.*, 31(9), 1559–1567. doi:10.5194/angeo-31-1559-2013

Kilpua, E. K. J., Hietala, H., Turner, D. L., Koskinen, H. E. J., Pulkkinen, T. I., Rodriguez, J. V., Reeves, G. D., Claudepierre, S. G. and Spence, H. E., 2015. Unraveling the drivers of the storm time radiation belt response. *Geophys. Res. Lett.*, 42(9), 3076–3084. doi:10.1002/2015GL063542

Kilpua, E. K. J., Koskinen, H. E. J. and Pulkkinen, T. I., 2017b. Coronal mass ejections and their sheath regions in interplanetary space. *Living Rev. Sol. Phys.*, 14(1), 5. doi:10.1007/s41116-017-0009-6

Kim, H.-J. and Chan, A. A., 1997. Fully adiabatic changes in storm time relativistic electron fluxes. *J. Geophys. Res.*, 102(A10), 22107–22116. doi:10.1029/97JA01814

Kim, H. J., Lee, D. Y., Wolf, R., Bortnik, J., Kim, K. C., Lyons, L., Choe, W., Noh, S. J., Choi, K. E., Yue, C. and Li, J., 2021. Rapid injections of MeV electrons and extremely fast step like outer radiation belt enhancements. *Geophys. Res. Lett.*, 48(9), e93151. doi:10.1029/2021GL093151

Kim, K. C., Lee, D. Y., Kim, H. J., Lee, E. S. and Choi, C. R., 2010. Numerical estimates of drift loss and Dst effect for outer radiation belt relativistic electrons with arbitrary pitch angle. *J. Geophys. Res. Space Physics*, 115(A3), A03208. doi:10.1029/2009JA014523

Kletzing, C. A., Kurth, W. S., Acuna, M., MacDowall, R. J., Torbert, R. B., Averkamp, T., Bodet, D., Bounds, S. R., Chutter, M., Connerney, J., Crawford, D., Dolan, J. S., Dvorsky, R., Hospodarsky, G. B., Howard, J., Jordanova, V., Johnson, R. A., Kirchner, D. L., Mokrzycki, B., Needell, G., Odom, J., Mark, D., Pfaff, R., Phillips, J. R., Piker, C. W., Remington, S. L., Rowland , D., Santolik, O., Schnurr, R., Sheppard, D., Smith, C. W., Thorne, R. M. and Tyler, J., 2013. The Electric and Magnetic Field Instrument Suite and Integrated Science (EMFISIS) on RBSP. *Space Sci. Rev.*, 179(1-4), 127–181. doi:10.1007/s11214-013-9993-6

Koons, H. C. and Roeder, J. L., 1990. A survey of equatorial magnetospheric wave activity between 5 and 8 R_E. *Planet. Space Sci.*, 38(10), 1335–1341. doi:10.1016/0032-0633(90)90136-E

Koskinen, H. E. J., 2011. *Physics of Space Storms*. Springer. doi:10.1007/978-3-642-00319-6

Koskinen, H. E. J. and Kilpua, E. K. J., 2022. *Physics of Earth's Radiation Belts: Theory and Observations*. Springer. doi:10.1007/978-3-030-82167-8

Kurita, S., Miyoshi, Y., Shiokawa, K., Higashio, N., Mitani, T., Takashima, T., Matsuoka, A., Shinohara, I., Kletzing, C. A., Blake, J. B., Claudepierre, S. G., Connors, M., Oyama, S., Nagatsuma, T., Sakaguchi, K., Baishev, D. and Otsuka, Y., 2018. Rapid loss of relativistic electrons by EMIC waves in the outer radiation belt observed by Arase, Van Allen Probes, and the PWING ground stations. *Geophys. Res. Lett.*, 45(23), 12,720–12,729. doi:10.1029/2018GL080262

Kurth, W. S., De Pascuale, S., Faden, J. B., Kletzing, C. A., Hospodarsky, G. B., Thaller, S. and Wygant, J. R., 2015. Electron densities inferred from plasma wave spectra obtained by the Waves instrument on Van Allen Probes. *J. Geophys. Res. Space Physics*, 120(2), 904–914. doi:10.1002/2014JA020857

Lam, M. M., Horne, R. B., Meredith, N. P., Glauert, S. A., Moffat-Griffin, T. and Green, J. C., 2010. Origin of energetic electron precipitation >30 keV into the atmosphere. *J. Geophys. Res. Space Physics*, 115(8), A00F08. doi:10.1029/2009JA014619

Lejosne, S. and Kollmann, P., 2020. Radiation belt radial diffusion at Earth and beyond. *Space Sci. Rev.*, 216(1), 19. doi:10.1007/s11214-020-0642-6

Lepping, R. P., Acũna, M. H., Burlaga, L. F., Farrell, W. M., Slavin, J. A., Schatten, K. H., Mariani, F., Ness, N. F., Neubauer, F. M., Whang, Y. C., Byrnes, J. B., Kennon, R. S., Panetta, P. V., Scheifele, J. and Worley, E. M., 1995. The Wind Magnetic Field Investigation. *Space Sci. Rev.*, 71, 207–229. doi:10.1007/BF00751330

Li, J., Bortnik, J., An, X., Li, W., Angelopoulos, V., Thorne, R. M., Russell, C. T., Ni, B., Shen, X., Kurth, W. S., Hospodarsky, G. B., Hartley, D. P., Funsten, H. O., Spence, H. E. and Baker, D. N., 2019. Origin of two-band chorus in the radiation belt of Earth. *Nat. Commun.*, 10, 4672. doi:10.1038/s41467-019-12561-3

Li, W., Ma, Q., Thorne, R. M., Bortnik, J., Zhang, X. J., Li, J., Baker, D. N., Reeves, G. D., Spence, H. E., Kletzing, C. A., Kurth, W. S., Hospodarsky, G. B., Blake, J. B., Fennell, J. F., Kanekal, S. G., Angelopoulos, V., Green, J. C. and Goldstein, J., 2016a. Radiation belt electron acceleration during the 17 March 2015 geomagnetic storm: Observations and simulations. *J. Geophys. Res. Space Physics*, 121(6), 5520–5536. doi:10.1002/2016JA022400

Li, W., Ni, B., Thorne, R. M., Bortnik, J., Green, J. C., Kletzing, C. A., Kurth, W. S. and Hospodarsky, G. B., 2013a. Constructing the global distribution of chorus wave intensity using measurements of electrons by the POES satellites and waves by the Van Allen Probes. *Geophys. Res. Lett.*, 40(17), 4526–4532. doi:10.1002/grl.50920

Li, W., Santolik, O., Bortnik, J., Thorne, R. M., Kletzing, C. A., Kurth, W. S. and Hospodarsky, G. B., 2016b. New chorus wave properties near the equator from Van Allen Probes wave observations. *Geophys. Res. Lett.*, 43(10), 4725–4735. doi:10.1002/2016GL068780

Li, W., Thorne, R. M., Bortnik, J., Baker, D. N., Reeves, G. D., Kanekal, S. G., Spence, H. E. and Green, J. C., 2015a. Solar wind conditions leading to efficient radiation belt electron acceleration: A superposed epoch analysis. *Geophys. Res. Lett.*, 42(17), 6906–6915. doi:10.1002/2015GL065342

Li, W., Thorne, R. M., Ma, Q., Ni, B., Bortnik, J., Baker, D. N., Spence, H. E., Reeves, G. D., Kanekal, S. G., Green, J. C., Kletzing, C. A., Kurth, W. S., Hospodarsky, G. B., Blake, J. B., Fennell, J. F. and Claudepierre, S. G., 2014. Radiation belt electron acceleration by chorus waves during the 17 March 2013 storm. *J. Geophys. Res. Space Physics*, 119(6), 4681–4693. doi:10.1002/2014JA019945

Li, X., Schiller, Q., Blum, L., Califf, S., Zhao, H., Tu, W., Turner, D. L., Gerhardt, D., Palo, S., Kanekal, S., Baker, D. N., Fennell, J., Blake, J. B., Looper, M., Reeves, G. D. and Spence, H., 2013b. First results from CSSWE CubeSat: Characteristics of relativistic electrons in the near-Earth environment during the October 2012 magnetic storms. *J. Geophys. Res. Space Physics*, 118(10), 6489–6499. doi:10.1002/2013JA019342

Li, X., Selesnick, R. S., Baker, D. N., Jaynes, A. N., Kanekal, S. G., Schiller, Q., Blum, L., Fennell, J. and Blake, J. B., 2015b. Upper limit on the inner radiation belt MeV electron intensity. *J. Geophys. Res. Space Physics*, 120(2), 1215–1228. doi:10.1002/2014JA020777

Lugaz, N., Farrugia, C. J., Winslow, R. M., Al-Haddad, N., Kilpua, E. K. J. and Riley, P., 2016. Factors affecting the geoeffectiveness of shocks and sheaths at 1 AU. *J. Geophys. Res. Space Physics*, 121(11), 10,861–10,879. doi:10.1002/2016JA023100

Mann, I. R., Ozeke, L. G., Morley, S. K., Murphy, K. R., Claudepierre, S. G., Turner, D. L., Baker, D. N., Rae, I. J., Kale, A., Milling, D. K., Boyd, A. J., Spence, H. E., Singer, H. J., Dimitrakoudis, S., Daglis, I. A. and Honary, F., 2018. Reply to 'The dynamics of Van Allen belts revisited'. *Nat. Phys.*, 14(2), 103–104. doi:10.1038/nphys4351

Masías-Meza, J. J., Dasso, S., Démoulin, P., Rodriguez, L. and Janvier, M., 2016. Superposed epoch study of ICME sub-structures near Earth and their effects on galactic cosmic rays. *Astron. Astrophys.*, 592, A118. doi:10.1051/0004-6361/201628571

Mauk, B. H., Fox, N. J., Kanekal, S. G., Kessel, R. L., Sibeck, D. G. and Ukhorskiy, A., 2013. Science objectives and rationale for the Radiation Belt Storm Probes mission. *Space Sci. Rev.*, 179(1-4), 3–27. doi:10.1007/s11214-012-9908-y

McIlwain, C. E., 1961. Coordinates for mapping the distribution of magnetically trapped particles. *J. Geophys. Res.*, 66(11), 3681–3691. doi:10.1029/JZ066i011p03681

Meredith, N. P., Horne, R. B., Glauert, S. A., Thorne, R. M., Summers, D., Albert, J. M. and Anderson, R. R., 2006. Energetic outer zone electron loss timescales during low geomagnetic activity. *J. Geophys. Res. Space Physics*, 111(A5), A05212. doi:10.1029/2005JA011516

Miyoshi, Y., Kataoka, R., Kasahara, Y., Kumamoto, A., Nagai, T. and Thomsen, M. F., 2013. High-speed solar wind with southward interplanetary magnetic field causes relativistic electron flux enhancement of the outer radiation belt via enhanced condition of whistler waves. *Geophys. Res. Lett.*, 40(17), 4520–4525. doi:10.1002/grl.50916

Morlet, J., Arens, G., Forgeau, I. and Giard, D., 1982. Wave propagation and sampling theory. *Geophysics*, 47, 203–236. doi:10.1190/1.1441328

Morley, S. K., Friedel, R. H. W., Cayton, T. E. and Noveroske, E., 2010. A rapid, global and prolonged electron radiation belt dropout observed with the Global

Positioning System constellation. *Geophys. Res. Lett.*, 37(6), L06102. doi:10.1029/2010GL042772

Morley, S. K., Henderson, M. G., Reeves, G. D., Friedel, R. H. W. and Baker, D. N., 2013. Phase space density matching of relativistic electrons using the Van Allen Probes: REPT results. *Geophys. Res. Lett.*, 40(18), 4798–4802. doi:10.1002/grl.50909

Morley, S. K., Sullivan, J. P., Carver, M. R., Kippen, R. M., Friedel, R. H. W., Reeves, G. D. and Henderson, M. G., 2017. Energetic particle data from the Global Positioning System constellation. *Space Weather*, 15(2), 283–289. doi:10.1002/2017SW001604

Morley, S. K., Sullivan, J. P., Henderson, M. G., Blake, J. B. and Baker, D. N., 2016. The Global Positioning System constellation as a space weather monitor: Comparison of electron measurements with Van Allen Probes data. *Space Weather*, 14(2), 76–92. doi:10.1002/2015SW001339

Ni, B., Li, W., Thorne, R. M., Bortnik, J., Green, J. C., Kletzing, C. A., Kurth, W. S., Hospodarsky, G. B. and Soria-Santacruz Pich, M., 2014. A novel technique to construct the global distribution of whistler mode chorus wave intensity using low-altitude POES electron data. *J. Geophys. Res. Space Physics*, 119(7), 5685–5699. doi:10.1002/2014JA019935

O'Brien, T. P., McPherron, R. L., Sornette, D., Reeves, G. D., Friedel, R. and Singer, H. J., 2001. Which magnetic storms produce relativistic electrons at geosynchronous orbit? *J. Geophys. Res.*, 106(A8), 15533–15544. doi:10.1029/2001JA000052

O'Brien, T. P. and Moldwin, M. B., 2003. Empirical plasmapause models from magnetic indices. *Geophys. Res. Lett.*, 30(4), 1152. doi:10.1029/2002GL016007

Ogilvie, K. W., Chornay, D. J., Fritzenreiter, R. J., Hunsaker, F., Keller, J., Lobell, J., Miller, G., Scudder, J. D., Sittler, E. C., Jr., Torbert, R. B., Bodet, D., Needell, G., Lazarus, A. J., Steinberg, J. T., Tappan, J. H., Mavretic, A. and Gergin, E., 1995. SWE, A comprehensive plasma instrument for the Wind spacecraft. *Space Sci. Rev.*, 71, 55–77. doi:10.1007/BF00751326

Olifer, L., Mann, I. R., Morley, S. K., Ozeke, L. G. and Choi, D., 2018. On the role of last closed drift shell dynamics in driving fast losses and Van Allen radiation

belt extinction. *J. Geophys. Res. Space Physics*, 123(5), 3692–3703. doi:10.1029/2018JA025190

Olifer, L., Mann, I. R., Ozeke, L. G., Morley, S. K. and Louis, H. L., 2021. On the formation of phantom electron phase space density peaks in single spacecraft radiation belt data. *Geophys. Res. Lett.*, 48(11), e92351. doi:10.1029/2020GL092351

Osmane, A., Savola, M., Kilpua, E., Koskinen, H., Borovsky, J. E. and Kalliokoski, M., 2022. Quantifying the non-linear dependence of energetic electron fluxes in the Earth's radiation belts with radial diffusion drivers. *Ann. Geophys.*, 40(1), 37–53. doi:10.5194/angeo-40-37-2022

Palmerio, E., Kilpua, E. K. J. and Savani, N. P., 2016. Planar magnetic structures in coronal mass ejection-driven sheath regions. *Ann. Geophys.*, 34(2), 313–322. doi:10.5194/angeo-34-313-2016

Palmroth, M., Praks, J., Vainio, R., Janhunen, P., Kilpua, E. K. J., Ganushkina, N. Y., Afanasiev, A., Ala-Lahti, M., Alho, A., Asikainen, T., Asvestari, E., Battarbee, M., Binios, A., Bosser, A., Brito, T., Envall, J., Ganse, U., George, H., Gieseler, J., Good, S., Grand in, M., Haslam, S., Hedman, H. P., Hietala, H., Jovanovic, N., Kakakhel, S., Kalliokoski, M., Kettunen, V. V., Koskela, T., Lumme, E., Meskanen, M., Morosan, D., Rizwan Mughal, M., Niemelä, P., Nyman, S., Oleynik, P., Osmane, A., Palmerio, E., Pfau-Kempf, Y., Peltonen, J., Plosila, J., Polkko, J., Poluianov, S., Pomoell, J., Price, D., Punkkinen, A., Punkkinen, R., Riwanto, B., Salomaa, L., Slavinskis, A., Säntti, T., Tammi, J., Tenhunen, H., Toivanen, P., Tuominen, J., Turc, L., Valtonen, E., Virtanen, P. and Westerlund, T., 2019. FORESAIL-1 cubesat mission to measure radiation belt losses and demonstrate deorbiting. *J. Geophys. Res. Space Physics*, 124. doi:10.1029/2018JA026354

Partamies, N., Juusola, L., Tanskanen, E. and Kauristie, K., 2013. Statistical properties of substorms during different storm and solar cycle phases. *Ann. Geophys.*, 31(2), 349–358. doi:10.5194/angeo-31-349-2013

Pickett, J. S., Grison, B., Omura, Y., Engebretson, M. J., Dandouras, I., Masson, A., Adrian, M. L., Santolík, O., Décréau, P. M. E., Cornilleau-Wehrlin, N. and Constantinescu, D., 2010. Cluster observations of EMIC triggered emissions in association with Pc1 waves near Earth's plasmapause. *Geophys. Res. Lett.*, 37(9), L09104. doi:10.1029/2010GL042648

Pulkkinen, T., 2007. Space weather: terrestrial perspective. *Living Rev. Sol. Phys.*, 4(1), 1. doi:10.12942/lrsp-2007-1

Pulkkinen, T. I., Partamies, N., Huttunen, K. E. J., Reeves, G. D. and Koskinen, H. E. J., 2007. Differences in geomagnetic storms driven by magnetic clouds and ICME sheath regions. *Geophys. Res. Lett.*, 34(2), L02105. doi:10.1029/2006GL027775

Reeves, G. D., Friedel, R. H. W., Larsen, B. A., Skoug, R. M., Funsten, H. O., Claudepierre, S. G., Fennell, J. F., Turner, D. L., Denton, M. H., Spence, H. E., Blake, J. B. and Baker, D. N., 2016. Energy-dependent dynamics of keV to MeV electrons in the inner zone, outer zone, and slot regions. *J. Geophys. Res. Space Physics*, 121(1), 397–412. doi:10.1002/2015JA021569

Reeves, G. D., McAdams, K. L., Friedel, R. H. W. and O'Brien, T. P., 2003. Acceleration and loss of relativistic electrons during geomagnetic storms. *Geophys. Res. Lett.*, 30(10), 1529. doi:10.1029/2002GL016513

Reeves, G. D., Spence, H. E., Henderson, M. G., Morley, S. K., Friedel, R. H. W., Funsten, H. O., Baker, D. N., Kanekal, S. G., Blake, J. B., Fennell, J. F., Claudepierre, S. G., Thorne, R. M., Turner, D. L., Kletzing, C. A., Kurth, W. S., Larsen, B. A. and Niehof, J. T., 2013. Electron acceleration in the heart of the Van Allen radiation belts. *Science*, 341(6149), 991–994. doi:10.1126/science.1237743

Richardson, I. G. and Cane, H. V., 2010. Near-Earth interplanetary coronal mass ejections during solar cycle 23 (1996 - 2009): catalog and summary of properties. *Solar Phys.*, 264(1), 189–237. doi:10.1007/s11207-010-9568-6

Rodger, C. J., Carson, B. R., Cummer, S. A., Gamble, R. J., Clilverd, M. A., Green, J. C., Sauvaud, J.-A., Parrot, M. and Berthelier, J.-J., 2010. Contrasting the efficiency of radiation belt losses caused by ducted and nonducted whistler-mode waves from ground-based transmitters. *J. Geophys. Res. Space Physics*, 115(A12), A12208. doi:10.1029/2010JA015880

Rodger, C. J., Kavanagh, A. J., Clilverd, M. A. and Marple, S. R., 2013. Comparison between POES energetic electron precipitation observations and riometer absorptions: Implications for determining true precipitation fluxes. *J. Geophys. Res. Space Physics*, 118(12), 7810–7821. doi:10.1002/2013JA019439

Roederer, J. G., 1970. *Dynamics of Geomagnetically Trapped Radiation*. Springer-Verlag, Berlin, Heidelberg. doi:10.1007/978-3-642-49300-3

Roederer, J. G. and Lejosne, S., 2018. Coordinates for representing radiation belt particle flux. *J. Geophys. Res. Space Physics*, 123(2), 1381–1387. doi:10.1002/2017JA025053

Schiller, Q., Li, X., Blum, L., Tu, W., Turner, D. L. and Blake, J. B., 2014. A nonstorm time enhancement of relativistic electrons in the outer radiation belt. *Geophys. Res. Lett.*, 41(1), 7–12. doi:10.1002/2013GL058485

Selesnick, R. S. and Albert, J. M., 2019. Variability of the proton radiation belt. *J. Geophys. Res. Space Physics*, 124(7), 5516–5527. doi:10.1029/2019JA026754

Shen, X.-C., Hudson, M. K., Jaynes, A. N., Shi, Q., Tian, A., Claudepierre, S. G., Qin, M.-R., Zong, Q.-G. and Sun, W.-J., 2017. Statistical study of the storm time radiation belt evolution during Van Allen Probes era: CME- versus CIR-driven storms. *J. Geophys. Res. Space Physics*, 122(8), 8327–8339. doi:10.1002/2017JA024100

Shprits, Y. Y., Horne, R. B., Kellerman, A. C. and Drozdov, A. Y., 2018. The dynamics of Van Allen belts revisited. *Nat. Phys.*, 14(2), 102–103. doi:10.1038/nphys4350

Shprits, Y. Y., Kellerman, A., Aseev, N., Drozdov, A. Y. and Michaelis, I., 2017. Multi-MeV electron loss in the heart of the radiation belts. *Geophys. Res. Lett.*, 44(3), 1204–1209. doi:10.1002/2016GL072258

Shue, J. H., Song, P., Russell, C. T., Steinberg, J. T., Chao, J. K., Zastenker, G., Vaisberg, O. L., Kokubun, S., Singer, H. J. and Detman, T. R., 1998. Magnetopause location under extreme solar wind conditions. *J. Geophys. Res.*, 103(A8), 17691–17700. doi:10.1029/98JA01103

Simms, L. E., Engebretson, M. J., Rodger, C. J., Dimitrakoudis, S., Mann, I. R. and Chi, P. J., 2021. The combined influence of lower band chorus and ULF waves on radiation belt electron fluxes at individual L shells. *J. Geophys. Res. Space Physics*, 126(5), e28755. doi:10.1029/2020JA028755

Singer, H., Matheson, L., Grubb, R., Newman, A. and Bouwer, D., 1996. Monitoring space weather with the GOES magnetometers. In Washwell, E. R., editor, *GOES-8 and Beyond*, volume 2812 of *Society of Photo-Optical Instrumentation Engineers (SPIE) Conference Series*, pages 299–308. doi:10.1117/12.254077

Siscoe, G. and Odstrcil, D., 2008. Ways in which ICME sheaths differ from magnetosheaths. *J. Geophys. Res. Space Physics*, 113(A9), A00B07. doi:10.1029/2008JA013142

Smirnov, A. G., Berrendorf, M., Shprits, Y. Y., Kronberg, E. A., Allison, H. J., Aseev, N. A., Zhelavskaya, I. S., Morley, S. K., Reeves, G. D., Carver, M. R. and Effenberger, F., 2020. Medium Energy Electron Flux in Earth's Outer Radiation Belt (MERLIN): A machine learning model. *Space Weather*, 18(11), e02532. doi: 10.1029/2020SW002532

Sorathia, K. A., Ukhorskiy, A. Y., Merkin, V. G., Fennell, J. F. and Claudepierre, S. G., 2018. Modeling the depletion and recovery of the outer radiation belt during a geomagnetic storm: combined MHD and test particle simulations. *J. Geophys. Res. Space Physics*, 123(7), 5590–5609. doi:10.1029/2018JA025506

Spence, H. E., Reeves, G. D., Baker, D. N., Blake, J. B., Bolton, M., Bourdarie, S., Chan, A. A., Claudepierre, S. G., Clemmons, J. H., Cravens, J. P., Elkington, S. R., Fennell, J. F., Friedel, R. H. W., Funsten, H. O., Goldstein, J., Green, J. C., Guthrie, A., Henderson, M. G., Horne, R. B., Hudson, M. K., Jahn, J.-M., Jordanova, V. K., Kanekal, S. G., Klatt, B. W., Larsen, B. A., Li, X., MacDonald, E. A., Mann, I. R., Niehof, J., O'Brien, T. P., Onsager, T. G., Salvaggio, D., Skoug, R. M., Smith, S. S., Suther, L. L., Thomsen, M. F. and Thorne, R. M., 2013. Science goals and overview of the Radiation Belt Storm Probes (RBSP) Energetic Particle, Composition, and Thermal Plasma (ECT) suite on NASA's Van Allen Probes mission. *Space Sci. Rev.*, 179, 311–336. doi:10.1007/s11214-013-0007-5

Su, Z., Zhu, H., Xiao, F., Zong, Q. G., Zhou, X. Z., Zheng, H., Wang, Y., Wang, S., Hao, Y. X., Gao, Z., He, Z., Baker, D. N., Spence, H. E., Reeves, G. D., Blake, J. B. and Wygant, J. R., 2015. Ultra-low-frequency wave-driven diffusion of radiation belt relativistic electrons. *Nat. Commun.*, 6, 10096. doi:10.1038/ncomms10096

Thorne, R. M., 2010. Radiation belt dynamics: The importance of wave-particle interactions. *Geophys. Res. Lett.*, 37(22), L22107. doi:10.1029/2010GL044990

Thorne, R. M., Li, W., Ni, B., Ma, Q., Bortnik, J., Chen, L., Baker, D. N., Spence, H. E., Reeves, G. D., Henderson, M. G., Kletzing, C. A., Kurth, W. S., Hospodarsky, G. B., Blake, J. B., Fennell, J. F., Claudepierre, S. G. and Kanekal, S. G., 2013. Rapid local acceleration of relativistic radiation-belt electrons by magnetospheric chorus. *Nature*, 504(7480), 411–414. doi:10.1038/nature12889

Torrence, C. and Compo, G. P., 1998. A practical guide to wavelet analysis. *Bulletin of the American Meteorological Society*, 79(1), 61–78. doi:10.1175/1520-0477(1998)079<0061:APGTWA>2.0.CO;2

Tsurutani, B. T., Gonzalez, W. D., Tang, F., Akasofu, S. I. and Smith, E. J., 1988. Origin of interplanetary southward magnetic fields responsible for major magnetic storms near solar maximum (1978-1979). *J. Geophys. Res.*, 93(A8), 8519–8531. doi:10.1029/JA093iA08p08519

Tsurutani, B. T. and Smith, E. J., 1974. Postmidnight chorus: A substorm phenomenon. *J. Geophys. Res.*, 79(1), 118–127. doi:10.1029/JA079i001p00118

Tsyganenko, N. A. and Sitnov, M. I., 2005. Modeling the dynamics of the inner magnetosphere during strong geomagnetic storms. *J. Geophys. Res. Space Physics*, 110(A3), A03208. doi:10.1029/2004JA010798

Turner, D. L., Angelopoulos, V., Li, W., Bortnik, J., Ni, B., Ma, Q., Thorne, R. M., Morley, S. K., Henderson, M. G., Reeves, G. D., Usanova, M., Mann, I. R., Claudepierre, S. G., Blake, J. B., Baker, D. N., Huang, C. L., Spence, H., Kurth, W., Kletzing, C. and Rodriguez, J. V., 2014a. Competing source and loss mechanisms due to wave-particle interactions in Earth's outer radiation belt during the 30 September to 3 October 2012 geomagnetic storm. *J. Geophys. Res. Space Physics*, 119(3), 1960–1979. doi:10.1002/2014JA019770

Turner, D. L., Angelopoulos, V., Li, W., Hartinger, M. D., Usanova, M., Mann, I. R., Bortnik, J. and Shprits, Y., 2013. On the storm-time evolution of relativistic electron phase space density in Earth's outer radiation belt. *J. Geophys. Res. Space Physics*, 118(5), 2196–2212. doi:10.1002/jgra.50151

Turner, D. L., Angelopoulos, V., Morley, S. K., Henderson, M. G., Reeves, G. D., Li, W., Baker, D. N., Huang, C. L., Boyd, A., Spence, H. E., Claudepierre, S. G., Blake, J. B. and Rodriguez, J. V., 2014b. On the cause and extent of outer radiation belt losses during the 30 September 2012 dropout event. *J. Geophys. Res. Space Physics*, 119(3), 1530–1540. doi:10.1002/2013JA019446

Turner, D. L., Cohen, I. J., Michael, A., Sorathia, K., Merkin, S., Mauk, B. H., Ukhorskiy, S., Murphy, K. R., Gabrielse, C., Boyd, A. J., Fennell, J. F., Blake, J. B., Claudepierre, S. G., Drozdov, A. Y., Jaynes, A. N., Ripoll, J.-F. and Reeves, G. D., 2021. Can Earth's magnetotail plasma sheet produce a source of relativistic electrons for the radiation belts? *Geophys. Res. Lett.*, 48(21), e95495. doi:10.1029/2021GL095495

Turner, D. L., Kilpua, E. K. J., Hietala, H., Claudepierre, S. G., O'Brien, T. P., Fennell, J. F., Blake, J. B., Jaynes, A. N., Kanekal, S., Baker, D. N., Spence,

H. E., Ripoll, J.-F. and Reeves, G. D., 2019. The response of Earth's electron radiation belts to geomagnetic storms: Statistics from the Van Allen Probes era including effects from different storm drivers. *J. Geophys. Res. Space Physics*, 124, 1013–1034. doi:10.1029/2018JA026066

Turner, D. L., O'Brien, T. P., Fennell, J. F., Claudepierre, S. G., Blake, J. B., Kilpua, E. K. J. and Hietala, H., 2015. The effects of geomagnetic storms on electrons in Earth's radiation belts. *Geophys. Res. Lett.*, 42, 9176–9184. doi: 10.1002/2015GL064747

Turner, D. L., Shprits, Y., Hartinger, M. and Angelopoulos, V., 2012. Explaining sudden losses of outer radiation belt electrons during geomagnetic storms. *Nat. Phys.*, 8(3), 208–212. doi:10.1038/nphys2185

Turner, D. L. and Ukhorskiy, A. Y., 2020. Outer radiation belt losses by magnetopause incursions and outward radial transport: new insight and outstanding questions from the Van Allen Probes era. In Jaynes, A. N. and Usanova, M. E., editors, *The Dynamic Loss of Earth's Radiation Belts*, pages 1–28. Elsevier. doi: 10.1016/B978-0-12-813371-2.00001-9

Tuszewski, M., Cayton, T. E., Ingraham, J. C. and Kippen, R. M., 2004. Bremsstrahlung effects in energetic particle detectors. *Space Weather*, 2(10), S10S01. doi:10.1029/2003SW000057

Ukhorskiy, A. Y., Sitnov, M. I., Mitchell, D. G., Takahashi, K., Lanzerotti, L. J. and Mauk, B. H., 2014. Rotationally driven 'zebra stripes' in Earth's inner radiation belt. *Nature*, 507(7492), 338–340. doi:10.1038/nature13046

Usanova, M. E., Drozdov, A., Orlova, K., Mann, I. R., Shprits, Y., Robertson, M. T., Turner, D. L., Milling, D. K., Kale, A. and Baker, D. N., 2014. Effect of EMIC waves on relativistic and ultrarelativistic electron populations: Ground-based and Van Allen Probes observations. *Geophys. Res. Lett.*, 41(5), 1375–1381. doi:10.1002/2013GL059024

Van Allen, J. A., 1959. The geomagnetically trapped corpuscular radiation. *J. Geophys. Res.*, 64(11), 1683–1689. doi:10.1029/JZ064i011p01683

Van Allen, J. A., Ludwig, G. H., Ray, E. C. and McIlwain, C. E., 1958. Observation of high intensity radiation by satellites 1958 Alpha and Gamma. *J. Jet Propuls.*, 28(9), 588–592. doi:10.2514/8.7396

Wang, C.-P., Thorne, R., Liu, T. Z., Hartinger, M. D., Nagai, T., Angelopoulos, V., Wygant, J. R., Breneman, A., Kletzing, C., Reeves, G. D., Claudepierre, S. G. and Spence, H. E., 2017. A multispacecraft event study of Pc5 ultralow-frequency waves in the magnetosphere and their external drivers. *J. Geophys. Res. Space Physics*, 122(5), 5132–5147. doi:10.1002/2016JA023610

Wing, S., Johnson, J. R., Turner, D. L., Ukhorskiy, A. Y. and Boyd, A. J., 2022. Untangling the solar wind and magnetospheric drivers of the radiation belt electrons. *J. Geophys. Res. Space Physics*, 127(4), e30246. doi:10.1029/2021JA030246

Wygant, J. R., Bonnell, J. W., Goetz, K., Ergun, R. E., Mozer, F. S., Bale, S. D., Ludlam, M., Turin, P., Harvey, P. R., Hochmann, R., Harps, K., Dalton, G., McCauley, J., Rachelson, W., Gordon, D., Donakowski, B., Shultz, C., Smith, C., Diaz-Aguado, M., Fischer, J., Heavner, S., Berg, P., Malsapina, D. M., Bolton, M. K., Hudson, M., Strangeway, R. J., Baker, D. N., Li, X., Albert, J., Foster, J. C., Chaston, C. C., Mann, I., Donovan, E., Cully, C. M., Cattell, C. A., Krasnoselskikh, V., Kersten, K., Brenneman, A. and Tao, J. B., 2013. The Electric Field and Waves instruments on the Radiation Belt Storm Probes mission. *Space Sci. Rev.*, 179(1-4), 183–220. doi:10.1007/s11214-013-0013-7

Zhang, X. J., Mourenas, D., Artemyev, A. V., Angelopoulos, V. and Sauvaud, J. A., 2019. Precipitation of MeV and sub-MeV electrons due to combined effects of EMIC and ULF waves. *J. Geophys. Res. Space Physics*, 124(10), 7923–7935. doi:10.1029/2019JA026566

Zhao, H., Baker, D. N., Li, X., Malaspina, D. M., Jaynes, A. N. and Kanekal, S. G., 2019a. On the acceleration mechanism of ultrarelativistic electrons in the center of the outer radiation belt: a statistical study. *J. Geophys. Res. Space Physics*, 124(11), 8590–8599. doi:10.1029/2019JA027111

Zhao, H., Ni, B., Li, X., Baker, D. N., Johnston, W. R., Zhang, W., Xiang, Z., Gu, X., Jaynes, A. N., Kanekal, S. G., Blake, J. B., Claudepierre, S. G., Temerin, M. A., Funsten, H. O., Reeves, G. D. and Boyd, A. J., 2019b. Plasmaspheric hiss waves generate a reversed energy spectrum of radiation belt electrons. *Nat. Phys.*, 15(4), 367–372. doi:10.1038/s41567-018-0391-6

Zhou, Q., Xiao, F., Yang, C., Liu, S., He, Y., Wygant, J. R., Baker, D. N., Spence, H. E., Reeves, G. D. and Funsten, H. O., 2016. Evolution of chorus emissions into plasmaspheric hiss observed by Van Allen Probes. *J. Geophys. Res. Space Physics*, 121(5), 4518–4529. doi:10.1002/2016JA022366